POLITECNICO DI MILANO

Facoltà di Ingegneria Industriale

Corso di Laurea Magistrale in
Ingegneria Aeronautica

EXPERIMENTAL AND NUMERICAL STUDY OF BEARING DAMAGE AND FAILURE OF TAILORED FIBRE PLACEMENT REINFORCED JOINING SYSTEMS IN FLAT PANELS

Relatore: Prof. Luca Angelo DI LANDRO (Politecnico di Milano)

Co-relatori: Dr. Anthony PICKETT (Universität Stuttgart)

Ing. Claudio MACCHIONE (Universität Stuttgart)

Tesi di Laurea di:

Daniel LONGHI Matr. 770901

Anno Accademico 2011-2012

Contents

List of Figures

List of Tables

Abstract

The aim of this work is an experimental and numerical investigation of the potential benefits of Tailored Fiber Placement (TFP) Patch reinforcements, with a focus on the influence of the design parameters on bearing behavior. TFP Patches can be employed as reinforcing elements for jointed systems: the fibers are placed along stress paths in order to minimize mass and maximize load carrying capacity. The remarkably customizable orientation of the fibers in a TFP Patch enables the optimization of fibre placement around the connecting holes. The work focuses on improving the predictive failure and optimization techniques. Experimental tests carried out on both unreinforced and reinforced quasi-isotropic carbon/epoxy coupons, manufactured with the Vacuum Assisted Resin Infusion (VARI) technique, showed a significant increase of the loading capacity of the laminates, due to the application of the patches. The high local thickness at the hole cross section, an effect of the infusion technique adopted, has however led to a lower bearing stress than in the unreinforced configuration. A numerical model was built and compared to the experimental data in order to represent numerically the bearing damage and failure behavior of the joints. The numerical model was developed from a new research code provided by ESI-Group for the software PAM-CRASH, originally designed for crushing phenomena such as cylinder impact. The model provides encouraging results which allow it to be included in the investigation of more complex components, such as typical aeronautical panels.

Keywords: Bearing, joining systems, composite materials, tailored fibre placement, patch reinforcements, vacuum assisted resin infusion, finite elements method.

Sommario

L'obiettivo di questo lavoro di tesi consiste nello studio sperimentale e numerico delle potenzialità rappresentate da elementi di rinforzo applicati a giunzioni in materiale composito, concentrando l'attenzione all'influenza di tali elementi su meccanismi di cedimento e danneggiamento per bearing dei fori. Patches realizzate con la tecnica Tailored Fiber Placement (TFP) possono essere impiegate come rinforzi in elementi di giunzione: le fibre sono disposte lungo i percorsi di carico per ridurre il peso del componente e incrementare la quantità di carico che può essere sopportata. La possibilità di scegliere una qualsiasi orientazione delle fibre all'interno delle patches permette, una volta compresi i fenomeni e i modi di danneggiamento, di ottimizzarne la disposizione attorno ai fori degli elementi di giunzione. Prove sperimentali su provini quasi isotropi in materiale composito (fibre di carbonio e resina epossidica), rinforzati e non, realizzati attraverso la tecnica Vacuum Assisted Resin Infusion (VARI), hanno mostrato un significativo aumento della capacità di carico dovuta all'applicazione delle patches. Lo sforzo di bearing è rimasto tuttavia inferiore a quello dei laminati non rinforzati a causa del notevole aumento locale di spessore dovuto ai rinforzi, limite evidente della tecnica di infusione adottata. Un modello numerico è stato realizzato per correlare i risultati sperimentali, con lo scopo di proporre una corretta rappresentazione dei fenomeni di danneggiamento indotti da bearing, attraverso lo sviluppo di un codice sperimentale fornito da ESI-Group per il software PAM-CRASH, ideato per fenomeni di crush assiale quale l'impatto di cilindri. Il modello ha prodotto risultati incoraggianti che suggeriscono la possibilità di una sua implementazione nella rappresentazione di un componente più complesso quale un tipico pannello aeronautico, anche con l'applicazione di patches.

Parole chiave: Bearing, giunzioni, materiali compositi, tailored fibre placement, patch di rinforzo, vacuum assisted resin infusion, elementi finiti.

Chapter 1

Introduction

1.1 General overview

The present investigation has been carried out in the frame of the European project CERFAC 'Cost Effective Reinforcements of Fasteners Area in Composites', in collaboration with several European companies and research institutes.
In the last years the aeronautical industry has been working on lighter, cost-effective and energy-efficient composite materials to improve the performances of new generation airplanes. One of the challenges of working with such advanced materials is the design of efficient joining systems for high performance structures. Since a large number of such interfaces is used in aircrafts, even little improvements in this field are highly promising in terms of weight and cost reductions. In this project, the transfer of loads between composite parts through innovative designs for joining and assembly is investigated.
The demands of structural efficiency has always been one of the main issues in the aeronautical industry, as well as in the advanced automotive sector, where the cost-to-weight ratio has always been considered a leading factor. This has allowed the usage of composites materials, like carbon fiber reinforced plastic, to become more and more important, because of their interesting specific mechanical properties.
Moreover, the reliability of numerical tools that can predict damage onset and propagation in composite materials has become more and more focal. Once numerical models are validated against experimental data, in fact, they can be used to simulate the structural response, saving time, money and material. As the effect of damage upon mechanical properties of composite laminates is still not completely clear, a composite structural design tends currently to

be conservative. Therefore their potential is still far from being completely developed, so new techniques and improvement possibilities are still to be investigated.

1.2 Motivations

This work was carried out at the Institut für Flugzeugbau (*Institute of Aircraft Design*) of the University of Stuttgart, thanks to a six months Erasmus program offered by Politecnico di Milano.
Due to the high level of specialization reached by the modern industry, it becomes increasingly more important sharing knowledge, interests, and competences. Best solutions are always found combining different abilities and comparing different points of view.
According to this perspective, nowadays, the most complete, efficient, and cost-affordable way to face an engineering problem is combining a theoretical, an experimental and a numerical approach. Comparing these strategies allows to overcome their respective limits, and to obtain results that otherwise could never be achieved.

1.3 Targets of this research project

The initial purpose of this research project has been the continuation and extension of previous studies conducted by Y. Urbanek at the University of Stuttgart on the possible employment of tailored fibre placement (TFP) patches reinforcing joining system in flat panels. Urbanek experimentally investigated different configurations of spiral reinforcements trying to improve the bearing behavior in zones of stress concentrations, in particular holed flat surfaces of carbon/epoxy composite laminates.
The first aim of this project is to determine experimentally the bearing improvement obtained by a different configuration of these patches, namely star shapes made by different numbers of rovings per arm. This achievement was accomplished in terms of total force, but not in terms of bearing stress, due to the particular manufacturing process employed in this work, the Vacuum Assisted Resin Infusion, whose greater limit, a limited control on the laminate thickness, is here highlighted.
The second target of this work focuses on the implementation of a numerical model capable of correlating the experimental data with the numerical results and representing the bearing damaging behavior. The numerical study applied a research version of a crush code, developed for the study of impact

problems. The numerical model was implemented according to the nature of the entire project, i.e, the pursuit of efficiency and the prospective of an optimization process. The correlation between the numerical model and the experimental data collected from the tests shows good results up to bearing failure. Even considering the simplicity of the model, it is believed that it would be reliable for some improvements regarding the post-failure behavior, which should be further investigated, for example in a damage-tolerance approach.

1.4 Main issues

The next Chapter presents a general overview of the state of the art of composite materials, the TFP technique, and the Vacuum Assisted Resin Infusion process. It also includes the main features of bearing phenomena, damage and failure.
Chapter 3 contains information about the investigated materials, and how the experimental tests were carried out starting with the presentation of the infusion process.
In Chapter 4 it is developed the theoretical model on which the numerical explicit analysis is based, and the calibration of the mechanical properties of the investigated material, requested from the numerical model.
Some preliminary tests were carried out on holed coupons to investigate the effect of stress concentration in simple flat laminates under tensile loading. This is shown in Chapter 5 together with a further development of the average stress criterion initially proposed by Whitney and Nuismer and applied for numerical failure prediction in holed flat plates by Greve.
In Chapter 6 the bearing tests of two different configurations of TFP reinforced coupons are presented, and compared with an unreinforced one. Starting from the test data collected, advantages and limits of this technique are here discussed.
Chapter 7 presents the finite element model developed to represent bearing damage and failure, with a new crush code available in a research version of PAM-CRASH software.
In the end, in Chapter 8, aims, results obtained and future developments will be summarized.
Finally in appendix A a rough optimization carried out to make a preliminary investigation of the patches is presented, and in appendix B results coming from the experimental tests are collected.

Chapter 2

Literature review

2.1 CERFAC project

CERFAC is an EU-funded project whose major challenge is the design and manufacturing of strong and cost-efficient joints for high performance carbon fiber reinforced plastic (CFRP) structures. Due to the large number of such interfaces in aircrafts, a solution to these problems is highly promising in terms of weight and cost reductions. It can be stated that current design practices give non-optimal joining systems, that are poor in terms of weight and cost efficiency. Consequently, composite designs are often rejected in favour of traditional metal alloys.
Special and frequent problems in fastener areas are the transfer of the load along rivets lines, the assembly of flat or curved thin-walled panels, and the introduction of concentrated loads for connecting lugs with thicker laminates. Therefore, the project focuses on applications with significant volume and occurrence, such as butt straps & splices, orbital and longitudinal multi-functional joints, single and multiple bolts attachments.
The first aim planned for the project is to gather a catalogue of reinforcement solutions in the region of fastener holes (rivet holes, bolt holes) or edges, leading to lighter, stronger and more damage tolerant designs. Predictive analysis methods and optimization techniques supported by extensive testing will enable cost and weight efficient solutions. Secondly, the project focuses on several specific reinforcements and these will be developed throughout the project in order to achieve a higher level of maturity and hopefully to allow their use in an industrial environment.

2.2 Composite materials in joining systems

Composite materials have become more extensively used in every project that requires high structural performance and light weight at the same time. Their extremely advantageous mechanical characteristics have led to an extensive use in both primary and secondary structures of next-generation mega-carrier aircraft or supersonic transport aircraft, as well as in automotive or naval industries.

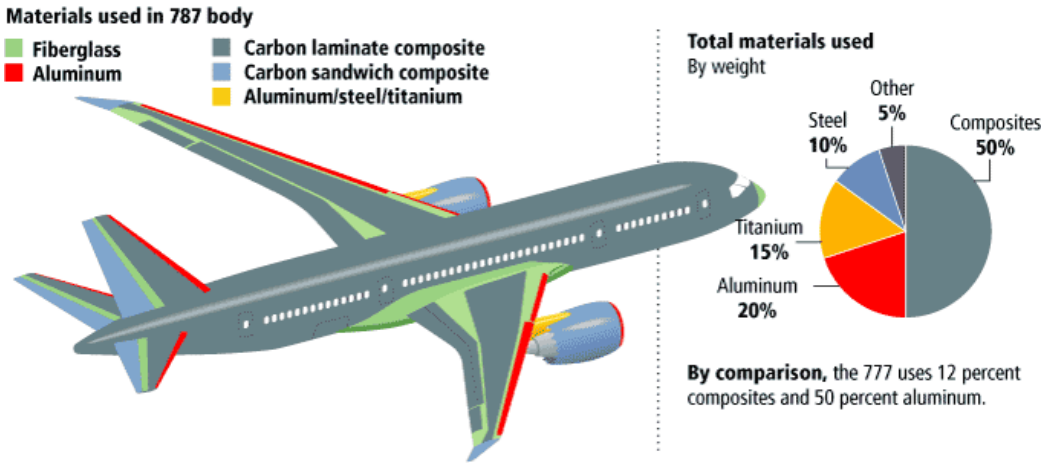

Figure 2.1: Boeing 787 Dreamliner [1]

The aircraft of Fig. 2.1, was built with up to 50% of composite materials, and it was the first major airliner to use composite materials as primary material in the construction of its airframe. One of the most versatile aspects is the possibility to design the orientation of the reinforcements according to the predicted load path. Moreover, with the recent manufacturing techniques, it is possible to produce near net-shape components, with remarkable saving in time, money and materials. Compression moulding, vacuum moulding, pultruding, filament winding, and resin transfer moulding [2] are just a few of the current options. For example this is the case of Boeing 787 Dreamliner fuselage, constructed using single piece barrels joined end to end instead of classical multiple panels.
Every structure usually needs joining systems. For example, according to the Boeing Company, the Boeing 747 includes six million parts, half of which are fasteners. They play a critical role in defining the longevity, the structural integrity, and the design philosophy of most of the aircraft structures.
Bolted connections are commonly preferred to other joining techniques as they allow greater freedom in assembly and repair. A mechanically fastened joint in CFRP laminates is necessary because of its advantages in inspection,

replacement and reliability, even though it has limits due to stress concentrations. In fact, a bolted joint introduces an additional compression load on the laminate and so a new potential failure mode, against which the laminate is relatively weak.
The structural failure of joining system components usually begins at the fastener sites, since high stress concentrations make the hole region more vulnerable to crack initiation. To utilize the full potential of laminated composite materials as structural elements, therefore, the damage and failure behavior of mechanically fastened joint must be understood.
A mechanical joint transfers load by shear forces in the bolt and frictional forces developed at the interface between the joined plates. The magnitude of the load transferred by frictional forces depends on both the interface condition and the clamping force. During the loading phase, a contact stress is generated between the bolt and the laminate. These stresses may vary with the circumferential position, with the geometry of the joint, and also through the thickness of the laminate. Depending on the specimen geometry and in general on the stacking orientation, the joint would eventually fail in 3 basic modes, namely net tension, shear out, bearing, or a mixtures of these modes. Usually, net tension and shear out failures are associated with stress concentration due to the presence of the hole and are usually catastrophic.
Bearing failure, on the other hand, is the ideal failure mode for bolted joints because it allows a compression damage accumulation that is function of applied load.

2.3 Bearing strength and failure behavior of bolted composite joints

The efficiency J of a single row fastened joint in a panel is defined as the ratio of the maximum bearing load, P_B, that can be transferred by the bolt to the laminate and the ultimate tensile load, P_{TU}, for a laminate section far from the hole. It results in a function of the tensile strength F_{TU} and the bearing strength, F_B, of the laminate, the width, w, and thickness, t, of the specimen, and the diameter, d, and local thickness and width, t_B and w_B, of the hole, as shown in Fig. 2.2 left. The joint efficiency J is given by

$$J = \frac{P_B}{P_{tu}} = \frac{F_B * w_B * t_B}{F_{tu} * w * t} \tag{2.1}$$

Even if usually some composite materials, like Carbon Fiber Reinforced Plastics (CFRP), overcome metal alloys in specific properties and in general

in efficiency, that is not the case of bearing failure. For composite laminates, the joint efficiency is significantly lower than for structural metals [3], as shown in fig. 2.2 right. This problem has been well known since their first structural applications.

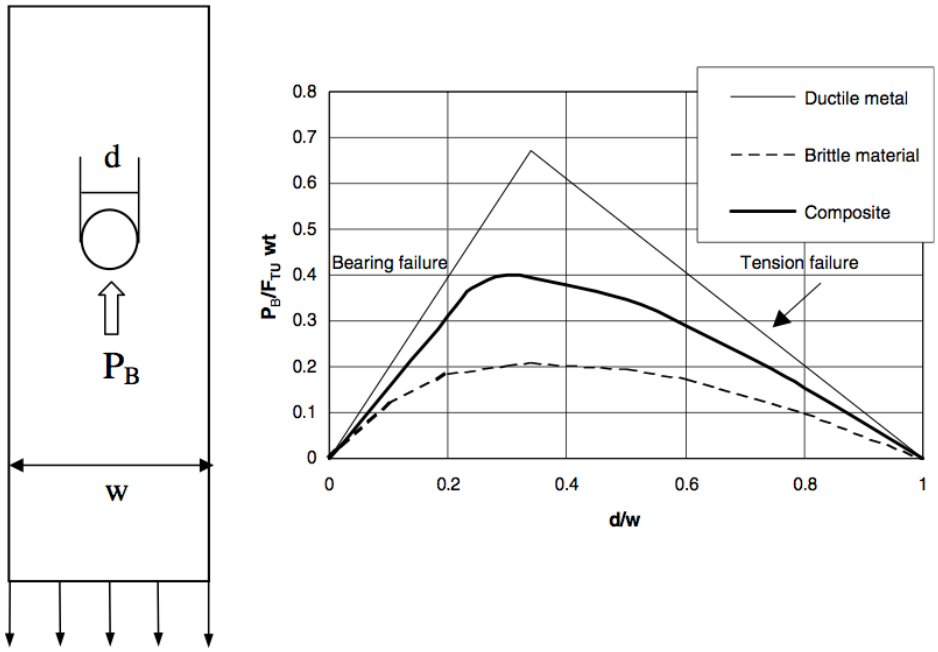

Figure 2.2: Joint efficiency of different materials [3]

Xiao and Ishikawa [4] identified different steps in the evolution of a bearing phenomenon, as shown in Fig. 2.3. They stated that bearing failure is caused by a compressive damage accumulation process that can be classified into four stages: damage onset, damage growth, local fracture and structural fracture. The dominant modes for the onset of damage appear to be fiber micro-buckling and matrix cracking, while the final failure stage is dominated by out-of-plane shear cracks and delamination. Several other parameters, such as the loading constraints or the stacking of the laminate, influence failure modes and damage mechanisms.
Every layer individually contributes to the accumulation of damage in terms of fiber micro-buckling, fiber-matrix shearing and matrix compression. However, bearing first failures in composite laminates can be grouped into two basic in-plane failure modes: matrix compression and fiber compression-shear failure. The final failure stage is dominated by more complex out-of-plane failure modes, such as through-thickness shear cracks and delaminations.

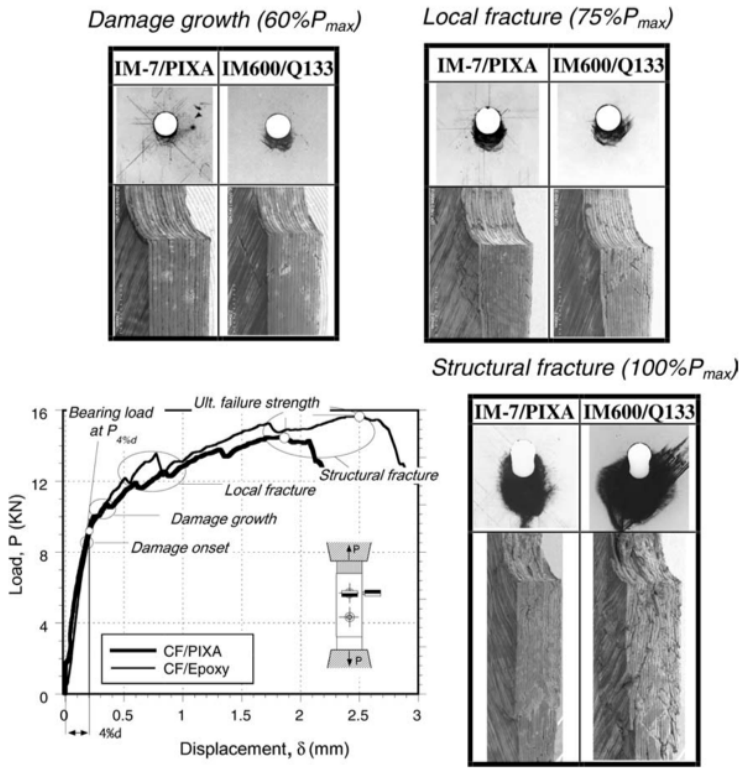

Figure 2.3: Typical evolution of a bearing failure, resulting from test on different laminates. [4]

2.4 Tailored Fibre Placement

The Tailored Fibre Placement technology, which has been developed at the Leibniz Institute of Polymer Research Dresden, allows to take fully advantage of the potential of composite materials. It is rapidly gaining ground as it is capable of manufacturing of textile preforms for composite parts with fibre layouts of arbitrary directions, using standard embroidery technology.

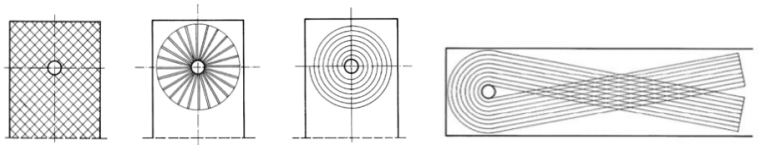

Figure 2.4: Example of the path followed by rovings to in TFP patches reinforcements. [5]

This technique is based on the principle of sewing for a continuous placement of fibrous material.

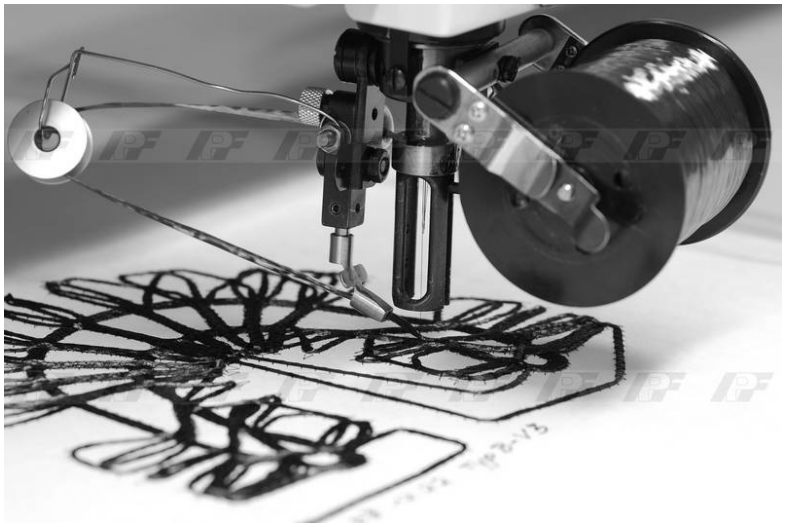

Figure 2.5: Stitching machine applying roving reinforcements according to a predetermined path. [6]

Among the many advantages of the TFP technology, the automatic disposition ensures high accuracy and repeatablity of the process. TFP machines with multiple heads allow to achieve significant productivity ratio, while the production of net-shape components reduces costs and avoid the waste of valuable reinforcement fibers. Moreover, the TFP technique allows the fabrication of tailored preform for a specific reinforcing area. All these aspects make its application every day more extensive in lightweight aircraft parts as well as in automotive components. Nowadays, the Tailored Fiber Placement is already in a few companies a well-established textile technology for the manufacture of dry preforms.

2.5 Resin Infusion Techniques

Liquid Composite Moulding (LCM) is a family of processes used to manufacture large composite parts, which, initially, were employed on reinforced components for automotive, civil and naval applications, and have recently acquired more importance in aeronautical industries too. Strong characteristic of these parts is the possibility of obtaining products with complex shapes, high thickness, and low tolerance. Moreover, it is possible to produce directly components that could be obtained only assembling several different single

parts. Vacuum Infusion is a particular application of this family of moulding processes where a reinforcing preform, typically made of continuous glass or carbon fibers, is draped on a one-sided mould surface. Vacuum is drown to the preform by means of a sealed bag, driving thermoset resin from a reservoir to the mould cavity, to fill the empty spaces between the fibers. The resin system is usually designed so that the pot life is slightly longer than the preform filling time in order to ensure a complete infusion. Then, the part is demoulded and acquire rigidity during the post cure process. A correct mould design, which means, definition of dimensions and locations of the distribution medium, resin inlets and outlets and the type of resin, is crucial in order to achieve a good infiltration and final good results. It is also important to obtain a complete mould filling and the elimination of micro-level and macro-level voids in the part, which are one of the causes of possible weak areas in final product. A valid example could be the new wing spar with a sinewave-shaped web from carbon fiber composites developed and manufactured with VARI by Premium AEROTEC [7], to demonstrate the potential of the use of carbon fiber in aircraft wing construction. The component was the result of a two-year technology project in collaboration with Boeing.

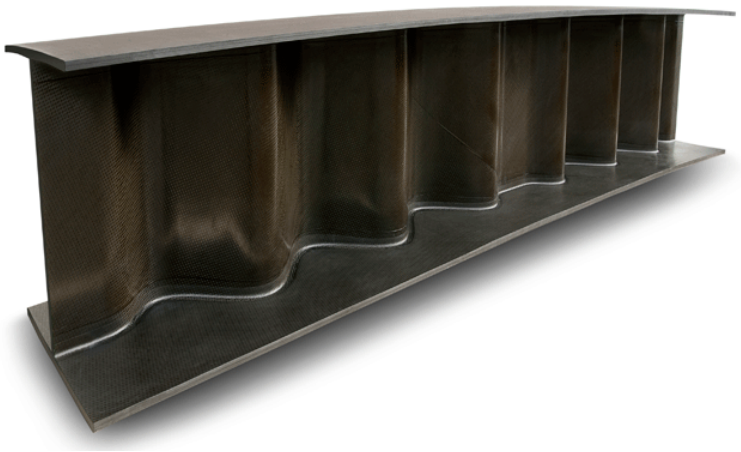

Figure 2.6: New wing spar with a sinewave-shaped developed and manufactured by Premium AEROTEC [7]

However, VARI is a labor-intensive process, which requires expert operators to perform a satisfactory infusion. It leads to a low rate production, that even in aeronautical industries, limits the process efficiency. As the autoclave is not requested, the part to be infiltrated can have very huge dimensions, such as windmill blades, ship decks and hulls, as the one in Fig. 2.7.

Figure 2.7: Vacuum Infusion Technology: Hull, *Southport boat* [8]

One of the major issues in the generic VARI process is the low fiber content due to the limited compaction of the preform, since the gradient pressure cannot be higher than atmospheric pressure. Because of the architecture of the process, only low viscosity resins can be used. Another drawback is caused by the usage of the vacuum bag instead of a double-mould, whose effects were analyzed by Yenilmez et al. [9]: the high surface roughness of the part at the bag side does not allow low tolerances, and causes also variations in the component thickness. This is due to the change in the compaction pressure, as resin pressure changes during the infusion process, and to the fiber relaxation with time even at constant compaction pressure. Moreover, if the infusion has to be stopped, the possible run out of the resin in the reservoir can decrease the pressure of the resin. Nowadays several projects have reached a state-of-the-art on automated VARI systems, trying to minimize costs and reduce operator's supervision, which is currently necessary during resin injection. Bender et al. [10] investigated a flow rate control system for VARI process, which enables to regulate the evacuation of the infusion bucket and generates a computer-controlled vacuum differential between the injection and vent location. A software package, developed by ESI Group, that simulates various moulding processes, has been recently updated to simulate VARI [11]. This is designed to help with the preliminary design, to make refined calculations for process and mould optimization, and to help with final design verifications. The effects on the bearing strength of pin loaded composites manufactured with VARI was investigated by Sevkat [12].

Chapter 3

Experimental work

This work investigates the bearing damage and failure of Quasi-Isotropic (QI) carbon/epoxy laminates, made of Unidirectional (UD) layers and manufactured using the Vacuum Assisted Resin Infusion process.
A description of the investigated materials, an overview of the VARI process, of the preparation of coupons and of the ARAMIS non-contact 3D measuring system is reported in this chapter.

3.1 Investigated materials

The reinforcement consists of T700 carbon fibers with 24k-Roving [13]. As it can be seen in Fig. 3.2, to enhance the handling quality, fiber rovings are delivered by SAERTEK® company stitched together with a coarse glass fiber net, with an angle of about 60° degrees in respect to the unidirectional orientation (0°).

Figure 3.1: SAERTEX®: roll of carbon fiber UD

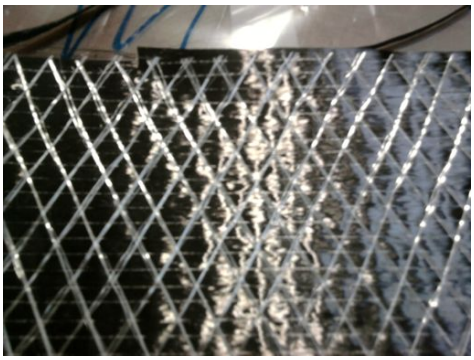

Figure 3.2: SAERTEX®: stitched layer UD

The specifications of the reinforcing material are reported in Tab. 3.1. The preform prepared for the infiltration was obtained stacking different plies of UD layers.

Table 3.1: Saertex® Fibre data, from [13]

Physical properties	**Unit**	**Carbon HT**
Density	g/cm^3	1.7
Tension	MPa	4800
E-Modul ||	GPa	235
E-Modul -	GPa	15
Breakage tension	%	1.5
Thermal expansion coefficient ||	10^{-6}/K	-0.1
Thermal expansion coefficient -	10^{-6}/K	10
Heat transferring properties	W/m*K	17
Spec. electr. properties	Ω*cm	10^{-3} - 10^{-4}
Humidity absorption -	%	0.1

The company Momentive™provides the epoxy resin used for the infusion of the preform: EPIKOTE™MGS® RIMR 235 [14]. This resin was chosen because of its low viscosity and the convenient gelation time, which allows to perform a good infusion within 90-120 minutes. The hardener, EPIKURE™Curing Agent RIM H 235, was chosen from the same company. As suggested from the supplier, a 100:34 mixing ratio was employed.
The patches are made of rovings of carbon fibre Toray T700SC-12000-50C of the company Torayca® [15]. These have a density of 1.8 g/cm^3 and a weight of 800 tex. A single roving has a width variable from 2.5 to 3 mm.

3.2 TFP reinforcements

Starting from single rovings, a TAJIMA embroidery system is able to create several configuration of TFP reinforcements, exploiting completely the potential of composite material. This project continues the work of Y. Urbanek[5], who investigated TFP patches in which the rovings were stitched according to a spiral path around the hole.

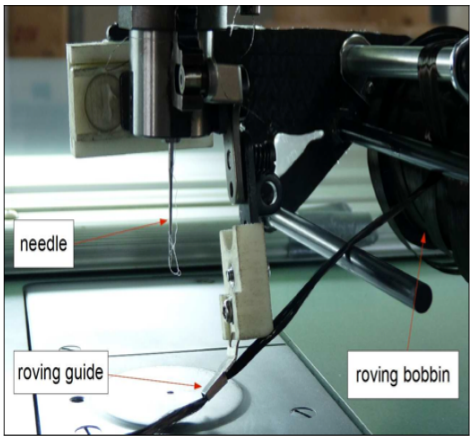

Figure 3.3: TAJIMA stitching machine, [16]

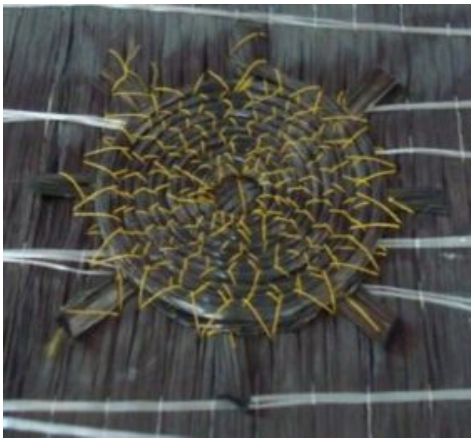

Figure 3.4: Spiral stitched patch, [5]

The TFP application stitches the patch directly on the preform, as shown in Fig. 3.4, or onto a glass fiber woven, which is disposed on, between or under the different layers of the preform before the infusion.
The former case allows to maintain a perfect orientation of the patch rovings, whose bearing error depends entirely on the precision of the stitching machine. The stitching of the patch can lead to an advantage in terms of possible delaminations between patch and preform, but also creates a sort of obstacle for the resin flow through the laminate, and tends to create resin rich zones between parallel rovings.
Instead, the latter approach was followed in this project. In this case the operator who performs the infusion has to pay attention in laying the patch onto the preform. The patch can be placed on, in the middle and under the laminate.
From previous test results, a patch stitched in the middle of the preform shows the best results, as the delamination of the patch was most of the time the cause of the first failures.

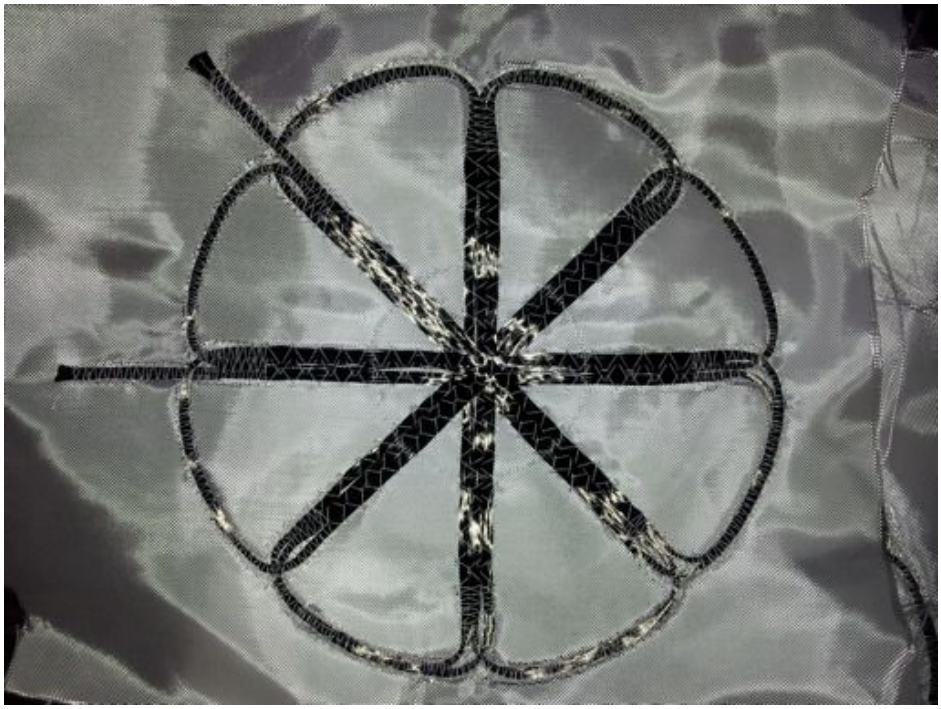

Figure 3.5: Single star patch with 3 roving not refined

In order to enhance the performances of the reinforcement, a new configuration was employed. Two series of star patches were created, one composed by 3 rovings per arm, and the other one by 5 rovings per arm.
Investigating the same shape of reinforcements but varying the number of fibers allows to perform an experimental optimization of the TFP patch reinforcement.

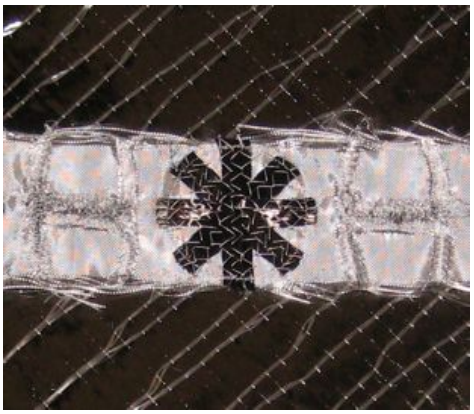

Figure 3.6: Star patches reinforcements, 3 rovings per arm

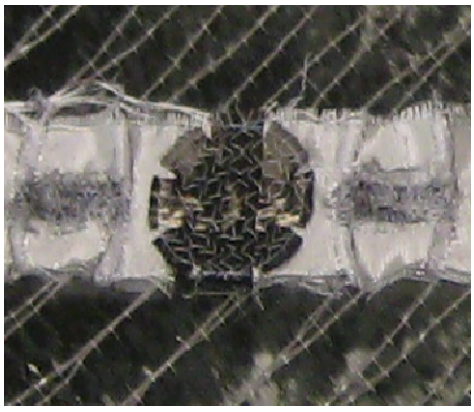

Figure 3.7: Star patches reinforcements, 5 rovings per arm

3.3 Vacuum Assisted Resin Infusion

The VARI process, used to prepare all the test coupons used in this work, is explained in this section. The manufacturing of the bearing test coupons, reinforced with 5 rovings patches, is here presented as an example. The simply architecture of VARI, shown in Fig. 3.8 is one of the characteristics that makes it more convenient in respect to autoclave and in some aspects even in respect to the classical resin transfer moulding processes.

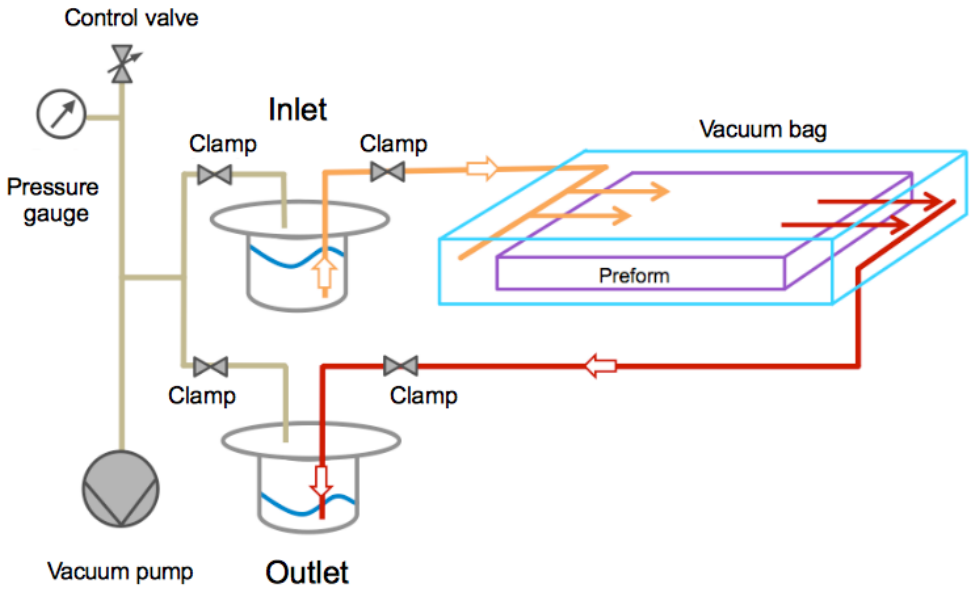

Figure 3.8: Infusion architecture, adapted from [5].

3.3.1 Preform

The number of specimens to be tested defines the dimensions of the preform, which is obtained by stacking different plies cut off the roll of reinforcement material. The cutting of the fibers is very difficult, especially in $\pm 45°$ directions. This can be done manually or, better, with an automatic cutter. In this work the roll was cut with the automatic cutter of the company Assyst Bullmer with the program CNC300 of company ProCom®, which require a CATIA [17] drawing with the dimensions of the plies, Fig 3.9.

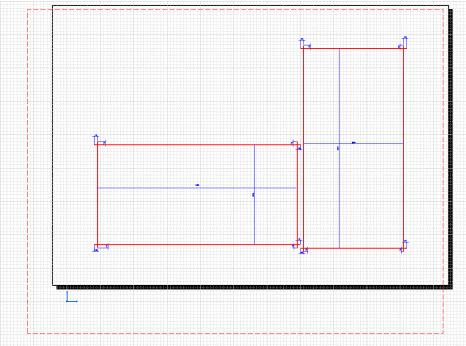

Figure 3.9: CATIA drawing for the cutting machine

Figure 3.10: Assyst Bullmer Automatic Cutter

Once the layers are obtained, these have to be weighed to be able to decide the amount of resin that will be infiltrated. For the particular architecture of the process a quantity resin higher than the 50% of the weight of the preform is suggested, in order to compensate the amount of resin that could remain in the pipes at the end of the infusion.

3.3.2 Additional layers

As with many things in the infusion process, it is absolutely essential to select the right product for the right purpose. Apart from the preform, other layers have to be prepared, each one having an important role in the process:

- *Vacuum bag (Vacuum Folie)*: A nylon bagging film is sealed to the edge of the mould with gum-like tacky tape to create a closed system. It must have bigger dimensions than the mould, in order to avoid folds and wrinkles, that both represent preferential undesiderable ways of flowing for the resin.

- *Distribution medium (Fließhilfe)*: it is a highly permeable extruded medium placed above and below the preform, which assists the resin flow throughout the preform during the infusion.

- *Peel-ply (Abreißgewebe)*: This polyester fabric has to be always placed between the preform surfaces and the others materials. It is a strong woven product with a good heat resistance. Peel plies provide a clean, uncontaminated surface for subsequent bonding or painting.

- *Breather (Lochfolie)*: a polyester non-woven fabrics that allows air and volatiles to be removed from within the vacuum bag throughout the

cure cycle. They also absorb excess resin present in some composite stacking.

- *Tacky Tape (Sealant)*: a gum-like sealant tape displaced all along the border of the mould, that seals the vacuum bag.

VARI process allows to infuse several different shapes, but for the purpose of this project, coupons were obtained from a simple flat surface. Hence, a metal flat plate is taken as a mould. This was cleaned with Aceton several times, in order to remove possible impurity caused by previous works, which would surely affect the quality of coupons. As already said, products made with VARI process have sides of different surface quality.
A chemical releasing agent, 770-NC Frekote[18], is applied all over the surface of the mould, which will let the final plate to be removed easily from the mould.
Then the gum tacky tape is applied all along the perimeter of the mould, paying attention to the corners, because the bonding of the vacuum bag at the corners occurs to be one of the most critical part of the process.

3.3.3 Layers stacking

The correct sequence of the stacking layers necessary for a VARI infiltration is shown in Figure 3.11.

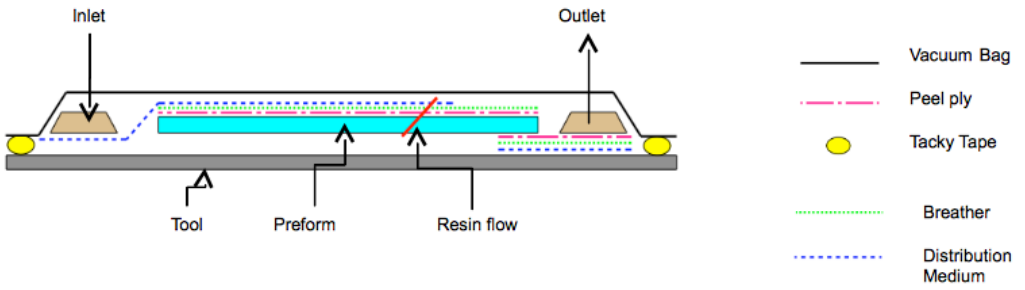

Figure 3.11: Correct stacking of the layers

Once the correct dimensions of the first lower peel ply, distribution medium, and breather layers are cut and are positioned on the mould, the preform can be added too. With more difficult mould shapes careful attention has to be paid. It is possible to use additional masking tape to hold in place the reinforcements and also the other materials. As it can be seen in Fig. 3.12, a perfect lay-up is essential for a good infusion.

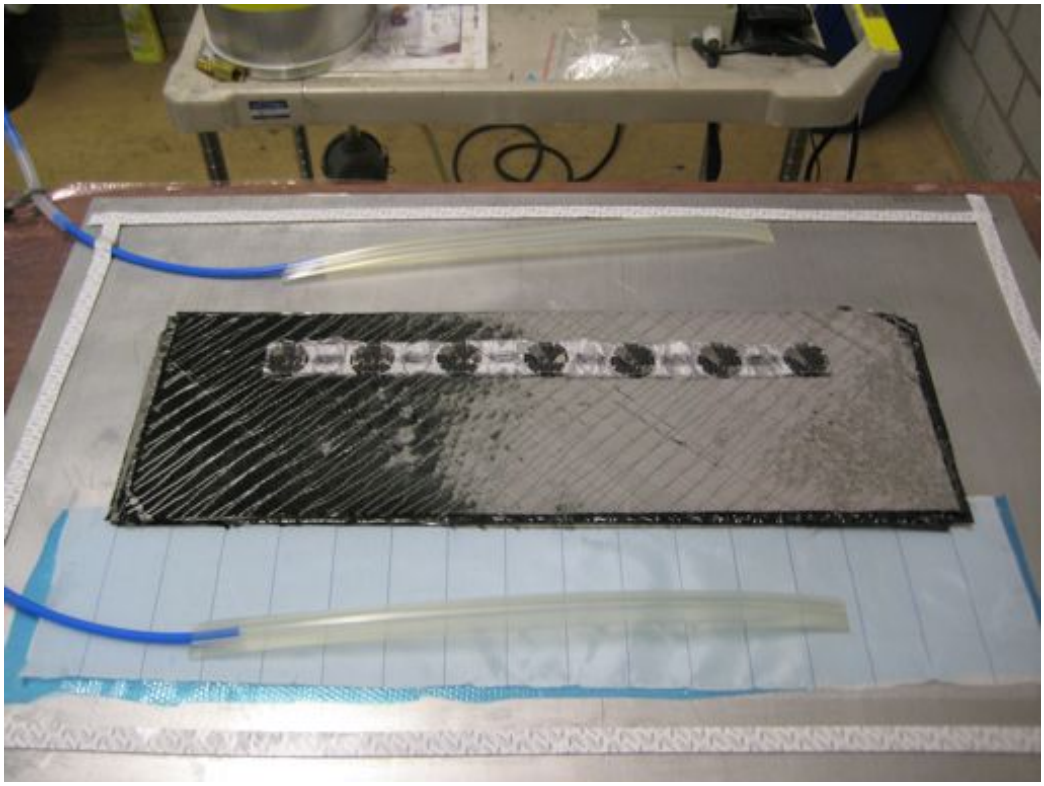

Figure 3.12: Lower layers, preform, and patches stacking

The distribution medium has to be a little wider than the width of the preform, so that two passages for the resin are created at the sides of the layers, in order to adjust the resin flow: in fact at the beginning these areas are more distant from the inlet, and this makes the resin to take more time to reach the sides of the preform. Moreover some space has to be left for the outlet, an Omega silicon profile, which is connected to the pump through PVC hoses. This should be as long as the preform, or a little shorter, in order to have the most possible uniform flow.
The Omega inlet (and outlet) should also be cut at each end in a diagonal profile, because the discontinuities created by the sharp edge could lead to folds in the bag. Also spirals can be used as inlets or outlets. Then the breather is placed over the distribution medium, covering the same area. The peel ply avoid the preform to get sticked to the vacuum bag, so it has to cover all the preform. The layers composing the preform are disposed according to the chosen stacking sequence, and then all the other layers are placed in the reverse order, as already explained in fig. 3.11. As the resin flows faster in the distribution medium than in the others material, the resin flow is diagonal through the thickness.

The upper distribution medium must end about 1 cm before the lower one, in order to allow the resin flow to become perpendicular to the mould plane, before it completes to infiltrate the preform. After all these steps, the build-up should look like fig. 3.15. The vacuum bag has to be cut larger and longer than the mould area, and then sealed to the mould with tacky tape. Pleats should be created, using extra loops of the gum tape, in the way out of the hoses from the bag, once again to avoid folds.

3.3.4 Resin and hardener

The amount of mixture (resin plus hardener) that is infiltrated should be enough to cover the entire volume of the layers. This will determine the final performances of the laminate, so it has to be chosen carefully. The ratio between resin and hardener depends on the nature of the two components. In every infusion it was chosen 100:34, according to the EPIKOTE indications. Once the two components are in the same cup with the exact ratio, they are mixed. This simple step is one of the trickiest, as additional attention has to be paid to avoid bubbles to enter the mixture. This undesiderable event would lead to an increase of the degassing time requested, and a lower time left for the infusion.

Figure 3.13: Mixing

Figure 3.14: Degassing

As the resin is drown to vacuum pressure during the infusion, a controlled degassing is requested before starting the infiltration. This is done at a very low pressure (5-10 mbar): it is important to keep this pressure lower than the 'vacuum pressure' that is used in the infiltration, otherwise this step would be useless. Degassing requires much more time if the mixture has a lot of bubbles, and this depends especially on how carefully the resin and the hardener have been mixed. Concerning the choice of the mixture components, in particular of the hardener, it has to be considered that the resin starts to

harden as soon as it's mixed with the hardener, and that its viscosity keeps decreasing. This would lead to a more difficult infusion as the time goes by. Once the mixture is degassed, it has to be placed in the container connected with the inlet in the vacuum bag.

3.3.5 Pump and containers

A pump is needed to drown the vacuum. There are several ways to connect it to the mould, the safest is to always use two metal containers, in order to avoid the resin to go into the pump, which would lead to catastrophic failure of the pump itself. The first one contains a cup with the resin and in the second one another empty cup is placed, which will receive the extra resin coming from the outlet. The cups are linked to the vacuum bag with silicon connectors. Once every layer is placed correctly, and the hoses are connected to the pump, several checks should be done to ensure that no voids let the air escape. Then vacuum (usually 30-40 mbar) can be drown, trying to avoid preferential ways of flowing, especially near the inlet, which could be caused by wrinkles and folds in the vacuum bag. This could be done manually opening the clamps, in order to let the air to be slowly pulled out with the pump.

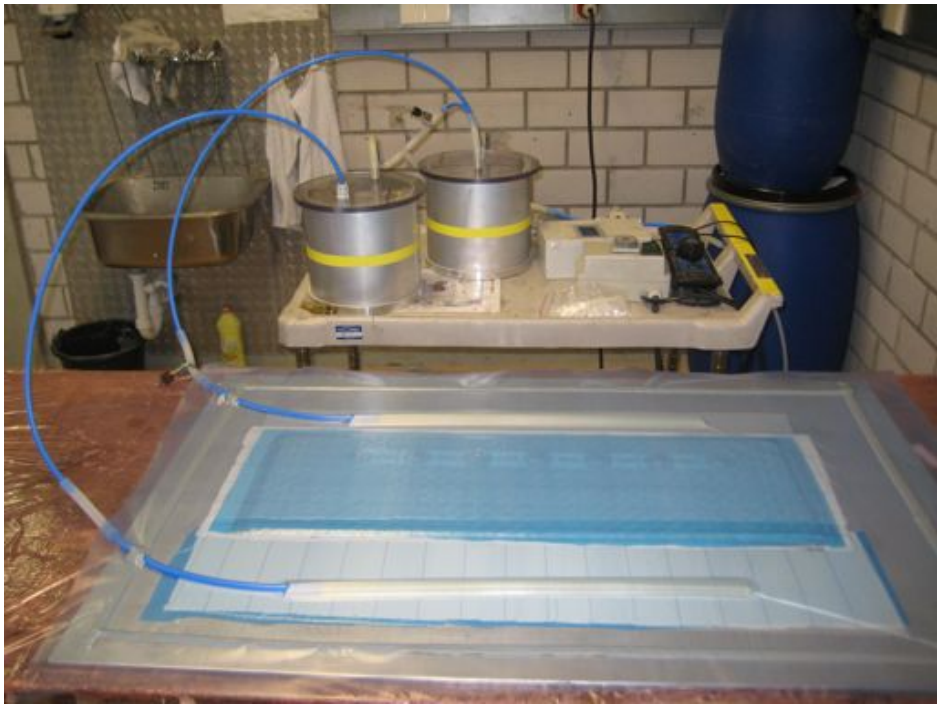

Figure 3.15: Vacuum drown into the system

3.3.6 Speed of the infusion

The speed of the resin flow follows the Darcy's law:

$$\vec{v} = [K]\frac{\nabla p}{\eta} \tag{3.1}$$

where:

- *[K]* : is the permeability tensor: it reports the attitude of the material to be soaked by a fluid.
- ∇p : is the pressure gradient.
- η : is the resin viscosity.

Or assuming an uni-directional flow, considering that the speed can be represented by the flow rate Q to the area:

$$\frac{Q}{A} = \frac{K}{\eta}(\frac{\nabla p}{L}) \tag{3.2}$$

where L is the way that the resin has to cover.
Because of this reason a low viscosity resin and high pressure are required. If the shape of the preform is complex, more inlets are usually used, and also a heating system for the resin, such as heated-plates or infrared devices, can be employed, in order to keep the viscosity at low levels.
According to this law, the resin flows faster in the more permeable materials, like the distribution medium. Besides, the resin starts slowly to cure as soon as it is mixed with the hardener, so its viscosity grows every minute, slowing down the infusion speed. In VARI process is more difficult to regulate the speed of the infusion than in other processes which use positive pressure to infiltrate the resin, like RTM. Initially, due to the maximum pressure gradient the infusion can be very fast, but as the time goes by, this suction force has to push even more resin through a wider surface, so the speed slows inevitably down. An operator can regulate manually the speed of the flow acting on the clamps, but only at the beginning of the infiltration. The speed depends on the width and the thickness of the layers, and it is up to experience of the operator.

3.3.7 Infiltration

The infiltration requires a pressure gradient, which means that in the container connected with the outlet there must be vacuum, therefore at the beginning this is sealed, while the other one, with resin, is left opened at ambient pressure. To start the resin flow the clamp between the inlet connector and the bag is slowly opened, and then regulated manually.
As stated before, attention must be paid not to speed up the flow front too much, and also to not let the infusion last more than the indicated resin curing time.

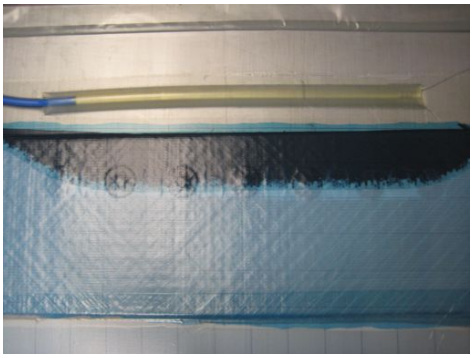

Figure 3.16: Infiltration: step 1

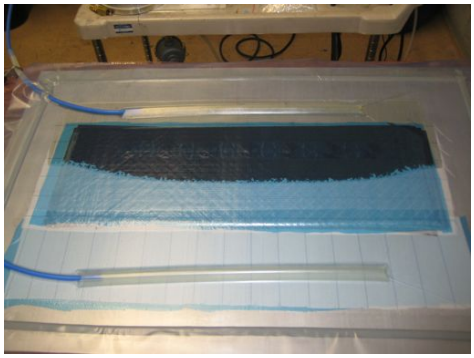

Figure 3.17: Infiltration: step 2

As it can be seen in the comparison between step 1 in Fig. 3.16, and step 2 in Fig. 3.16, even if at the beginning the resin flow is not uniform in the width of the layers, it regulates slowly thanks to the two corridors of distribution medium left at the two sides.

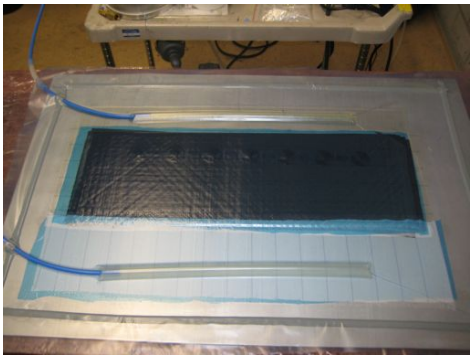

Figure 3.18: Infiltration: step 3

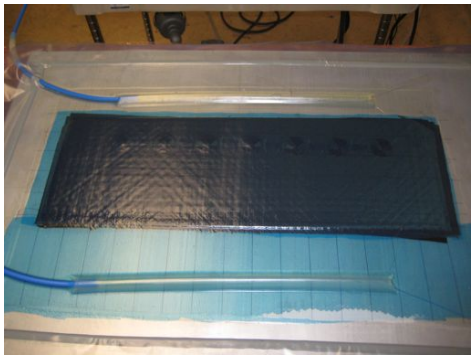

Figure 3.19: Infiltration: step 4

During this part, in the upper surface occasionally air bubbles trapped in the breather can be seen. In this particular infiltration, with patches laid

on top of the preform, more bubbles were highlighted. This was expected, due to the discontinuities created by the patches surface and the thickness variation.
When the resin has reached the end of the upper distribution medium, as shown in Fig. 3.18, usually the speed can no longer be regulated manually. Even if this seems to reach a more uniform distribution in width, the flow is still oblique in the thickness direction, as the resin flows faster in the upper side thanks to the more permeable materials. Therefore about 1 cm was left between the upper and the lower distribution media in order to let the resin redirect the flow in the out of plane direction.
Finally, when the resin completely fills the outlet Omega profile, the cup connected to the inlet is closed, and then in cups, hoses, and in the bag the pressure is set at 250-350 mbar. The curing pressure has great influence on the final fiber volume content. In fact, the lower the pressure inside the system, the higher the gradient pressure, which forces the resin outside the preform through the hoses up to the cups, increasing the fiber volume content. The resin is let curing for 24-48 hours, depending on the external environmental conditions.
After the separation of the laminate from the mould, the laminate shows a smoother surface on the side that was in contact with the metal plate, as expected. On the other side, the patches were easily recognizable, due to the relevant difference in local thickness.

3.3.8 Post-cure

Depending on the ambient conditions, especially external pressure and temperature, 24 hours could be not sufficient to obtain a rigid laminate. This would lead to a difficult separation of the plate from the mould, with the risk of ruining the lower surface, and hence a post-cure treatment can be necessary. Anyway, after the low pressure cure it is always highly recommended a post cure treatment to improve the laminate performance.
According to the guideline provided from the supplier for this combination of resin and hardener, the laminate was put for 15 hours in oven at 80°. Curing the resin at higher temperature than the glass transition temperature improves its performances, since the chaotic chemical bonds in the matrix have the possibility to redistribute and harden the laminate.

3.3.9 Mechanical Processing Techniques: Cutting, tabs, drilling

Once the plate is taken out of the oven, every single coupon was cut off the laminate with a diamond saw, but slightly larger than the correct dimensions, in order to save time and attach the glass tabs to the entire plate first. In case of the patches reinforced coupons, tabs were applied only on one edge, as on the other one the hole for the bearing test is drilled.
The glue for the tabs was prepared mixing A10/B10 hardeners[19] and then applied between the coupons and the tabs with the help of bench vises in order to hold them in the right position, and then let dry for 3 days at ambient temperature. Finally the specimens were cut with the correct width dimensions.

Figure 3.20: Tabs application, bench vises

Hole drilling was necessary both for the open-hole investigation and for the bearing tests. Composite materials are very sensitive to drilling. A notch can introduce in the laminate relevant border effect even from a theoretical point of view in an ideal manufactured laminate: it damages the hole region

because of the mechanical action acting on the surface. When a composite laminate is drilled, the lower surface must have a back up plate to avoid delaminations [20].

Figure 3.21: Drilling on a bearing coupon

A correct blocking system, in this case exploited with a bench vise as shown in Fig. 3.21, is requested, to avoid other possible damaging due to the vibrations of the drilling machine.

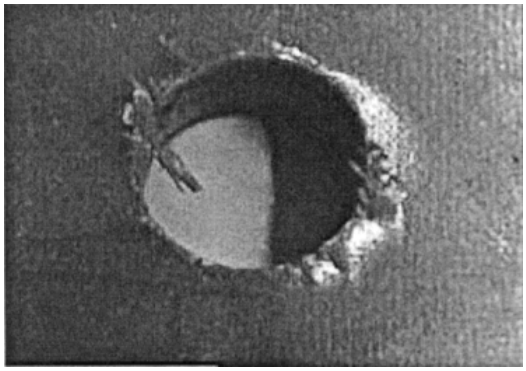

Figure 3.22: Delaminatios and pull-out of fibers in a holed laminate[20]

3.4 ARAMIS measuring system

In case of holed specimens, a classical measurement configuration it's not possible, because the reduced space at the middle section of the coupons does not allow the placement of strain gauges. Hence, the ARAMIS [21] non-contact optical 3D deformation measuring system was used. This system analyzes, calculates and collects the field of surface deformations of an object in digital camera images, allocating coordinates to the image pixels. The graphical representation of the results provides an understanding of the behavior of the measured object. The first image taken represents the undeformed state of the object, then, during and after the deformation of the coupon, further images are recorded. ARAMIS compares the digital images and calculates displacements and deformations of the investigated object.

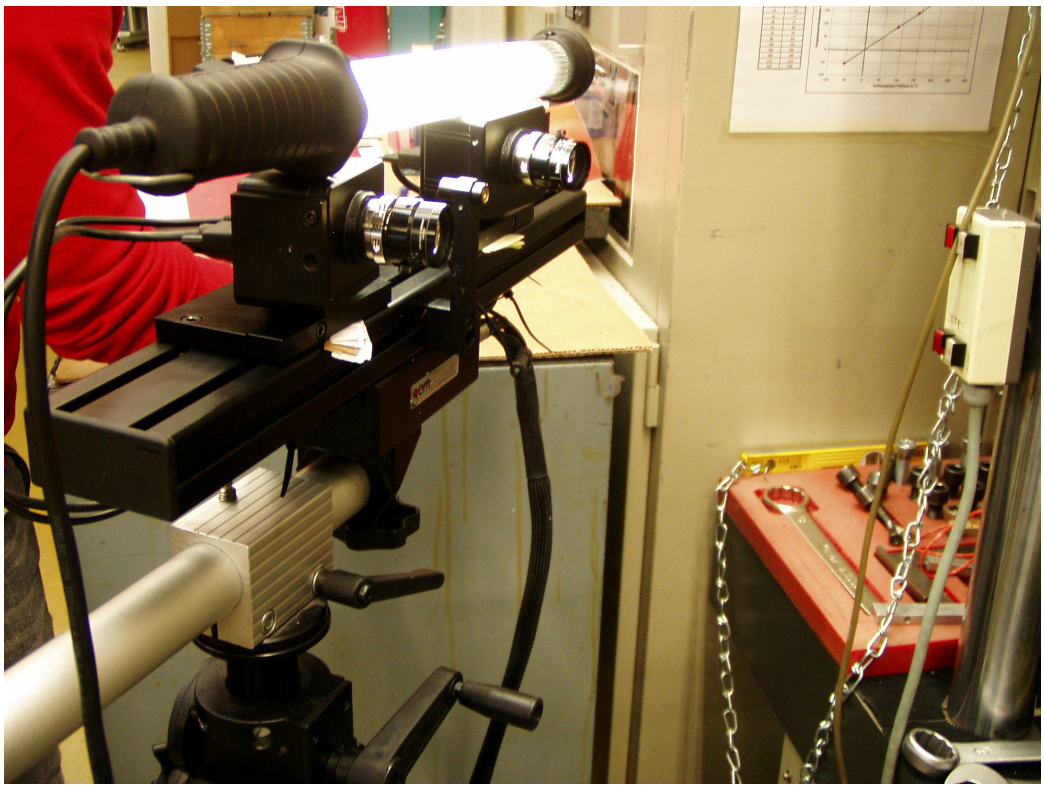

Figure 3.23: ARAMIS camera system

In order to recognize the surface and record the deformations, such surfaces have to be prepared by means of suitable methods, e.g. by spraying randomly a colored pattern, as shown in Fig. 3.24. The most common way to reproduce it, is the use of a white painted base on where black spots are

applied, for example dabbing a brush previously dipped with black paint. More than the dimensions of the points, it is very important to create a stochastic points distribution.

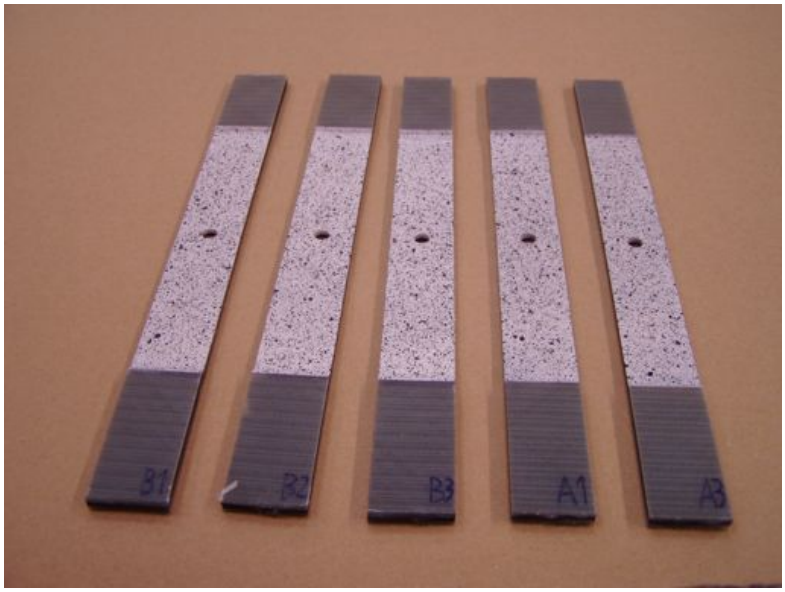

Figure 3.24: Coupon ready for the test

The camera system has to be calibrated before the test. The distance of the cameras and their orientation must be defined. In addition, the properties of the lenses have to be set (e.g. focus, lens distortions).

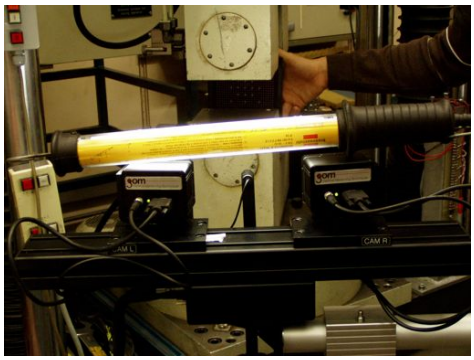

Figure 3.25: Camera calibration: panel with two scale bar

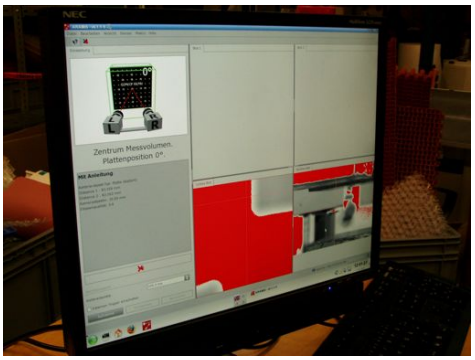

Figure 3.26: ARAMIS camera calibration

This kind of measuring system is faster than strain gauges, which have to be applied to the surface, and then connected and calibrated to the acqui-

sition system. Moreover, instead of a local deformation measure, it provides the entire field of strains on the surface of the measuring object.

3.5 Testing machine

After all the steps explained above, the coupons are ready to be tested. A Schenck-Trebel test machine was used. It has three load cells, which can measure up to 25 kN, 250 kN, and 500 kN, and can apply tensile, compressive, or a twist force. It can record the applied force, displacements and strains, if strain gauges are provided. The signal acquired is converted with a Spider 8 measurement amplifier into a digital signal in the HBM software Catman Professional, at a sampling rate of 200 ms. All the tests were controlled in displacement and with a upper load cell displacement rate of 2mm/min, without ramp-up.

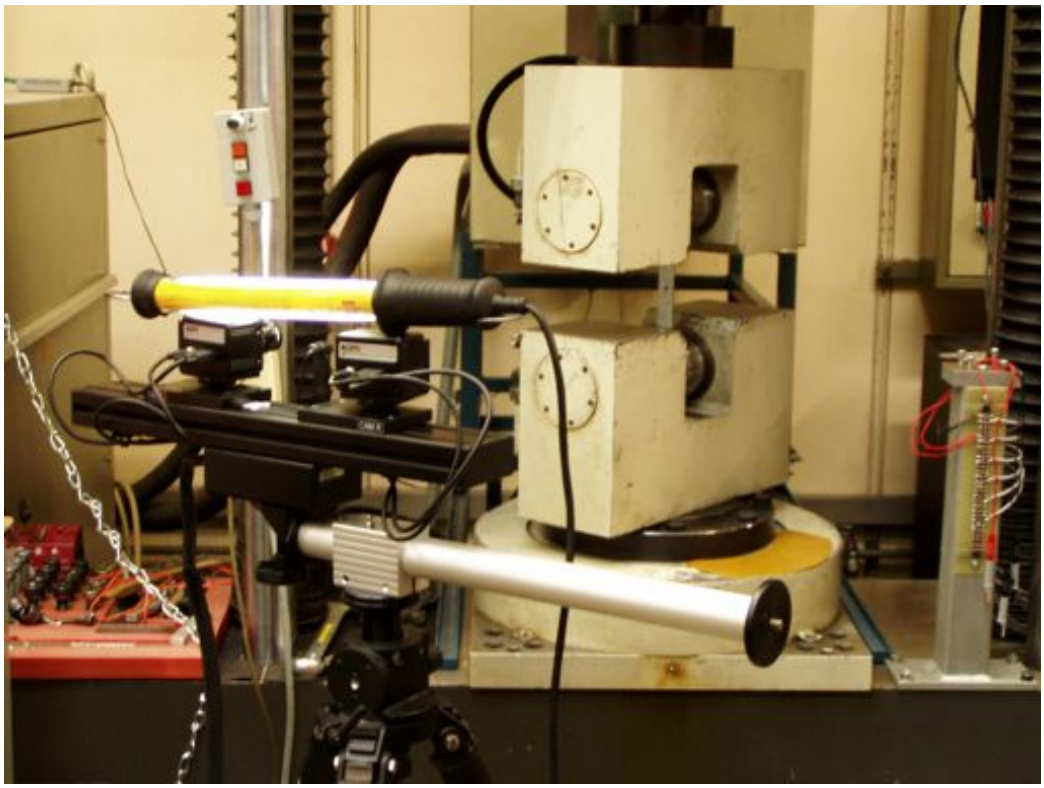

Figure 3.27: Testing machine and ARAMIS measurement system

Chapter 4

Material model parameters identification and discussion

In this chapter it is described how the investigated material was calibrated. Some parameters are requested for PAM-CRASH^{TM}in order to represent the mechanical properties of the material. A good calibration is a crucial step when it comes to Finite Element investigation. Without a good comprehension of how every parameter influences the mechanical response, the setup of complex models would not be enough accurate.
Firstly, the theoretical model presented by Ladevèze et al.[22] is introduced. Then the calibration of the parameters is described, starting from the experimental data.
In this project different formulations of elements were used: for the composite parts, due to the particular choice of crushing code here used to represent the bearing behavior, only SHELL elements were used, while for the text fixture, as well as for bolts, BEAM and SOLID formulation were employed.

4.1 Shell element formulation: PAM-CRASH Input Cards

All the numerical simulations that have been carried out at the Institut für Flugzeugbau of the University of Stuttgart were run with the explicit solver PAM-CRASH^{TM}[23]. In this code, three basic cards have to be defined to represent a shell element:

- SHELL PART. These cards contain basic information like the layers frame of reference and the thickness of the shells. They require the material cards as input.

- MATERIAL TYPE 131: MULTILAYERED SHELL ELEMENT. These cards contain information about material density, number of plies in the laminate and stacking sequence. Here the thickness of the ply and the fiber angle is provided too. It is also possible to define a control on hourglassing modes. Moreover, complementary output can be here defined, in order to get information on stresses, strains and damage in the desired ply.
- PLY MODEL TYPE 1: UNIDIRECTIONAL COMPOSITE GLOBAL PLY. These cards contain all ply mechanical data for stiffness, damage and failure.

4.1.1 Material Card definition

In PAM-CRASH^{TM}database several cards are available to correctly represent a composite material. Different element formulations can be chosen. In the numerical model built in this project CFRP were represented by Material type 131, which corresponds to multilayered and multi-material shell models [23]. The layers consist of materials modeled as elastic damaging fiber-matrix (bi-phase or global) composite.

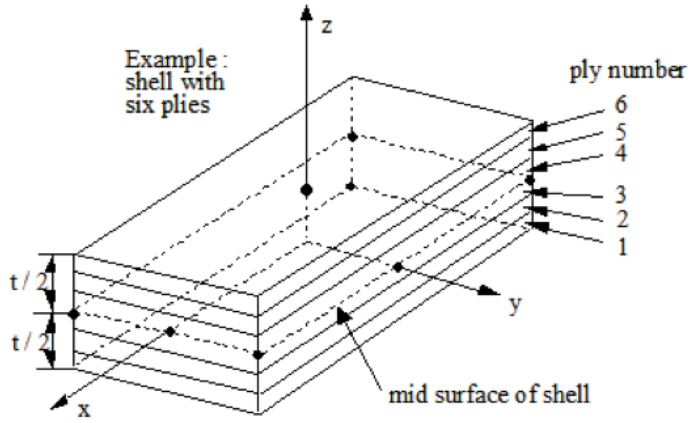

Figure 4.1: Material type 131: layered shell and reference frame [23]

Every material card contains different layers. Every ply card, numbered consecutively from the lower side to the upper side in the normal direction, as shown in Fig. 4.1, contains all the mechanical information of the material. The methodologies discussed in the following sections are based on the assumption that the failure behavior of a laminate can be sufficiently predicted

if the failure behavior of the single ply under arbitrary loading conditions is known [24]. The failure criteria are applied for each ply independently, and it is assumed that the physical material properties for ply failure do not depend on the stacking sequence and are not influenced by the adjacent plies.

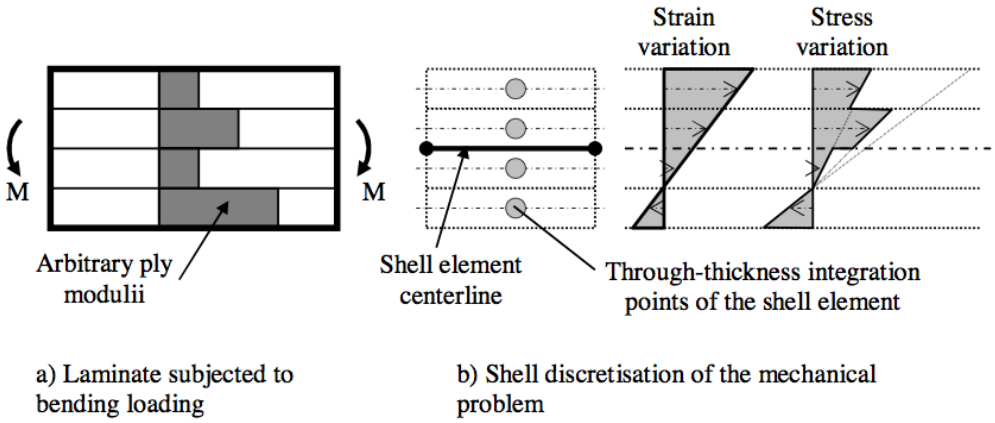

Figure 4.2: Numerical integration: Representation of a laminate as stacked UD lamina [24]

The mechanical response of a laminate is obtained by the through-the-thickness summation of all laminate layers in the simulation code, as shown in Fig 4.2. Each ply is represented by a corresponding integration point through the thickness of the shell.
Commercial crash codes use special shell element formulations, based on the Mindlin/Reissner plate theory ([25], [26]), which have been adapted in order to use a multi-layered ply approach representing the composite laminate [24]. Belytschko et al. proposed a shell element formulation for the explicit time integration method, which is implemented in several commercial simulation codes ([23], [27]). A shell element is particularly suitable for crash simulation, due to its efficiency and robustness [28].

4.1.2 Orthotropic reference frame

The ply coordinate system (1,2,3) is defined so that the first axis (1) coincides with the fiber direction; the second axis (2) corresponds to the left perpendicular direction in the plane of a unidirectional ply, and the third axis (3) is normal to the plane composed by the first two. The material parameters are defined with respect to the natural coordinates of orthotropy.

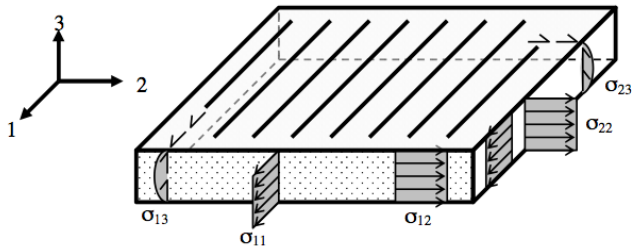

Figure 4.3: Ply coordinate system

4.1.3 Elastic behavior of an UD lamina

The Ladevèze model is addressed to the numerical simulation of unidirectional continuous fiber reinforced composite material. Unlike the heterogeneous 'bi-phase' model, the Ladevèze model does not treat two phases separately (fibers and matrix), i.e. the composite ply is described using homogeneous continuum mechanics.
The general Hook's law describes the elastic stress-strain response of a 3D continuum [29],

$$\{\sigma^0\} = [C^0]\{\varepsilon^e\} \tag{4.1}$$

where $\{\sigma^0\}$ is a general stress vector, $[C^0]$ is the general stress-strain constitutive matrix and $\{\varepsilon^e\}$ is the general elastic strain vector. The compliance matrix $[S^0]$ is obtained inverting the constitutive matrix,

$$[S^0] = [C^0]^{-1} \tag{4.2}$$

and allows to evidence the elastic strain:

$$\{\varepsilon^e\} = [S^0]\{\sigma^0\} \tag{4.3}$$

Considering a thin, orthotropic, and transversely isotropic lamina, the elasticity matrix can be significantly reduced. Moreover, normal out of plane

stresses $\{\sigma_{33}^0\}$ are neglected in this shell formulation. The stress-strain relation is simplified, and defined in the ply reference frame, as

$$\begin{bmatrix} \varepsilon_{11}^e \\ \varepsilon_{22}^e \\ 2\varepsilon_{12}^e \\ 2\varepsilon_{23}^e \\ 2\varepsilon_{13}^e \end{bmatrix} = \begin{bmatrix} \frac{1}{E_{11}} & -\frac{\nu_{21}^0}{E_{22}^0} & 0 & 0 & 0 \\ -\frac{\nu_{12}^0}{E_{11}} & \frac{1}{E_{22}^0} & 0 & 0 & 0 \\ 0 & 0 & \frac{1}{G_{12}^0} & 0 & 0 \\ 0 & 0 & 0 & \frac{1}{G_{23}^0} & 0 \\ 0 & 0 & 0 & 0 & \frac{1}{G_{12}^0} \end{bmatrix} \begin{bmatrix} \sigma_{11} \\ \sigma_{22} \\ \sigma_{12} \\ \sigma_{23} \\ \sigma_{13} \end{bmatrix} \tag{4.4}$$

where E_{11} and E_{22}^0 are the lamina moduli in the fiber and transverse direction, ν_{ij}^0 is the Poisson's coefficient, and G_{ij}^0 represent the shear modulus. Remembering the symmetry of $[S^0]$, the matrix is further simplified:

$$E_{22}^0 \nu_{12}^0 = E_{11} \nu_{21}^0 \tag{4.5}$$

The initial stress-strain constitutive matrix of a thin orthotropic lamina is obtained by inverting the upgraded compliance matrix $[S^0]$:

$$\left[C^0\right] = \begin{bmatrix} C_{11}^0 & \nu_{21}^0 C_{11}^0 & 0 & 0 & 0 \\ \nu_{21}^0 C_{11}^0 & C_{22}^0 & 0 & 0 & 0 \\ 0 & 0 & G_{12}^0 & 0 & 0 \\ 0 & 0 & 0 & G_{23}^0 & 0 \\ 0 & 0 & 0 & 0 & G_{12}^0 \end{bmatrix} \tag{4.6}$$

with

$$C_{11}^0 = \frac{E_{11}}{1 - \nu_{12}^0 \nu_{21}^0} \tag{4.7}$$

$$C_{22}^0 = \frac{E_{22}^0}{1 - \nu_{12}^0 \nu_{21}^0} \tag{4.8}$$

4.1.4 The modified Ladevèze composite model

Composite materials exhibit brittle failure in the fiber direction, but it is well known that small cracks on a micro-scale appears prior to failure. Besides, the matrix dominated directions have a non linear behavior.
Ladevèze introduces elastic softening, depending on underlying loading state and loading history. This will be analyzed further in the calibration of the shear parameters.
Basically, the matrix related damage is taken into account by two scalar variables, d_{12} and d_{22}. These variables represent two experimental phenomena: parameter d_{12} quantifies the damage coming from the debonding between fibers and matrix, whereas parameter d_{22} is related to the damage due to the microcracking of the matrix in the fiber direction. Consequently parameters d_{12} and d_{22} are applied respectively to the ply shear and transverse moduli. Hence the damaged quantities are:

$$C_{22} = C_{22}^0(1 - d_{22}) \tag{4.9}$$

$$G_{12} = G_{12}^0(1 - d_{12}) \tag{4.10}$$

$$G_{23} = G_{23}^0(1 - d_{12}) \tag{4.11}$$

The compliance matrix is thereby modified:

$$\left[C^d\right] = \begin{bmatrix} C_{11}^0 & \nu_{21}^0 C_{11}^0 & 0 & 0 & 0 \\ \nu_{21}^0 C_{11}^0 & C_{22}^0(1-d_{22}) & 0 & 0 & 0 \\ 0 & 0 & G_{12}^0(1-d_{12}) & 0 & 0 \\ 0 & 0 & 0 & G_{23}^0(1-d_{12}) & 0 \\ 0 & 0 & 0 & 0 & G_{12}^0(1-d_{12}) \end{bmatrix} \tag{4.12}$$

So the new stress-strain relationship is expressed as follows:

$$\{\sigma\} = [C^d]\{\varepsilon^e\} \tag{4.13}$$

Damage is here expressed as the change in slope of the moduli G_{12} and E_{22} with the growth of the load level. This is directly correlated with the change of the stored elastic energy, and shows how the damage is progressing. However, tensile and compressive transverse responses must be distinguished, because the micro-cracks grow when the composite ply is under tensile transverse loading (the material gets weaker), but they close under compression

(the material gets stronger). Hence damage development is prohibited under matrix transverse compressive loading.
The damage elastic energy per unit volume is expressed as:

$$W_e^d = \frac{1}{2}\{\sigma\}\{\varepsilon^e\} \tag{4.14}$$

or, recalling the previous equations and neglecting the out of plane terms like γ_{13} or G_{23}^0,

$$W_e^d = \frac{1}{2}(E_{11}(\varepsilon_{11}^e)^2 + C_{22}^0(1-d_{22})(\nu_{12}^0\varepsilon_{11}^e + \varepsilon_{22}^e)^2 + (1-d_{12})(\sigma_{12}(\gamma_{12}^e)^2) \tag{4.15}$$

The damage governing functions, Y_{12} and Y_{22}, are defined separately for shear and transverse loading, by partial derivation of W_e^d against the damage parameters.

$$Y_{12} = -\frac{\partial W_e^d}{\partial d_{12}} = \frac{1}{2}\sigma_{12}(\gamma_{12}^e)^2 \tag{4.16}$$

$$Y_{22} = -\frac{\partial W_e^d}{\partial d_{22}} = \frac{1}{2}C_{22}^0(\nu_{12}^0\varepsilon_{11}^e + \varepsilon_{22}^e)^2 \tag{4.17}$$

Fitting d_{ij} and Y_{ij} with a linear or exponential curve, or by assigning the correspondent set of points, the explicit code is able to reproduce the non-linear elasticity.
The Ladevèze modified model can also take into account the plasticity of the matrix, using a simple yield condition:

$$f = \sqrt{\sigma_{12}^2 + a^2\sigma_{22}^2} - R - R_0 \tag{4.18}$$

where R_0 is the matrix shear yield stress, and R is the plastic strain hardening. If required, factor a^2 can introduce material anisotropy. Assuming an isotropic von Mises matrix material the factor yields 0.33 [23].
In the further sections it will be explained how to get accurate parameters from the experimental data, by means of a calibration process.

4.2 Determination of orthotropic elastic and failure properties from test measurements

An explicit solver can employ a non linear material formulation, as the one above mentioned, but requires some input parameters to reproduce the material behavior.
A comprehensive material characterization of the UD investigated in this work requires an extensive test program, which is divided into different sections. For the purpose of this study, data from previous tests performed at IFB on the investigated material were collected and elaborated in order to get the parameters necessary for the numerical model.
The principal intra-laminar deformation and failure mechanisms are investigated. For a UD material the tests required for its numerical characterization are:

- *Simple tension test on* $[0]_8$: elastic and failure properties
- *Simple compression test on* $[0]_8$: elastic and failure properties
- *Simple tension test on* $[90]_8$: transverse elastic and failure properties
- *Simple tension test on* $[\pm 45]_{2S}$: shear elastic properties
- *Cyclic tension test on* $[\pm 45]_{2S}$: shear damage and plasticity properties

This section explains how the parameters of the PLY card requested from PAM-CRASH were obtained.

4.2.1 Transformation between global and ply frame of reference

The characterization of material parameters requires the transformation of mechanical properties from the global test frame (L,T), according to which test data were initially provided, to the local ply frame (1,2). The angle between fibers and the load direction is called θ. In these tests, the load directions correspond to the laminate X,Y axis.

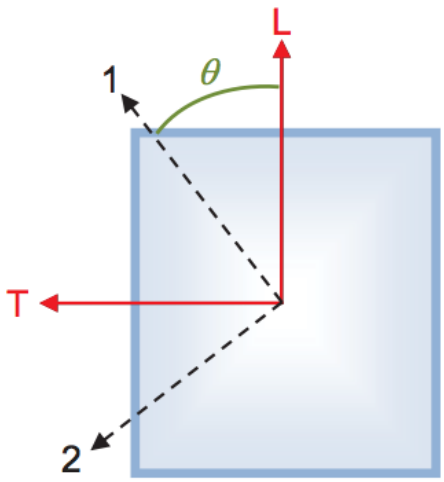

Figure 4.4: Global (L,T) and local (1,2) frame

A MATLAB^{TM}script allowed to extract the desired material constants. Results are computed from the test data, which store time, applied force, displacements longitudinal (L) and transverse (T) strains, the last two recorded by strain gauges.
The rotation matrices between the local and global stresses and strains in a given ply with fiber angle θ are given by:

$$\begin{bmatrix} \varepsilon_{11} \\ \varepsilon_{22} \\ 2\varepsilon_{12} \end{bmatrix} = \begin{bmatrix} cos^2\theta & sin^2\theta & cos\theta sin\theta \\ sin^2\theta & cos^2\theta & -cos\theta sin\theta \\ -2cos\theta sin\theta & 2cos\theta sin\theta & cos^2\theta - sin^2\theta \end{bmatrix} \begin{bmatrix} \varepsilon_L \\ \varepsilon_T \\ 2\varepsilon_{LT} \end{bmatrix} = \begin{bmatrix} Q_1 \end{bmatrix} \begin{bmatrix} \varepsilon_L \\ \varepsilon_T \\ 2\varepsilon_{LT} \end{bmatrix} \tag{4.19}$$

$$\begin{bmatrix}\sigma_{11}\\ \sigma_{22}\\ \sigma_{12}\end{bmatrix} = \begin{bmatrix} cos^2\theta & sin^2\theta & 2cos\theta sin\theta \\ sin^2\theta & cos^2\theta & -2cos\theta sin\theta \\ -cos\theta sin\theta & cos\theta sin\theta & cos^2\theta - sin^2\theta \end{bmatrix} \begin{bmatrix}\sigma_L\\ \sigma_T\\ 2\sigma_{LT}\end{bmatrix} = \Big[Q_2\Big] \begin{bmatrix}\sigma_L\\ \sigma_T\\ 2\sigma_{LT}\end{bmatrix} \tag{4.20}$$

This equation is simplified in the case of tensile test because then

$$2\varepsilon_{LT} = \sigma_T = \sigma_{LT} = 0 \tag{4.21}$$

The initial tensile elastic behavior law for each ply of the laminate is written as:

$$\begin{bmatrix}\sigma_{11}\\ \sigma_{22}\\ \sigma_{12}\end{bmatrix} = \begin{bmatrix} \dfrac{E_1^{0t}}{1-\nu_{12}^0\nu_{21}^0} & \dfrac{\nu_{21}^0 E_1^{0t}}{1-\nu_{12}^0\nu_{21}^0} & 0 \\ \dfrac{\nu_{12}^0 E_1^{0t}}{1-\nu_{12}^0\nu_{21}^0} & \dfrac{E_2^{0t}}{1-\nu_{12}^0\nu_{21}^0} & 0 \\ 0 & 0 & G_{12}^0 \end{bmatrix} \begin{bmatrix}\varepsilon_{11}\\ \varepsilon_{22}\\ 2\varepsilon_{12}\end{bmatrix} = \Big[C^0\Big] \begin{bmatrix}\varepsilon_{11}\\ \varepsilon_{22}\\ 2\varepsilon_{12}\end{bmatrix} \tag{4.22}$$

The stresses inside each ply with an angle θ are given in the global frame using the identity:

$$\Big[Q_2\Big]^{-1} = \Big[Q_1\Big]^T \tag{4.23}$$

$$\begin{bmatrix}\sigma_L\\ \sigma_T\\ \sigma_{LT}\end{bmatrix}^\theta = \Big[Q_1\Big]^T \begin{bmatrix}\sigma_{11}\\ \sigma_{22}\\ \sigma_{12}\end{bmatrix} = \Big[Q_1\Big]^T \Big[C^0\Big] \begin{bmatrix}\varepsilon_{11}\\ \varepsilon_{22}\\ 2\varepsilon_{12}\end{bmatrix} = \Big[Q_1\Big]^T \Big[C^0\Big] \Big[Q_1\Big] \begin{bmatrix}\varepsilon_L\\ \varepsilon_T\\ 2\varepsilon_{LT}\end{bmatrix} \tag{4.24}$$

4.3 Simple tension test on $[0]_8$

The parameters obtained from a simple tension test on $[0]_8$ coupons are:

- E_1^{0t}: the tensile initial Young's modulus in the direction of the fibers.
- ν_{12}^0: the Poisson's ratio in plane (1,2).
- ε_i^{ft}, ε_u^{ft}, d_u^{ft} : the critical strain thresholds and the ultimate damage corresponding to fibre rupture.

Besides classical calibration strategies, ε_i^{ft}, ε_u^{ft}, d_u^{ft} parameters are present in PAM CRASH code in order to introduce both tensile and compressive modulus damaging. As it can be seen in Fig. 4.5, the typical brittle fiber failure is modified to prevent elements from breaking too quickly, which would lead to numerical instabilities. ε_i^{ft}, ε_u^{ft} can slow down the breaking process, while d_u^{ft} allows to consider an asymptotic ultimate damage.

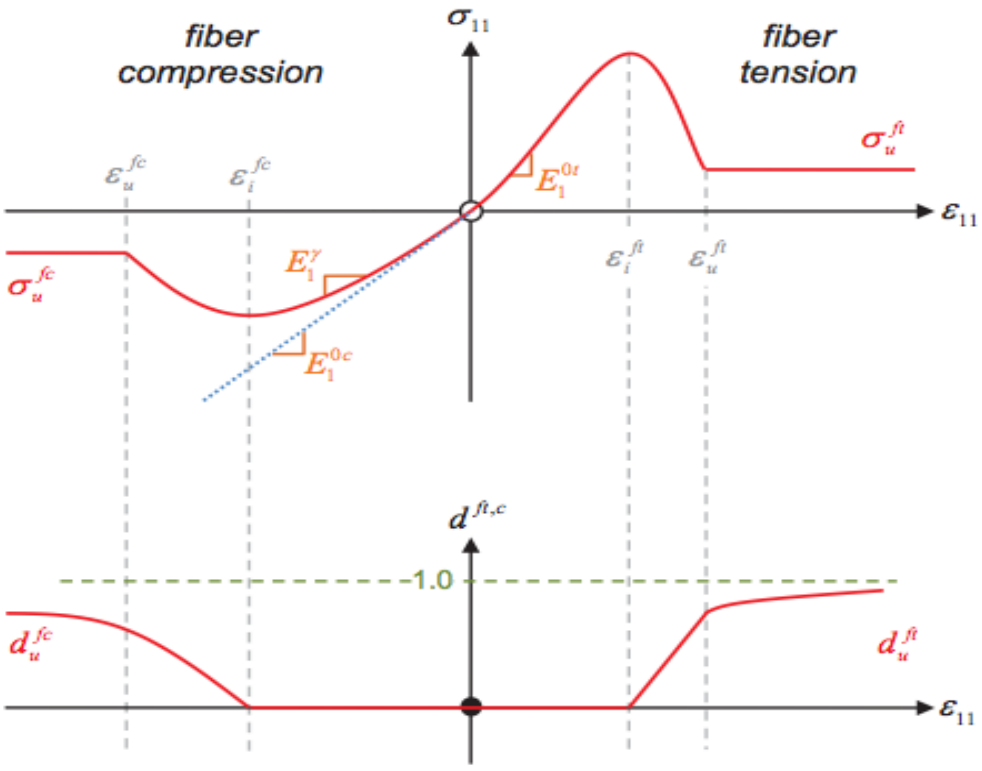

Figure 4.5: Fiber Tensile Damage, [23]

It can be noticed that the compressive section requires an extra parameter which consider the non linear behavior, Fig. 4.5. This will be further investigated in the compressive parameter calibration section.
According to the Ladevèze model, longitudinal tensile E modulus calculations can be summarized as follows:

- *Sub-critical*:

$$E_1 = E_1^{0t} \tag{4.25}$$

- *Critical*:

$$E_1 = E_1^{0t}(1 - d^{ft}), d^{ft} = d_u^{ft}\frac{\varepsilon_{11} - \varepsilon_i^{ft}}{\varepsilon_u^{ft} - \varepsilon_i^{ft}} \tag{4.26}$$

- *Post-critical*:

$$E_1 = E_1^{0t}(1 - d^{ft}), d^{ft} = 1 - (1 - d_u^{ft})\frac{\varepsilon_{11}}{\varepsilon_u^{ft}} \tag{4.27}$$

E_1^{0t} and ν_{12}^0 were calculated according to the standards of the American Society for Testing and Materials ASTM D 3039/D 3039M [30]. These defines standard methods and specifications for a tensile test.
According to section 4.2.1, from strain gauges placed at the center of the coupons in longitudinal and transverse direction, ε_L and ε_T, stresses and strains in local coordinates were computed.

$$\begin{bmatrix}\sigma_{11}\\ \sigma_{22}\\ \sigma_{12}\end{bmatrix} = \begin{bmatrix}\sigma_L\\ 0\\ 0\end{bmatrix} \; and \; \begin{bmatrix}\varepsilon_{11}\\ \varepsilon_{22}\\ 2\varepsilon_{12}\end{bmatrix} = \begin{bmatrix}\varepsilon_L\\ \varepsilon_T\\ 0\end{bmatrix} \tag{4.28}$$

From the analysis of the data the ultimate strength is calculated according to the standards. The force collected at each instant of the test is divided by the initial measured area of the coupons, obtaining the stress time history:

$$\sigma_{Li} = \frac{F_i}{A} \tag{4.29}$$

Deformations are obtained directly from strain gauges through the CATMAN program, as shown in section 3.5. The tensile E-modulus is then calculated:

$$E_1^{0t} = \frac{\Delta\sigma_L}{\Delta\varepsilon_L} \tag{4.30}$$

The norms define a specified range in which the E_1^{0t} can be computed, as it can be seen in the following figures:

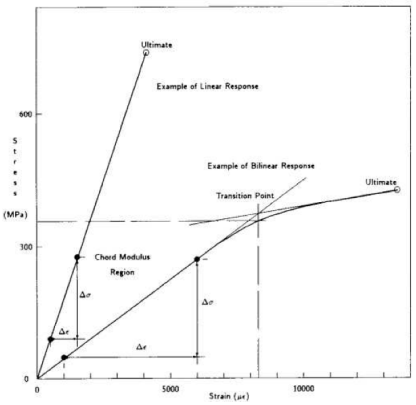

Figure 4.6: Simple tension test on $[0]_8$ coupons, ASTM standards

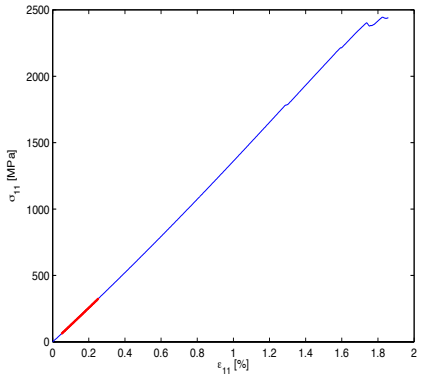

Figure 4.7: Coupon 0.8, identification of E_1^{0t}

Experimental data of 5 coupons tested at IFB were collected. The average value for stiffness and failure data are outlined in the table below, where values in italics font are not included in the computation, resulting from unreliable tests.

Table 4.1: Simple tension test on $[0]_8$, 6 coupons

Specimen	E_1^{0t} [GPa]	ν_{12}^0 [-]	ε_i^{ft} [%]
0.8	124.783	0.3280	1.9842
0.9	131.975	0.2790	1.7990
0.10	129.925	0.2587	1.8574
0.11	117.700	0.2930	1.8950
0.11b	132.241	0.3710	*2.5802*
0.12	*109.35*	*0.2728*	*6.5129*
Mean values	**127.325**	**0.3059**	**1.8839**

Since the typical brittle failure of a tensile test would lead to a very small difference between ε_i^{ft} and ε_u^{ft}, the value of ε_u^{ft} was set at 2, a value quite bigger than the experimental results, in order not to let the element break too quickly and to avoid possible numerical instabilities. An ultimate damage d_u^{ft} of 1.0 was set.

4.3.1 Numerical calibration

The numerical calibration is based on the study of a single element, with supports and loading as shown in Fig.4.8. This simple setup ensures that the element is properly supported and has pure tension loading in the x-direction with free contraction in y-direction.

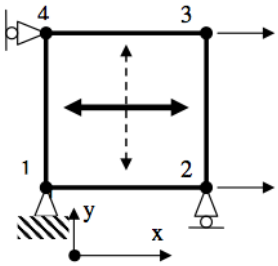

Figure 4.8: Single element calibration

The results of the calibration of a single element are here reported and compared to the experimental data.

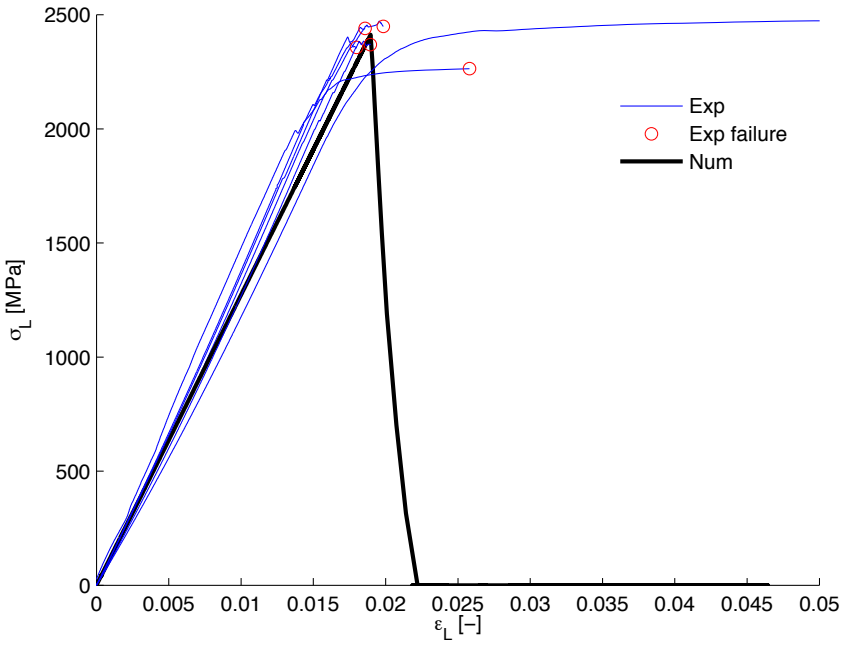

Figure 4.9: Tensile calibration $[0]_8$

4.4 Simple tension test on $[90]_8$

This test allows to find the transverse elastic modulus E_2^0.
Six samples were tested to rupture. Value in italics were not computed for the average values, as the first two coupons have higher slopes and fail near the tabs, which made their results unreliable.

Table 4.2: Simple tension test on $[90]_8$, 6 coupons

Specimen	E_2^0 [GPa]	Ultimate stress [MPa]
15.01	*11.6808*	*37.523*
15.02	*11.0830*	*41.876*
15.03	9.0851	42.033
15.04	9.913	41.560
15.05	9.8013	40.542
15.06	10.072	42.597
Mean values	**9.898**	**41.683**

The results of the experimental data are compared in Fig.4.11.

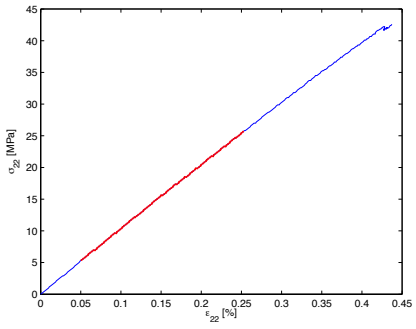

Figure 4.10: Simple tension test on $[90]_8$, coupon 15.06: E_2^0

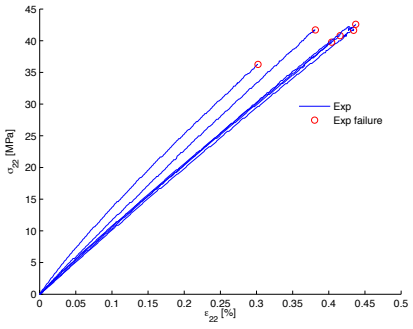

Figure 4.11: Simple tension tests on $[90]_8$, comparison 6 coupons

4.5 Simple compression test on $[0]_8$

This test allows to find:

- E_1^{0c}: the compressive initial Young's modulus in the direction of fibers.
- γ: the corrective factor for non-linear fiber compressive behavior,
- ε_i^{fc}, ε_u^{fc}, d_u^{fc} : the critical strains and ultimate damage corresponding to compressive fiber value

Compression coupons are smaller than the tensile coupons, in order to prevent buckling effects. According to ASTM standards, 5 coupons with length of 110 mm, width of 10 mm and thickness of 2 mm, were tested.
Once the experimental data are obtained, parameters E_1^{0c}, ε_i^{fc}, ε_u^{fc}, d_u^{fc} are evaluated in the same way of the tension test: a single element under appropriate constraints is loaded under compression, and then correlated with tests, as it can be seen in Fig. 4.12:

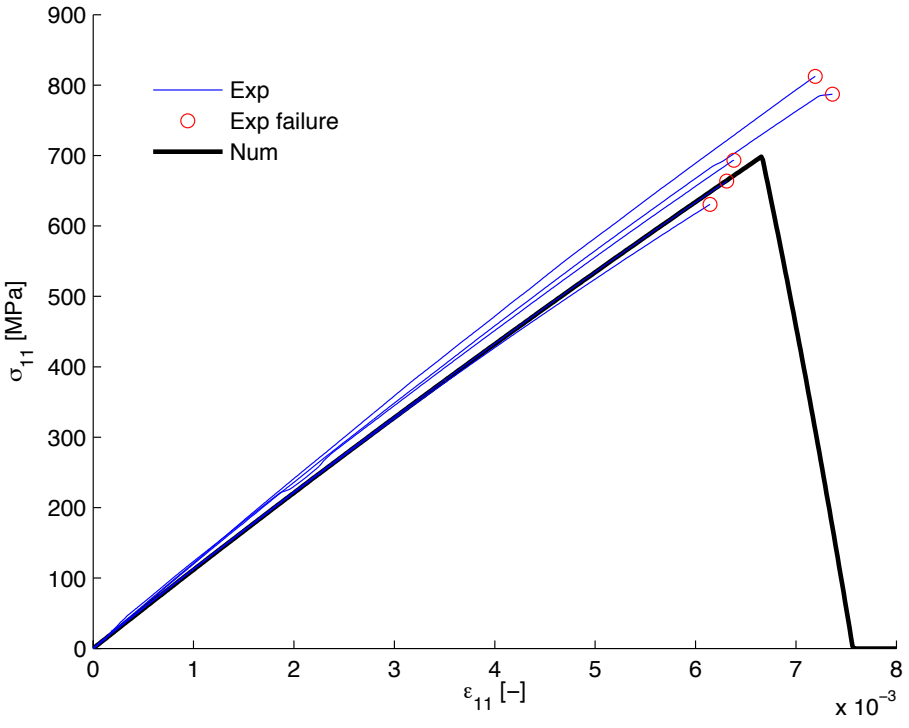

Figure 4.12: Compression experimental tests on $[0]_8$ coupons and calibration

This test, even if carried out according to ASTM standards, leads to a highly non-uniform strain field. The strain gauges record local deformations, and this is one of the reason why the slope of calibrated tension and compression calibrated curves can be quite different.

4.5.1 Nonlinear fiber compressive behavior

Fiber misalignment, crimping and fiber micro-buckling phenomena can lead to a non-linear behavior in the fiber direction under a compressive load. These phenomena are one of the main causes of the bearing mechanical response, therefore their characterization is very important.

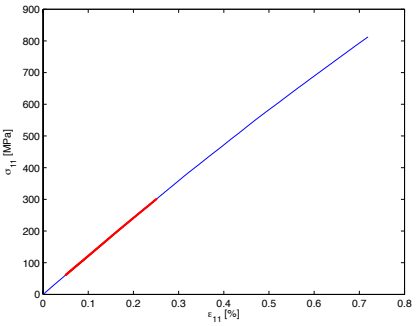

Figure 4.13: Compressive calibration $[0]_8$, coupon 4.2: E modulus

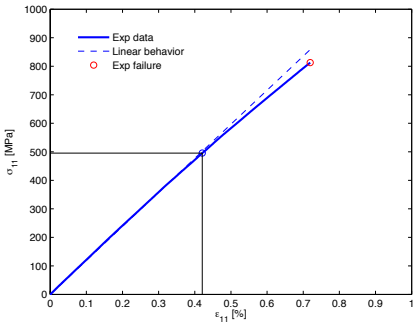

Figure 4.14: Compressive calibration $[0]_8$: non linear behavior

Fig. 4.13 shows the interval in which the E compressive moduli were computed. The longitudinal Young modulus can decrease under compression because of a non linear behavior which can be quantified by the introduction of a factor γ, so that the effective undamaged fiber modulus in compression is given by:

$$E_1^{\gamma} = \frac{E_1^{0c}}{1 + \gamma E_1^{0c} |\varepsilon_{11}|} \tag{4.31}$$

where ε_{11} is the strain at which the elastic curve loses its linear behavior, as it can be seen in Fig. 4.14.
In Table 4.3 values obtained for each coupon are reported.

Table 4.3: Simple compression test on $[0]_8$

Specimen	E_1^{0c} [MPa]	E_1^{γ} [MPa]	γ [-]
4.1	116.422	112.085	0.0604
4.2	119.345	115.695	0.0480
4.3	112.854	110.287	0.0374
4.6	109.095	106.275	0.0442
4.7	107.501	103.317	0.0684
Mean values	**113.043**	**109.532**	**0.0517**

4.6 Simple tension tests on $[\pm 45]_{2S}$

This test allows to find the shear modulus in the ply plane G_{12}^0. Once again, from the data collected in the global reference frame, local stresses and strains have to be computed:

$$\begin{bmatrix} \sigma_{11} \\ \sigma_{22} \\ \sigma_{12} \end{bmatrix} = \begin{bmatrix} 0 \\ 0 \\ \dfrac{\sigma_L}{2} \end{bmatrix} \; and \; \begin{bmatrix} \varepsilon_{11} \\ \varepsilon_{22} \\ 2\varepsilon_{12} \end{bmatrix} = \begin{bmatrix} 0 \\ 0 \\ \varepsilon_L - \varepsilon_T \end{bmatrix} \tag{4.32}$$

From now on the real shear strain $2\varepsilon_{12}$ will be called as the engineering shear strain, γ_{12}. According to ASTM standard, stresses and strains for the computation of G_{12}^0 have to be calculated as for the other tests, but within an interval of 0.1% γ_{12} and 0.5% γ_{12}, as shown in Fig.4.15.

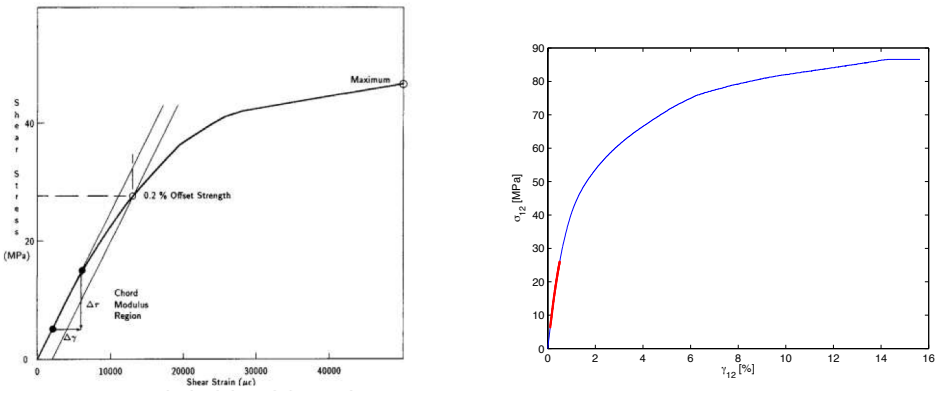

Figure 4.15: ASTM standards, simple tension test on $[\pm 45]_{2S}$, coupon 2.4

It can be seen that the presence of the matrix influence significantly the behavior of the material, so that non linearity appears in the mechanical response. The experimental data collected from 4 coupons are reported in the following table:

Table 4.4: Simple tension tests on $[\pm 45]_{2S}$

Specimen	G_{12}^0 [GPa]	Ultimate stress [MPa]
2.1	5.1540	84.40
2.2	4.9415	88.10
2.3	5.0167	85.30
2.4	4.9417	87.80
Mean values	**5.0135**	**86.4**

4.7 Cyclic tension tests on $[\pm 45]_{2S}$

Cyclic tension tests with increasing load level were performed on 4 coupons to obtain the evolution of shear damage and plasticity in the investigated material.

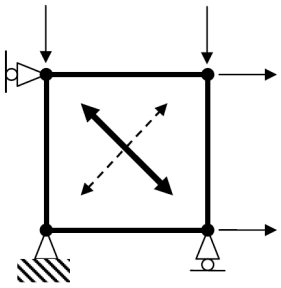

Figure 4.16: Shear single element calibration

A single element is modeled in PAM CRASH and constrained as shown in fig. 4.16.
The typical cyclic curve is reported in Fig. 4.17.

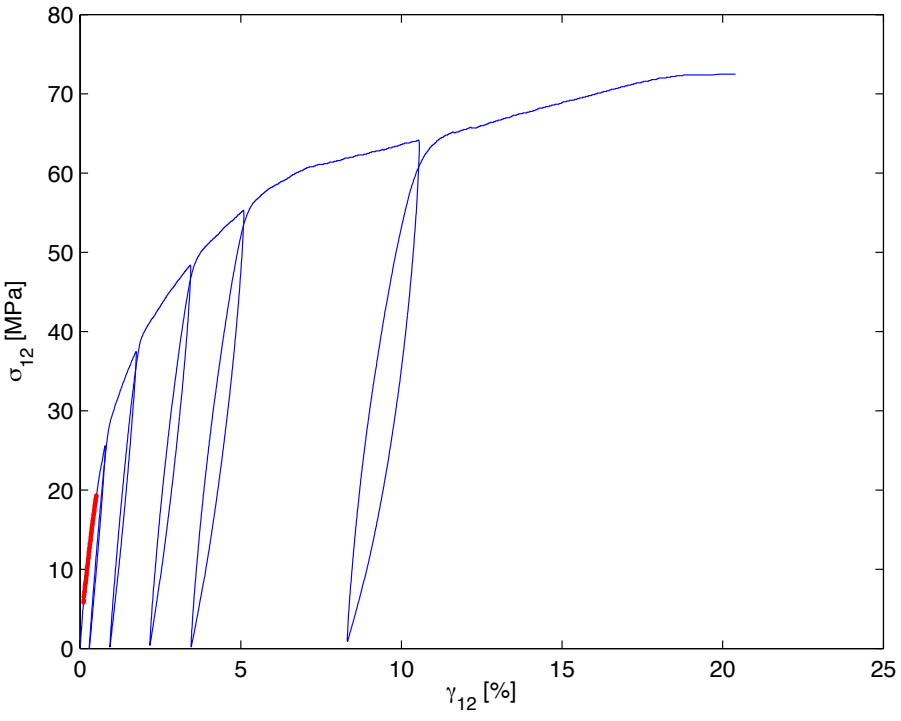

Figure 4.17: Cyclic tension test on $[\pm 45]_{2S}$, coupon 2.6

4.7.1 Elastic matrix damaging behavior

As explained in section 2.1, the modified Ladevèze model uses two scalar variables to represent the evolution of shear damage. The relation between damage and damage governing function can be included in the code with an auxiliary function, an exponential or a linear curve: in the last case it is represented as:

$$Y_{12} = Y_C \cdot d_{12} + Y_0 \tag{4.33}$$

considering

- Y_C: the critical shear damage limit.
- Y_0: the initial shear damage limit.
- Y_R: the elementary shear damage fracture limit, to be assigned aside.

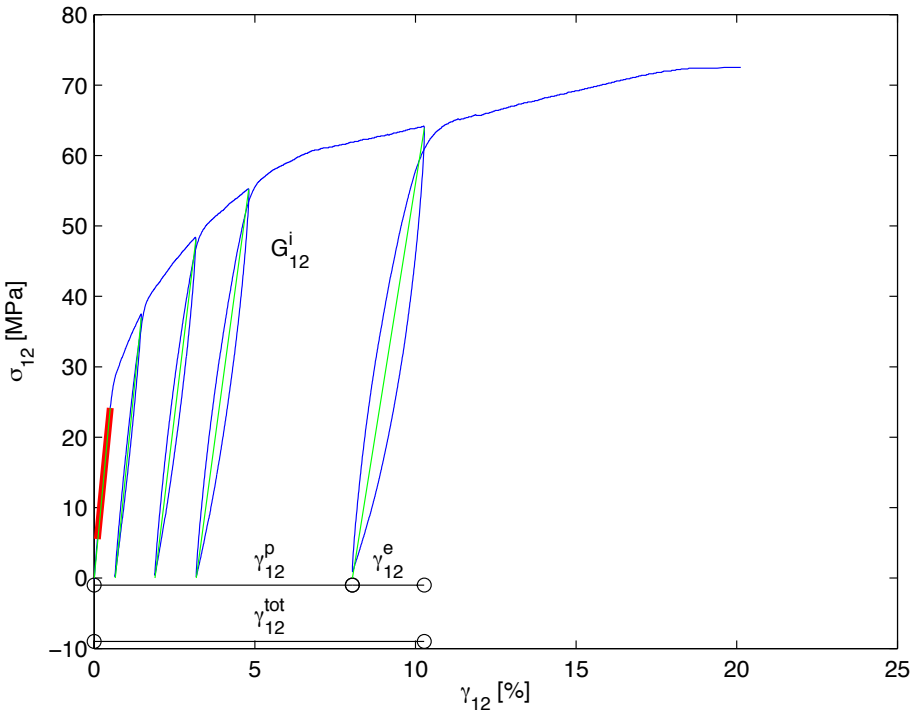

Figure 4.18: Elastic and plastic deformations, last cycle, coupon 2.6

From each cycle it is possible to extract elastic strain γ_{12}^e, plastic strain, γ_{12}^p, total strain γ_{12}^{tot} and the damage elastic modulus G_{12}^i, as shown in Fig.4.18. The scalar values of the damage d_{12} are calculated for every cycle, according to equation 4.34, hence

$$d_{12} = 1 - \frac{G_{12}^i}{G_{12}^0} \tag{4.34}$$

Coupon 2.6 was correlated, since it represented well an average behavior of the specimens. According to Ladevèze model, the damage growth function can be calculated at every cycle using equation 4.35.

$$Y_{12}^i = \sqrt{\frac{1}{2} G_{12}^0 ((\gamma_{12}^e)^i)^2} \tag{4.35}$$

The first cycle was not considered, because all the coupon of this batch exhibited a singular behavior (i.e. the slope of the first cycle is higher than the slope of the following cycles), probably caused by some sliding effects in the test fixture. Results are reported in Tab.4.5

Table 4.5: Shear non linear behavior: parameter identification

Cycle	G_{12}^{i} [GPa]	d_{12} [-]	γ_{12}^{e} [%]	Y_{12} [-]
0	4.2000	0	0.5000	0.0075
1	3.9539	0.2113	0.8137	0.0176
2	3.2917	0.3434	1.2627	0.0272
3	2.9228	0.4170	1.6333	0.0347
4	2.4858	0.5041	2.2353	0.0477

A linear function, whose coefficients are requested by the software, can be obtained interpolating different ranges of data as it can be seen in Fig. 4.19. However, these functions could not fit properly the recorded data: the linear interpolation underestimated the damage governing functions at high levels of damage, breaking the numerical coupons too late, while the exponential curve could not fit the first part of the data.
Therefore these calculated point (d_{12},Y_{12}) were given as input for an auxiliary curve in the PLY card, instead of Y_C, Y_0, Y_R.

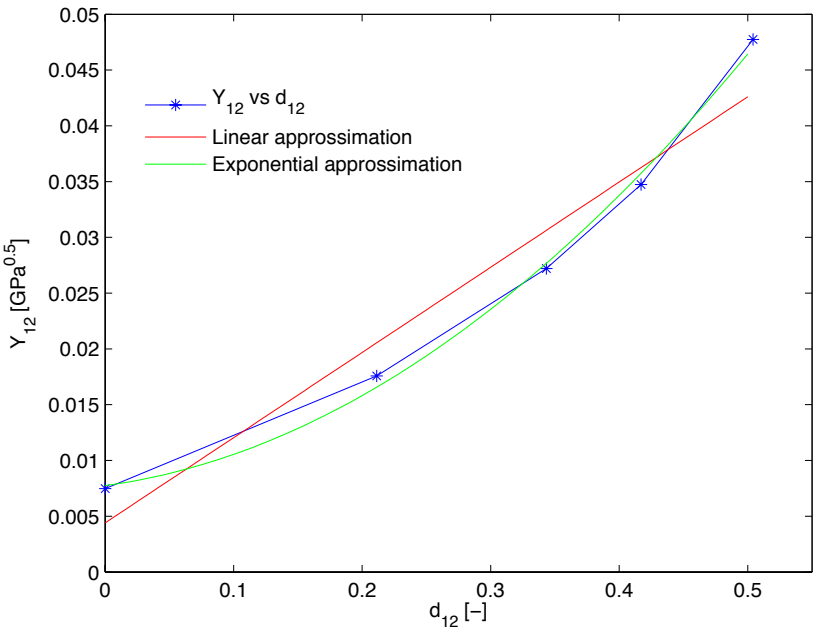

Figure 4.19: Interpolation damage governing function

4.7.2 Plastic damaging law

Non-elastic deformations are described in PAM CRASH by an exponential plasticity law (see Eq. 4.39), where β and m are material parameters, that have to be calibrated and given as input in the ply card.
The original formulation allows to couple transverse strains, ε_{22}, and shear strains γ_{12}, while the factor a, already described in the previous section, is left at 0.
The factor P_j represents the effective plastic strain and the term R_i is used to determine how the value of the shear damage d_{12} affects the yield stress at each cycle. The term P_j is calculated with equations 4.36 and 4.37, using a simple integration to include the effect of the cumulative damage. This is well explained in Fig. 4.20.

$$p_i = \int_{\gamma_{12}^{p,i}}^{\gamma_{12}^{p,i-1}} (1 - d_i)\gamma_{12}^{p,i} \tag{4.36}$$

$$P_j = \sum_{i=1}^{i=j} p_i \tag{4.37}$$

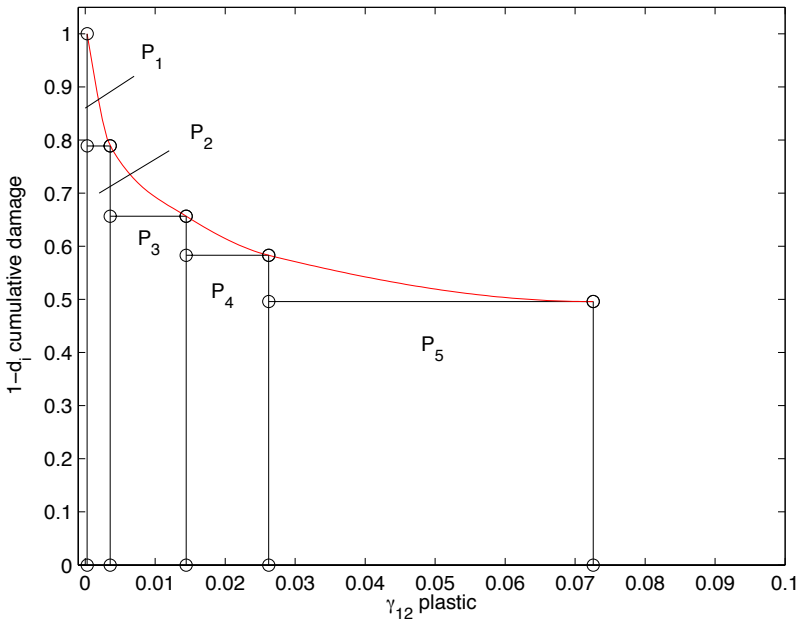

Figure 4.20: Shear calibration $[\pm 45]_{2S}$: cumulative damage

Each load/unload cycles gives an 'initial' yield stress σ_{12}^i, and a plastic strain γ_{12}^i. R_0 is the matrix shear initial yield stress. This was chosen as the stress corresponding at the first unloading point. The effective plastic strain can be calculated as:

$$R_i = \frac{\sigma_{12}^i}{(1 - d_i)} - R_0 \tag{4.38}$$

Finally, β and m are calculated interpolating the R_i and P_j data through a curve fitting exercise.

$$R_i = \beta P_j^m + R_0 \tag{4.39}$$

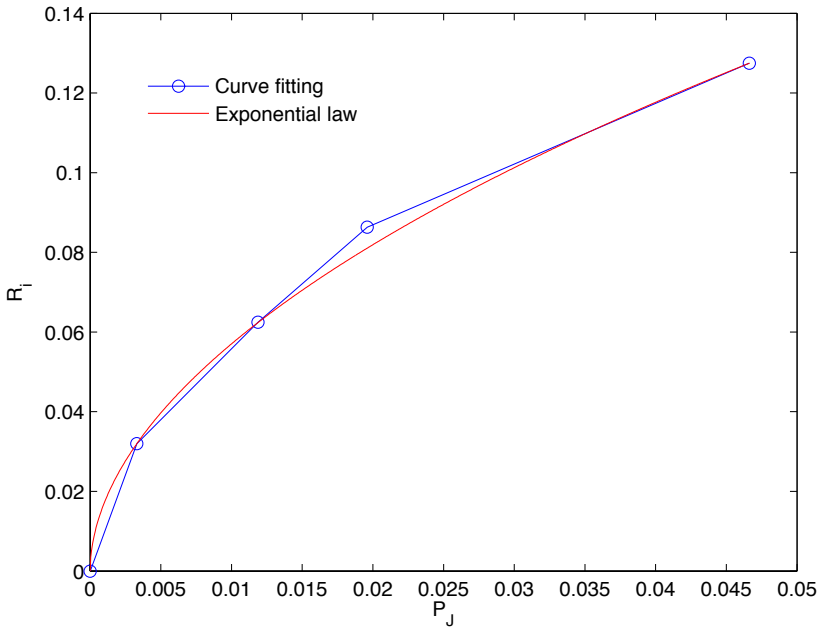

Figure 4.21: Shear calibration $[\pm 45]_{2S}$: plasticity exponential curve

In table 4.6 the data resulting from the calibration are summarized.

Table 4.6: Plasticity cumulative damage and plastic deformation at every cycle

Cycle	1-d_i	γ_{12}^p [%]	p_i	P_j	R_i [MPa]
0	1.0000	0.0276	0.0000	0.0000	0.0000
1	0.7887	0.3582	0.0033	0.0033	0.0320
2	0.6566	1.4442	0.0086	0.0119	0.0625
3	0.5830	2.6216	0.0077	0.0196	0.0863
4	0.4959	7.2587	0.0270	0.0466	0.1275

4.7.3 Specimen numerical model

The process explained above for the calibration of shear damage properties has to be considered only a first step. Even though all the passages above have a physical background, the calibration of the single element modeled in PAM CRASH does not represent the real mechanical response of the coupon. Two factors affect the quality of the calibration. Firstly, the cross area approximation: it is well known that during a tensile test the cross section area decreases due to the positive Poisson's coefficient.
Therefore performing a stress calibration in a single element, represented by the red curve in Fig. 4.25, results in a higher ultimate force value than the one recorded in the test data, Fig. 4.26. As it's highly undesiderable to try to reproduce the exact cross area variation, and considering that these parameters can strongly affect the quality of the final bearing model, it was decided to build a specimen numerical model and to perform a manual fitting of the experimental curve.
The numerical model in Fig. 4.22, is constrained at the right end in all directions, representing the real test fixture, and only in y-direction at the left end. This simple model has the same dimensions of the coupon 2.6, used to calibrate the damage parameters.
The second factor that influences the difference between these two curves is that the tabs cause a local damaged area due to the constraints numerically imposed, which actually change the mechanical response. The real coupon is not in a pure-shear condition.
The tab prevents the cross section to tighten, in contrast to what specimens do naturally in their central section, and this generates an increasing stress. This leads to the characteristic damage field shown in Fig. 4.22.

This is also the reason why the breaking cracks don not start at the center of the specimen, but in sections closer to the tabs.

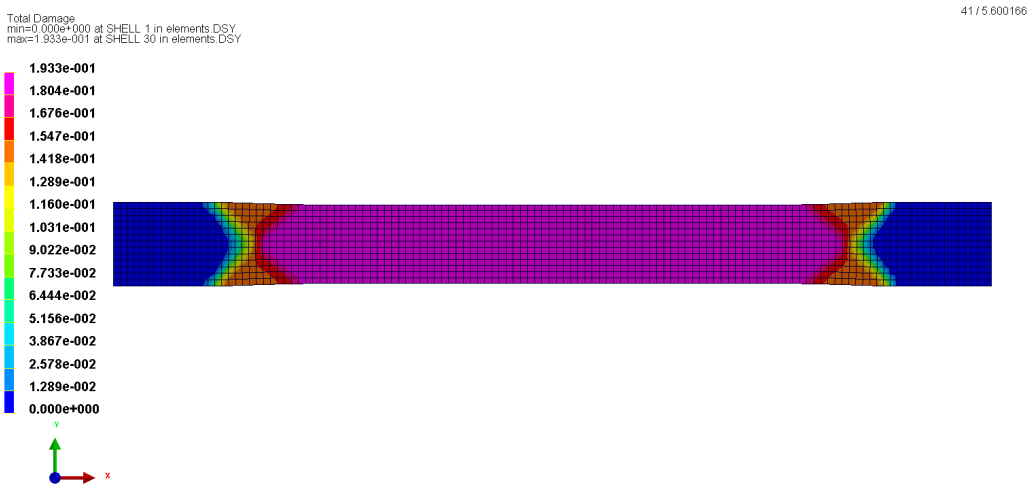

Figure 4.22: Shear calibration $[\pm 45]_{2S}$: specimen numerical model

Selecting some elements in different positions in the numerical model, as shown in Fig. 4.23, and considering their stress-strain (σ_{12})-(γ_{12}), curves, it can be seen that a local behavior characterizes the angle-ply coupon.
When a certain level of load is reached, elements in different position in the specimen reach a different state of damage. Because of this, when the force decreases as the more damaged elements approach the failure, the elements with a lower damage see the load level reduction, and consequently they unload, without breaking, as they have not still reached their limit deformation value. This is well represented in Fig. 4.24.
As the force is the same in every cross section, this local behavior can be highlighted only with a local study of the problem. This may lead to substantial differences between a single element in pure shear condition and a coupon model.

The final correlation with the specimen numerical model is shown in Fig. 4.26. The apparently bad correlation in the stress-strain diagram is caused by the two factors explained here above. These are also the reasons why in a correlation test the force and not the stress has to be calibrated.

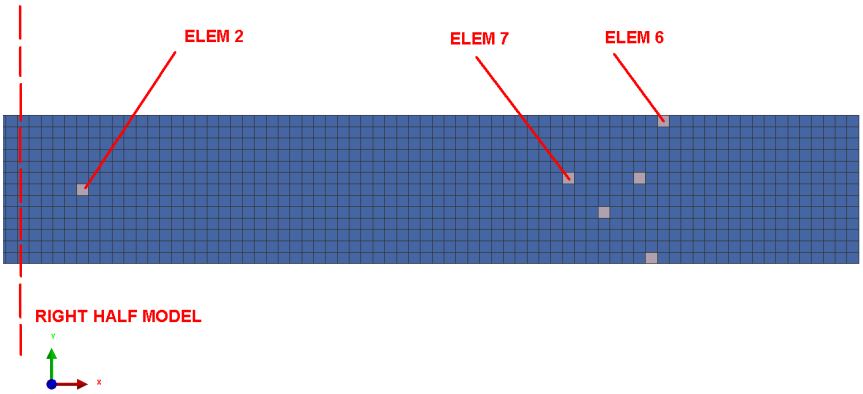

Figure 4.23: Different element positions in the numerical model

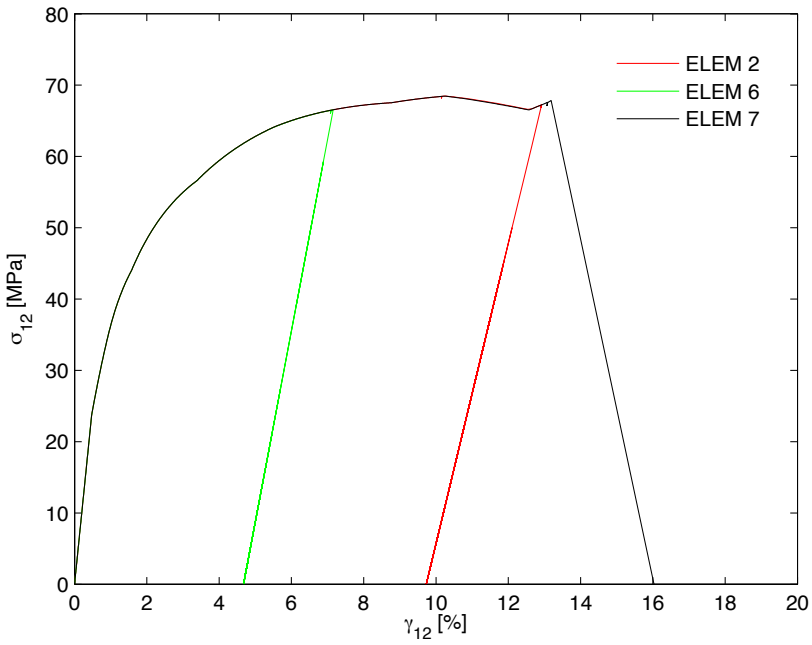

Figure 4.24: Load-unload behavior in the elements according to their position in the coupon

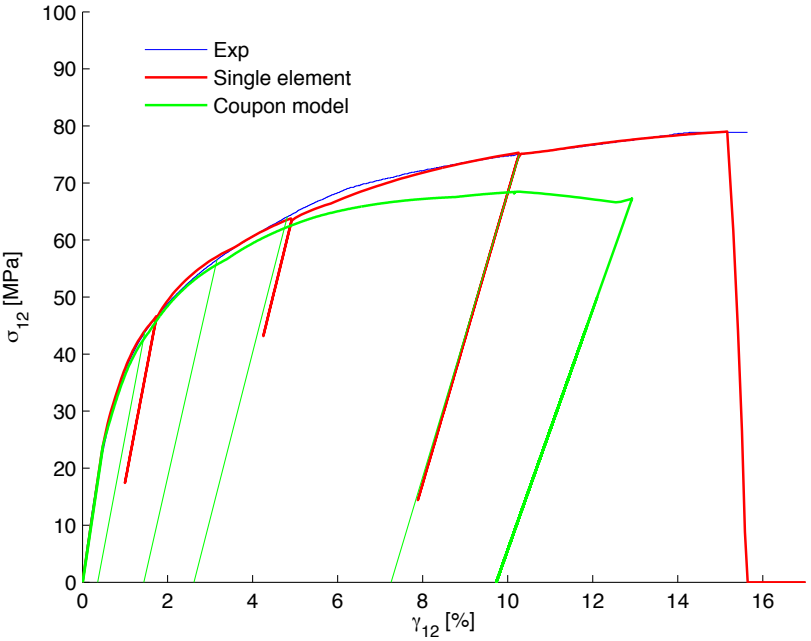

Figure 4.25: Stress calibration $[\pm 45]_{2S}$: experimental data and calibration according to Ladèveze

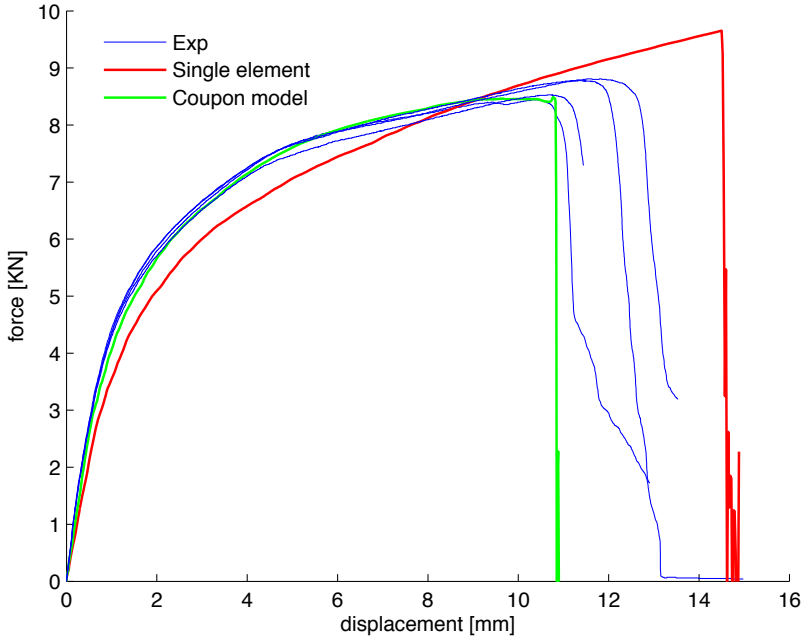

Figure 4.26: Force calibration $[\pm 45]_{2S}$: experimental data and calibration according to Ladèveze

Chapter 5

Open-hole preliminary study

5.1 Mechanics of notched specimens

5.1.1 Failure characterization within zones of stress concentrations

As a matter of fact, real industrial structural components have always different dimensions and more complex shapes in respect to simple plates or beams. These geometrical discontinuities lead to high local stress concentrations when loads are applied. This well known problem has been widely addressed in literature, considering different metal and composite materials. A similar case is reported by Matthews [31], who examined the complex influence of the stacking sequence on the failure mechanisms of bolted joints, as well as the correlation of bearing stress with specimen's width and diameter ratio, based on experimental evidence.
Moreover, the behavior of composites and metals in a notched component is completely unrelated, because of their different inelastic mechanical response. That is, when the elastic limit is reached, a metal can store additional damage taking advantage of its plastic properties and high tenacity. Composite materials, in which only the matrix allows limited plastic damage accumulation, cannot distribute stress peaks. The drilling of a plate to obtain an hole also introduces 3D border effects, which always deteriorates the mechanical behavior of a laminate [32].

5.1.2 Open-hole plate mechanics

The aim of this work is to investigate the bearing behavior of reinforced composite material, but before trying to represent a bearing test with a numerical model, it is necessary to understand how a hole can modify the mechanical

response of a generic flat laminate. For this purpose, preliminary studies were performed on open-hole specimens subjected to simple tension loading. In a generic cross section of a hole two factors can lead to stress concentration: diminished cross sectional area, and biased stress distribution.
The first factor defines that, since the cross sectional area of the holed specimen is smaller than the unnotched one, a lower force is required to reach the ultimate strength of the material, assuming a linear-elastic behavior.
The second factor is represented by a parameter, α_k that quantifies the relation between the maximum stress σ_{max} at the root of the hole and the constant ideal stress σ_{net} which comes from linear elastic fracture mechanics, as shown in Fig. 5.1.

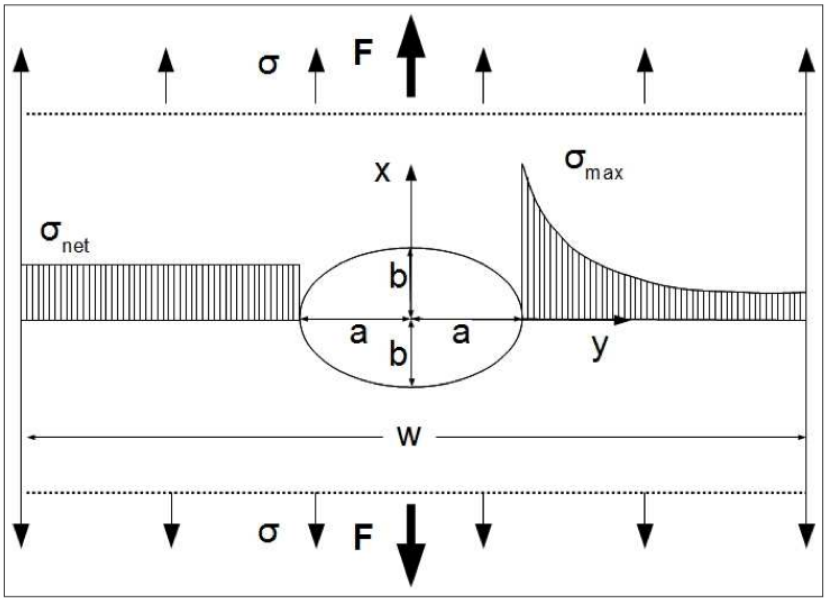

Figure 5.1: Stress distributions in an open-hole plate (adapted from [16])

This parameter, called Stress Concentration Factor (SCF), depends on several factors, like the shape of the discontinuity, the width of the plate, the surface conditions, etc. [16].
Even if, from a geometrical point of view, this parameter can be estimated from simple analytical solutions, it does not work properly for CFRP materials, whose orthotropic structure has also a significant influence on the SCF.

5.1.3 The average stress criterion by Whitney and Nuismer

An alternative approach, proposed by Whitney and Nuismer [33] and verified by Greve [24], is followed in this project. They proposed a non-local analytical criterion for failure prediction within zones of stress concentrations of elastic brittle materials. This criterion postulates that the average stress σ_0 in the zone of stress gradient, measured over a characteristic distance a_0, perpendicular to the direction of the load, equals the unnotched laminate strength.

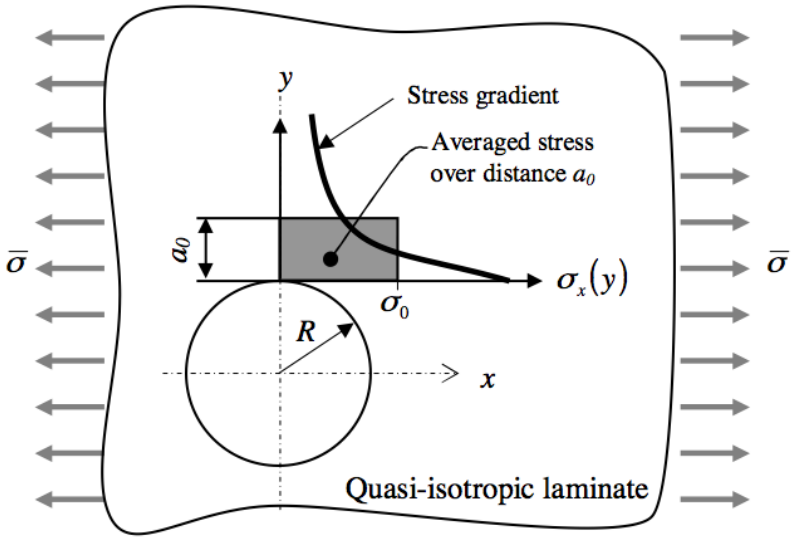

Figure 5.2: Average stress failure criterion by Whitney and Nuismer [24]

In the reference frame of Fig. 5.2, the local stress distribution in the x-direction σ_x(y) along the y-axis of an isotropic plate of infinite length subjected to uniaxial load is expressed as a function of radius R [29],

$$\sigma_x(y) = \overline{\sigma}\left[1 + \frac{1}{2}\left(\frac{R}{y}\right)^2 + \frac{3}{4}\left(\frac{R}{y}\right)^4\right] \tag{5.1}$$

where $\overline{\sigma}$ is the global laminate stress.
According to the criterion, the average strength has to be calculated within a distance of a_0 from the border of the hole.

$$\sigma_0 = \frac{1}{a_0}\int_R^{R+a_0} \sigma_x(y)dy \tag{5.2}$$

Assuming that the global stress represents the notched laminate strength ($\overline{\sigma} = \sigma_N$), and integrating, a relationship between notched and unnotched laminate strength is found.

$$\frac{\sigma_N}{\sigma_0} = \frac{2(1-\xi)}{2-\xi^2-\xi^4} \tag{5.3}$$

where D is the diameter of the hole, and ξ is defined as

$$\xi = \frac{D}{D+2a_0} \tag{5.4}$$

Therefore the notched laminate strength can be estimated from the unnotched laminate strength, the distance a_0, and the diameter of the hole.

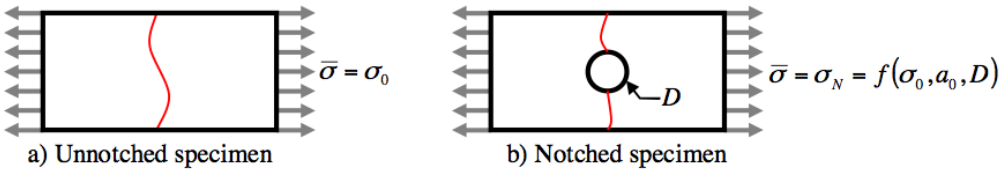

Figure 5.3: Unnotched and notched laminate strength of QI composite specimens [24]

This non-local failure criterion has been successfully applied by Greve and Pickett for the failure prediction of QI glass/epoxy laminates with different hole diameters and for QI graphite/epoxy laminates with sharp cracks of different lengths [24]. This criterion assumes that it is not necessary to have a very accurate local stresses approximation in the notch, as long as the average stress over the characteristic distance is well represented.
This phenomenon can be exploited for numerical failure prediction. The basic idea is to use a local element-wise approach, in which the failure criterion is related to a corresponding average finite element size, which is assumed to capture the average stresses and strains in the characteristic failure zone, as shown in Fig. 5.4. The average stress criterion assumes global elastic material behavior to failure and therefore it is believed to be only applicable for fibre dominated intra-laminar failure. For this reason, a laminate dominated by matrix behavior should not be correctly represented. In the next section this method is applied to two different configurations, respectively a cross-ply (CP) $[0/90]_{2S}$ and an angle-ply (AP) $[\pm 45]_{2S}$ laminate, in order to investigate the effects of the mesh size on different stacking configurations.

Table 5.1: Holed coupons test matrix

Configuration	Stacking sequence	N° of coupons
A - Cross ply (CP)	$[0/90]_{2S}$	3
B - Angle-ply (AP)	$[\pm 45]_{2S}$	3

5.2 Finite Element Analysis: notched elements mesh calibration

When it comes to Finite Element Analysis, conflicting goals arise as far as the choice of the mesh size is concerned. On one hand, it is well known that the Finite Element approach requires a fine mesh in order to represent correctly mechanical quantities (like stress and strain gradients), keeping in mind that the finer is the mesh the longer is the simulation time. Hence an extreme refinement can lead to unacceptable computational time. However, on the other hand, looking at the Fig. 5.4, it can be seen that increasing the number of elements near a zone of stress concentration can lead to inaccurate results, since the strain in a shell elements is calculated as the average of the values reached at every node, i.e. for a one integration point element it is represented at the center of the element.

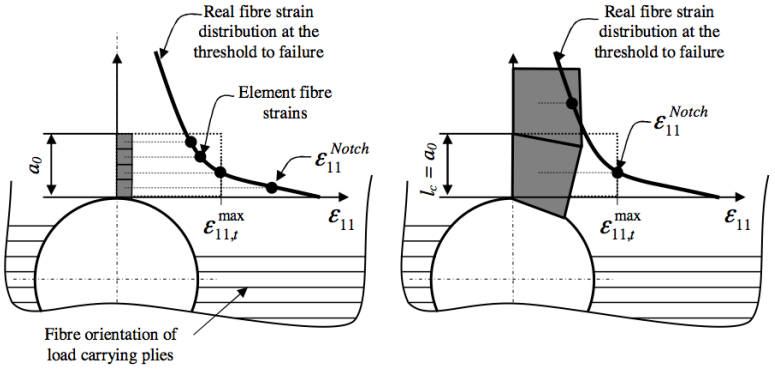

Figure 5.4: Virtual example of Finite Element models of a quasi-isotropic composite structure with a hole subjected to uniaxial tension loading in the direction of the load carrying 0° plies, using different mesh sizes for geometrical approximation [24]

Thus decreasing the elements size in problems with stress concentration would lead only to a premature failure. For this reason, a mesh calibration has to be performed in order to get the element size that best fit the load level of the experimental tests.

5.2.1 Experimental tests

The experimental tests were carried out according to ASTM D 3039 [30] standards. These norms were followed even if they refer to the unnotched specimens, like the ones tested for the calibration of the tensile properties in chapter 3, which were used for comparison. Cross-ply and angle-ply laminates were obtained from a single plate, according to Fig. 3.9. Specimens were subjected to quasi-static tension loading to failure at 2 mm/min. The longitudinal displacement was recorded by the testing machine, at the upper load cell. The holes had 6 mm diameter width and the same width of the specimens tested for bearing.

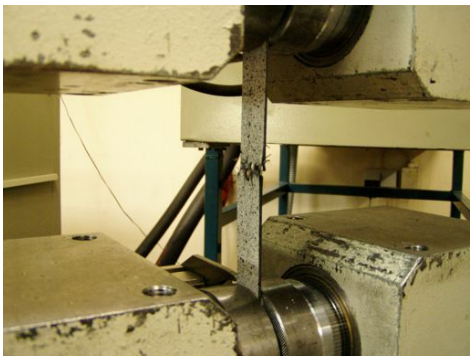

Figure 5.5: Cross-ply test

Figure 5.6: Angle-ply test

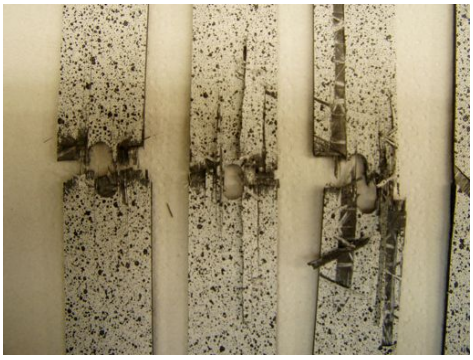

Figure 5.7: Cross-ply rupture

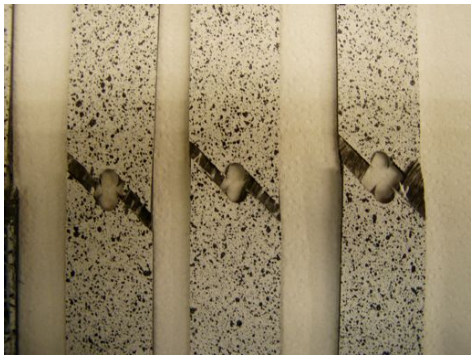

Figure 5.8: Angle-ply rupture

Figure 5.9: Open-hole experimental tests

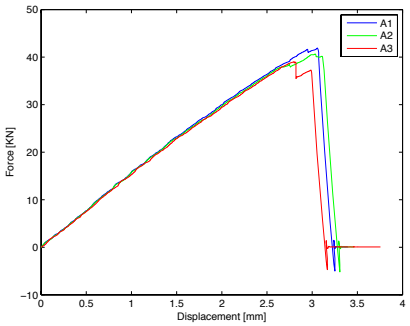

Figure 5.10: Cross-ply numerical results

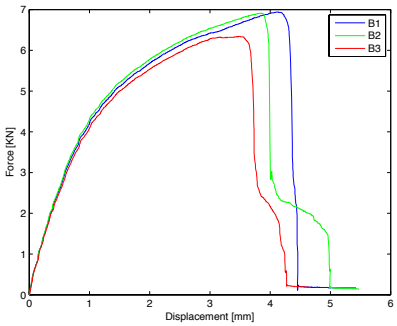

Figure 5.11: Angle-ply numerical results

The cross-ply specimens exhibited brittle elastic failure and little scatter. All three specimens broke at the hole section, as expected. Cracks starts at the border of the hole and propagate in the transverse direction. Angle-ply specimens exhibit a strong non linear stress-strain relationship, as already seen for the shear calibration in Chapter 3, due to extensive matrix deformation, Fig. 5.22. Furthermore, the failure strains for the B specimens exhibited larger scatter. This is probably related to the position of the tows around the hole. If the failure initiates in a resin rich zone, as shown in Fig. 5.12, a low maximum strain will be achieved, because of the lower local matrix strength.

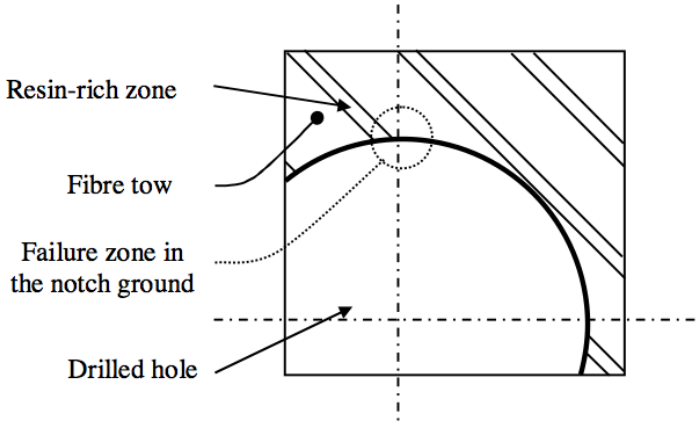

Figure 5.12: Close-up view of biaxial specimen with drilled hole showing the possible influence of actual tow position in relation to the drilled hole on the failure behaviour [24]

5.2.2 Numerical model

The experimental results were then compared with finite element models. These were represented by simple holed rectangular flat surfaces, modeled with the material data elaborated in chapter 4. The models were fully constrained at one end and only in the transverse direction at the other end, representing the tabs clamped zones. It was imposed a 2mm/ms velocity load, with a ramp-up to avoid possible numerical instabilities.

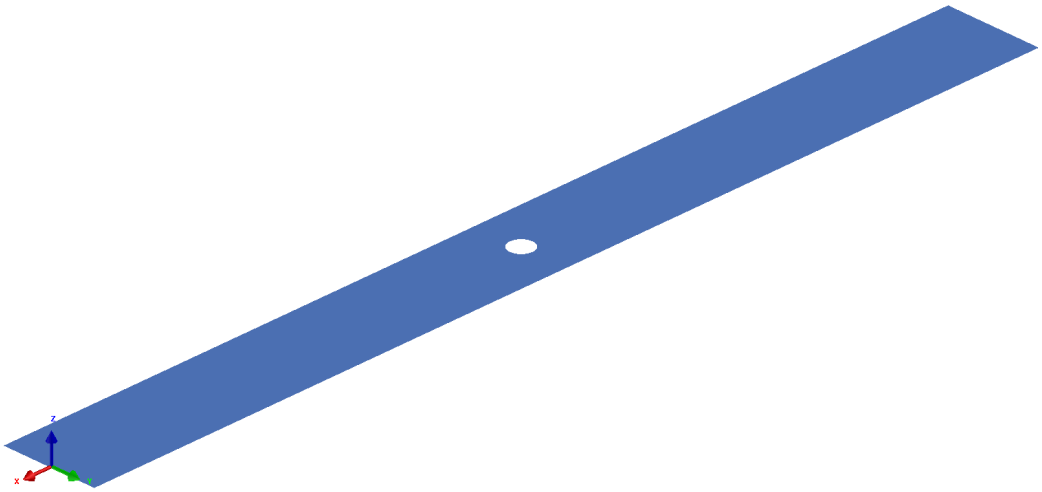

Figure 5.13: Holed flat specimen

Six different models were created in order to study the mesh dependency, varying the dimensions of the elements around the hole. Greve's results suggested an element dimension of 4mm, hence coarser and finer meshes were tried and compared.

Table 5.2: Holed coupons test matrix

Configuration	Mesh size	Element size around the hole
A	6.00 mm	4.00 mm
B	4.00 mm	4.00 mm
C	4.00 mm	3.70 mm
D	3.00 mm	2.20 mm
E	1.50 mm	1.10 mm
F	0.75 mm	0.55 mm

Configurations A and B have the same element size around the hole but different sizes in the remaining area.

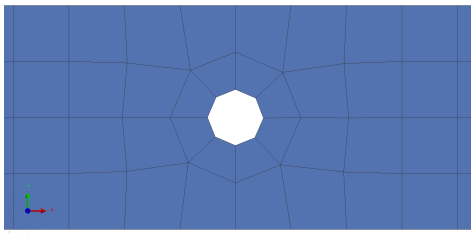

Figure 5.14: Mesh A: 4mm

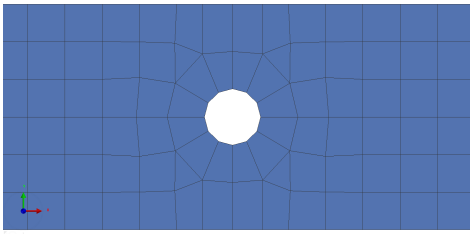

Figure 5.15: Mesh B: 4mm

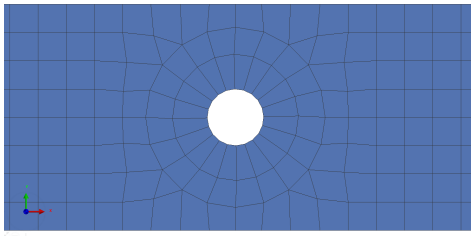

Figure 5.16: Mesh C: 3.7mm

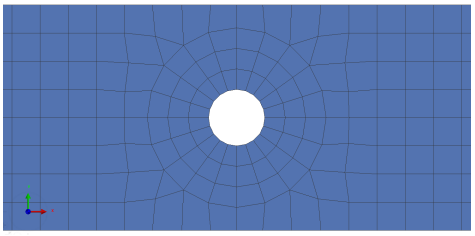

Figure 5.17: Mesh D: 2.2mm

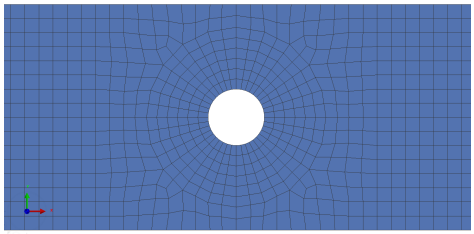

Figure 5.18: Mesh E: 1.1mm

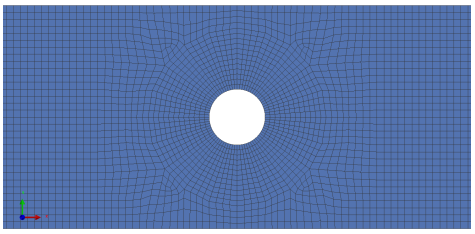

Figure 5.19: Mesh F: 0.55mm

Figure 5.20: Mesh size around hole

The simulations showed that the cross-ply configuration can be correctly represented by the 4mm element distribution, in accordance with Greve's results. A finer mesh would lead to premature failure in the laminate.
As expected, this criterion cannot be applied to predict angle-ply failure, because of the plastic behavior. Moreover, comparing Mesh A and B it can be seen that also the element size far from the hole influence the breakage value. This could be important in the prospective of an optimization analysis. The complete results are reported in the next section.

5.2.3 Comparison between experimental and numerical models

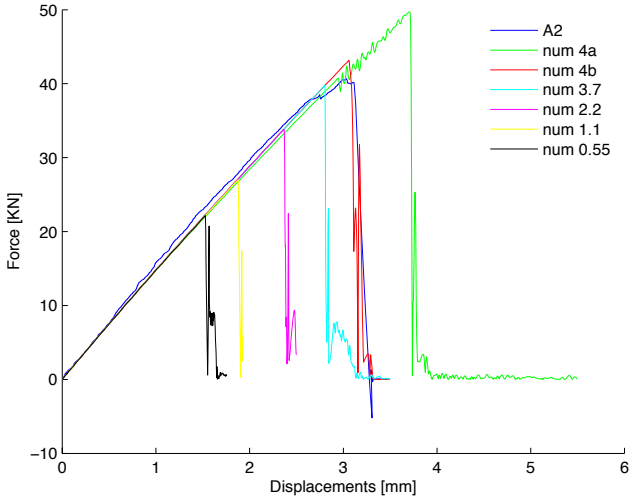

Figure 5.21: Longitudinal force-displacement curves of $[0/90]_{2S}$ specimens with a 6 mm hole subjected to uniaxial tension loading: comparison numerical and experimental specimens

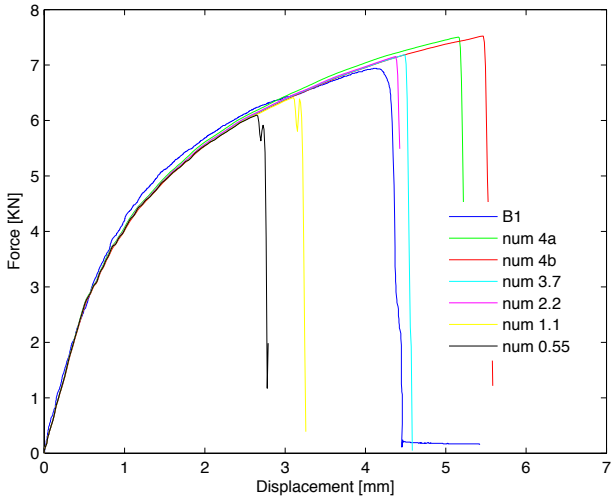

Figure 5.22: Longitudinal force-displacement curves of $[\pm 45]_{2S}$ specimens with a 6 mm hole subjected to uniaxial tension loading: comparison numerical and experimental specimens

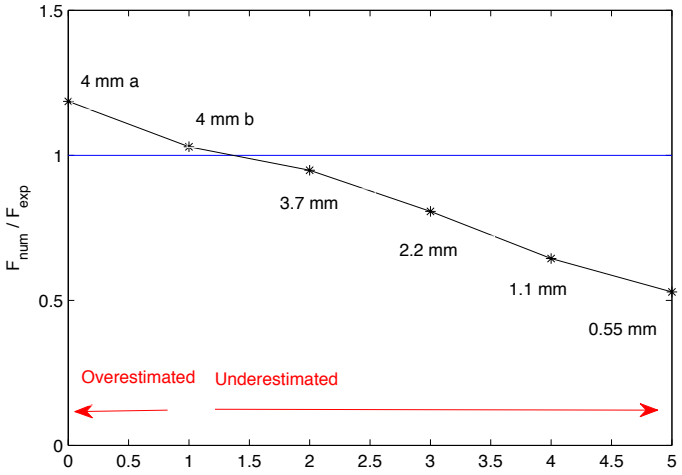

Figure 5.23: $[0/90]_{2S}$: numerical and experimental force comparison for different mesh sizes

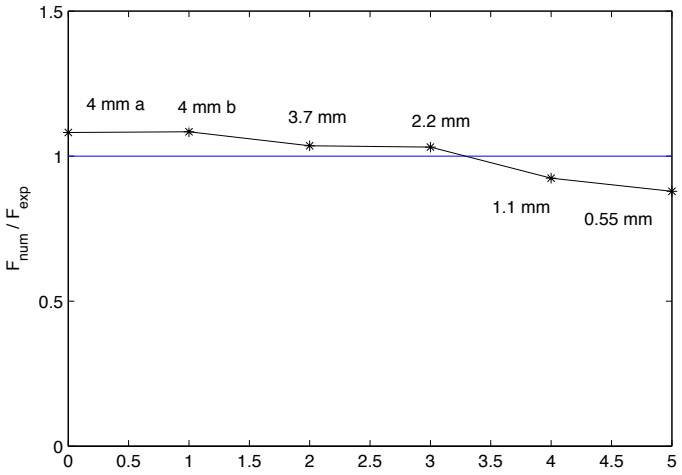

Figure 5.24: $[\pm 45]_{2S}$: numerical and experimental force comparison for different mesh sizes

The ARAMIS measuring system was used to collect and compare the deformation field of experimental and numerical models. The initial measuring volume is shown in Fig. 5.25.

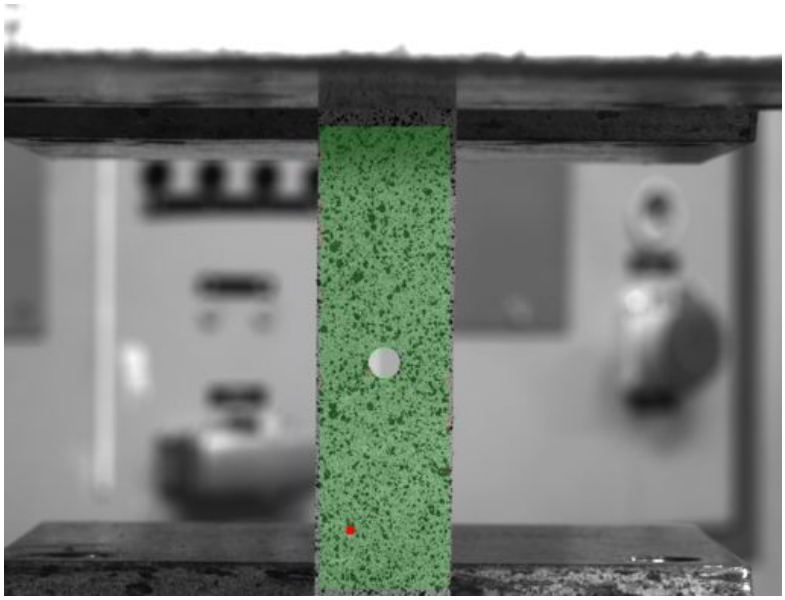

Figure 5.25: ARAMIS measuring volume

The ε_{11} deformation field of a cross-ply coupon can be observed in Fig. 5.26. The stress concentration zones are easily recognizable at the sides of the hole. The deformation field (with the same limit scale values) of the cross-ply numerical model, presented in Fig. 5.27, shows a good global correspondence in terms of strain distribution and limit values.

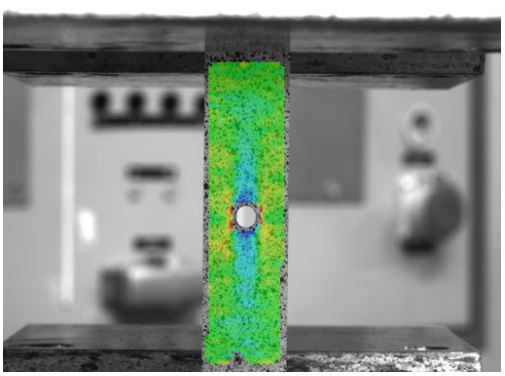

Figure 5.26: Cross-ply: ARAMIS ε_{11} strain distribution

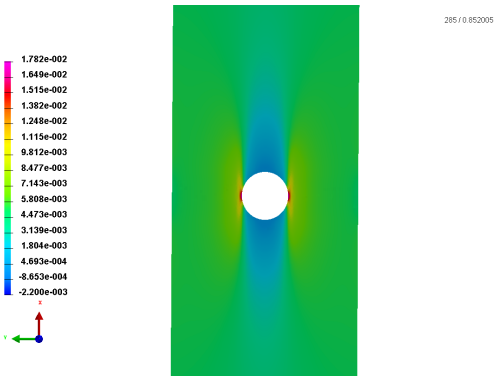

Figure 5.27: Cross-ply: numerical ε_{11} strain distribution

For the same configuration, the ε_{12} experimental and numerical deformation fields are reported below (Fig. 5.28 and 5.29).

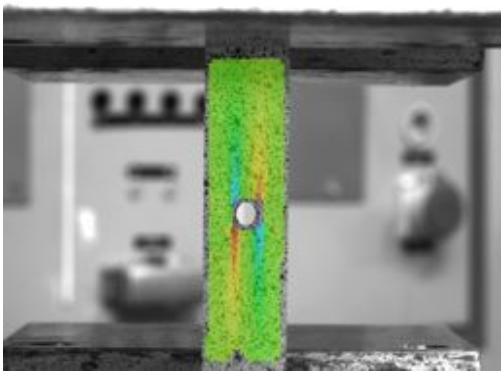

Figure 5.28: Cross-ply: ARAMIS ε_{12} strain distribution

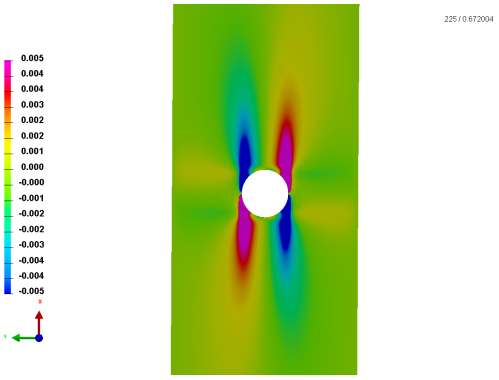

Figure 5.29: Cross-ply: numerical ε_{12} strain distribution

The ε_{11} deformation field of an angle-ply coupon can be observed in Fig. 5.30, and compared with the numerical model, shown in Fig. 5.31. The sign of the values depends on the frame of reference used by the ARAMIS measuring system.

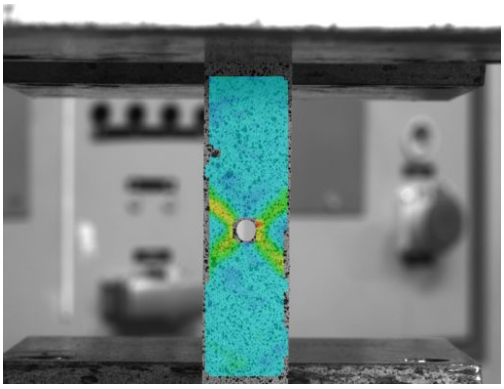

Figure 5.30: Angle-ply: ARAMIS ε_{11} strain distribution

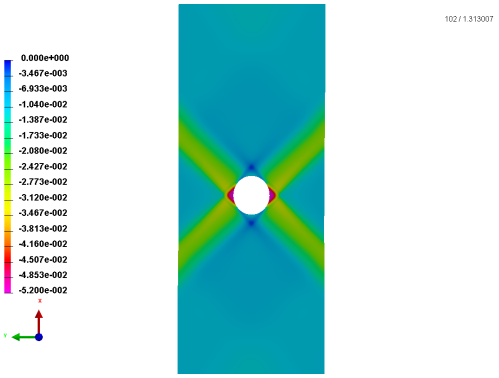

Figure 5.31: Angle-ply: numerical ε_{11} strain distribution

Chapter 6

Bearing experimental tests

This section will focus on the evaluation of the results of the bearing tests. A discussion of the test set up is necessary to understand the influence that test fixtures can have when bearing failure is originated. Comparing non-reinforced and TFP-reinforced coupons with two different configurations of reinforcement, it will be highlighted how the patches allow the samples to bear a higher load, and how the bearing strength decreases due to the local thickness increase. The failure modes observed at the end of the tests in all the configurations are then presented.

6.1 Test report

All the tests were carried out at the Institut für Flugzeugbau of the University of Stuttgart according to standard ASTM-D-5961-08 [34]. These norms allow to compare the results obtained with other tests, following a standard test method for the bearing response of polymer matrix composite materials.
The aim of a bearing test is to characterize the following properties:

- Bearing stress-strain curve.
- E^{br}: Bearing chord stiffness of the composite laminate-fastener joint.
- F^{bru}: Ultimate bearing strength of the laminate-fastener joint.
- F^{bro}: Offset bearing strength of the composite laminate-fastener joint.

Observing the tested coupons is also possible to analyze how the damage and failure mechanisms occurred.

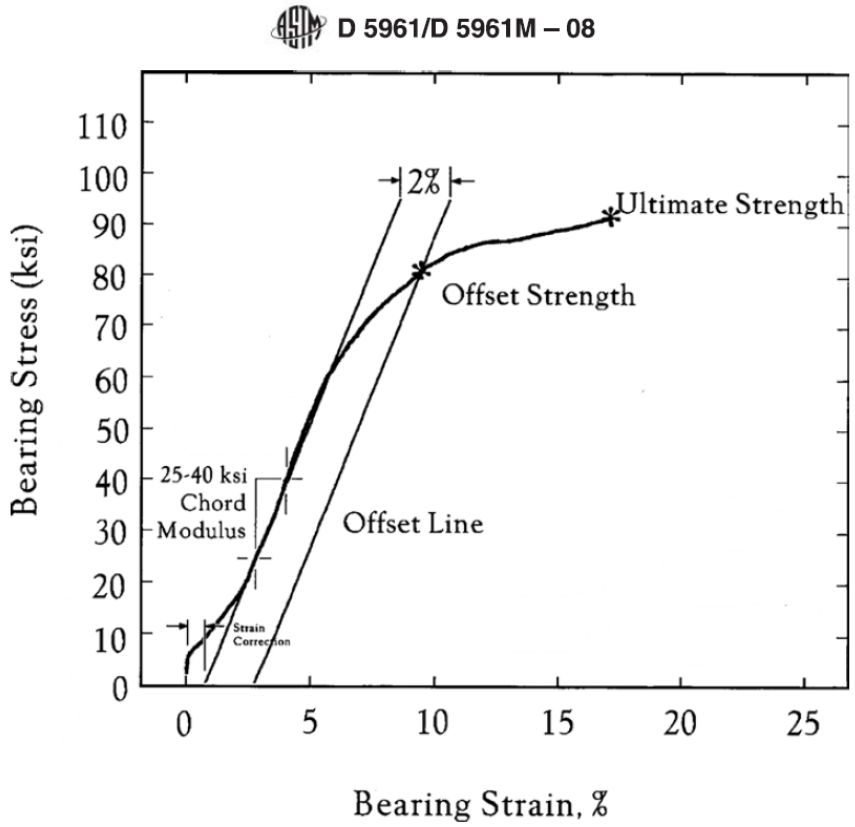

Figure 6.1: Example of bearing stress/strain curve, [34]

6.1.1 Bearing stress-strain curve

The bearing strain time history, ε^{br}, represents the deformation of the the hole in the direction of the applied force at every sampling instant, s_{Li}, divided by the diameter of the hole, D.

$$\varepsilon_i^{br} = \frac{s_{Li}}{D} \tag{6.1}$$

The bearing stress, σ^{br} is given by the force measured during the test, P_i, divided by the bearing area, which is obtained by multiplying the diameter of the hole by the thickness of the hole cross section of the tested specimens, h.

$$\sigma_i^{br} = \frac{P_i}{A^{br}} = \frac{P_i}{D \cdot h} \tag{6.2}$$

According to Fig. 6.1, the load time history has to be corrected and reworked properly. As the clamps grab the coupons, an initial compressive force is read by the acquisition system. This cause a non linear behavior in the first part of the curve, that has to be corrected for the new real origin.

6.1.2 Bearing chord stiffness

The chord stiffness represents the linear portion of the stress-strain curve. Even if the standards suggest an interval between 175 and 275 MPa, (25 and 40 ksi), in this range some coupons showed a substantial difference from the linear behavior, so a more suitable interval was chosen, using respectively 100 and 200 MPa as lower and upper limits.

6.1.3 Ultimate bearing strength

The identification of the ultimate bearing strength is not as easy as in a classic tensile test. According to the standards, this is the stress at the maximum load that can be reached. However, due to the complexity of the test, the coupons start to bend way before the maximum peak is registered by the acquisition system. Oscillations in the load curves after the offset bearing strength are noticed, which represents delaminations and, in the case of TFP reinforced coupons, detachment of the rovings.
The bolt used to join specimen and test fixture also deforms itself. According to the standards and considering that the maximum load occurred at a low level of deformations, the global maximum peak registered was considered as the ultimate bearing strength.

6.1.4 Width to diameter ratio and edge distance ratio

These parameters allow to compare tests on coupons with different configurations and dimensions. For this test, the width to diameter ratio of the specimen is $w/D = 6.0$, while the edge distance ratio is $e/D = 2.5$. These values are chosen to promote bearing failure, instead of others failure modes, as already shown in Chapter 1, Fig. 2.2.

6.1.5 Offset bearing strength

After correcting the load time history for the new effective origin, the offset bearing strength is obtained translating the chord stiffness along the strain axis of the 2% strain, and calculating the point at the interception of the two curves (dotted and blue line in Fig. 6.2).

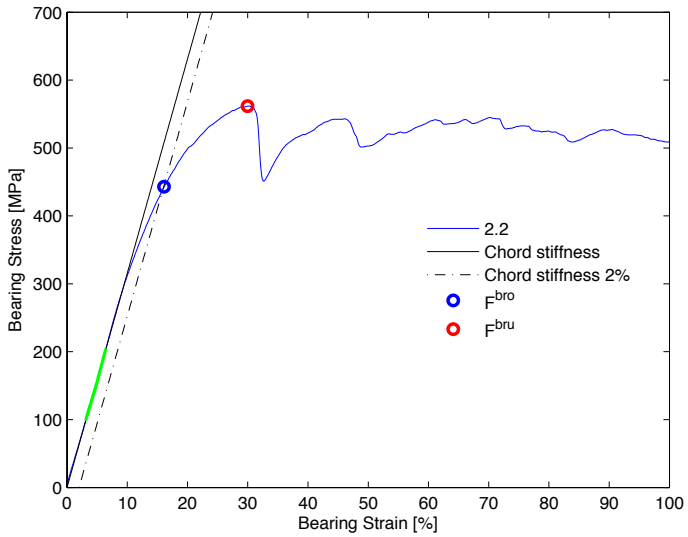

Figure 6.2: Example of bearing stress/strain curve, coupon 2.2

6.2 Test matrix

Three different configurations are compared in this project. The first configuration corresponds to a basic laminate without patch reinforcements whose data were collected by test carried out by Urbanek [5]. Configurations 2 and 3 present patch reinforcements with 3 and 5 rovings-per-arm. The basic laminate has a quasi-isotropic (QI) stacking, asymmetric in the middle:

[45/0/-45/90/45/0/90/-45/90/-45/0/45]

Table 6.1: Coupon configurations

Conf.	Basic laminate	TFP	Number of specimen
1	QI	-	5
2	QI	3 rovings per arm	7
3	QI	5 rovings per arm	7

6.3 Test procedure

A flat specimen with a rectangular cross-section is loaded in bearing at the centerline hole located near one edge of the specimen, as shown in Fig. 6.3.

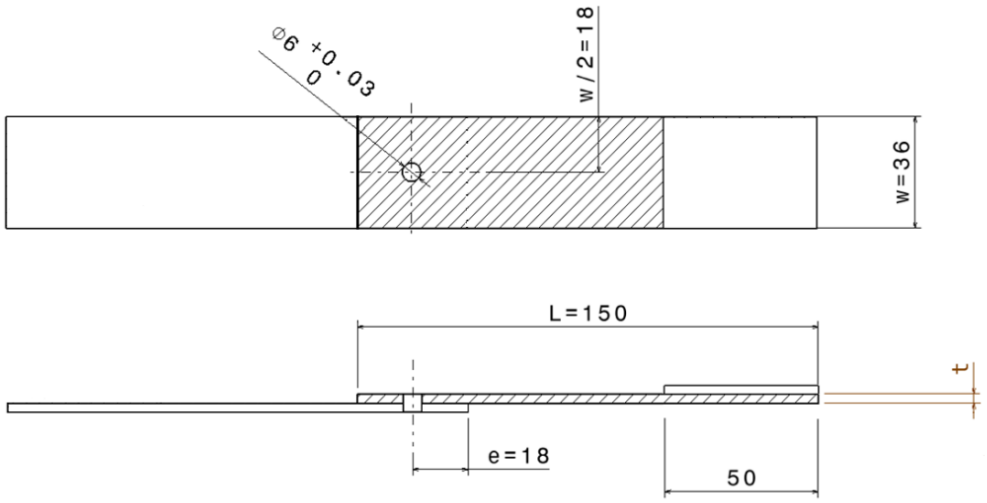

Figure 6.3: Dimensions of the coupons according to standards ASTM [5]: upper and side view

Four procedures are described in the standards to correctly promote the bearing failure. The tests carried out in this work follows procedure C [34]: single-shear tensile loading of a one-piece specimen. Because of the complexity of this failure behavior, a meaningful comparison between different configurations is possible only if these ones are tested using the same procedure and identical test parameters. This is the reason why the tests were carried out according to the same test assembly and dimensions adopted for the previous investigations of CERFAC project [5].
The bearing force is created by loading the test fixture in tension (testing machine and acquisition system have already been described in chapter 3). According to the previous tests, the hole deformation is obtained by dividing the displacement recorded in the test machine by the hole initial diameter. The effect of measuring the upper load cell displacement instead of a deformation of the hole is described in a further section.

6.3.1 Test fixture

The text fixture, shown in Fig. 6.4 consists of a steel plate connected by four fasteners and a pin to the main component, previously designed and manufactured at IFB specifically for a bearing test. This configuration allows the steel plate to be removed and replaced after every test, and also to be regulated in order to control the vertical alignment of the testing specimen, minimizing the possibility of supplementary bending.
The configuration required the upper load cell of the testing machine to be turned of 90 degrees. The test was controlled in displacement at a constant 2 mm/min loading velocity.
The configuration as it looks like just before the test starts is shown in Fig. 6.4, next to a CAD representation of the test fixture. Fasteners, washers and nuts were used to assemble the joining system. As it can be seen in Fig. 6.7, many washers were interposed between the bolt head and the plate in order to prevent the damage of the coupon contact surface.
According to the results obtained from previous tests [5], results were greatly affected by the number of washers employed and by the length of the shank of the fasteners.

Figure 6.4: Test fixture [5]

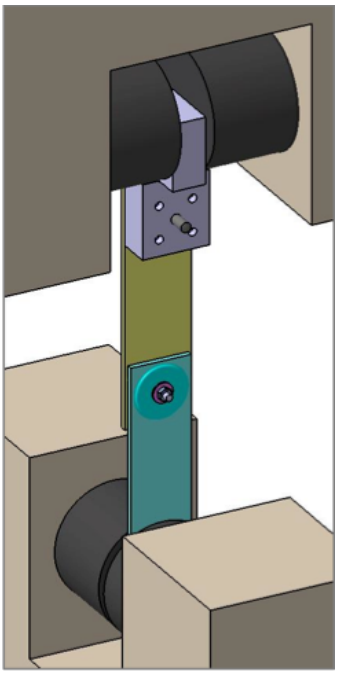

Figure 6.5: CAD drawing front side view [5]

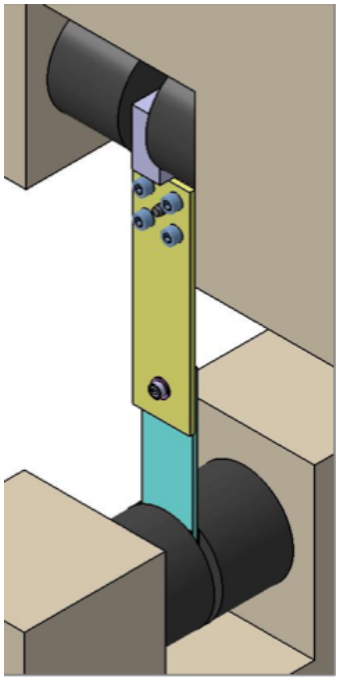

Figure 6.6: CAD drawing back side view [5]

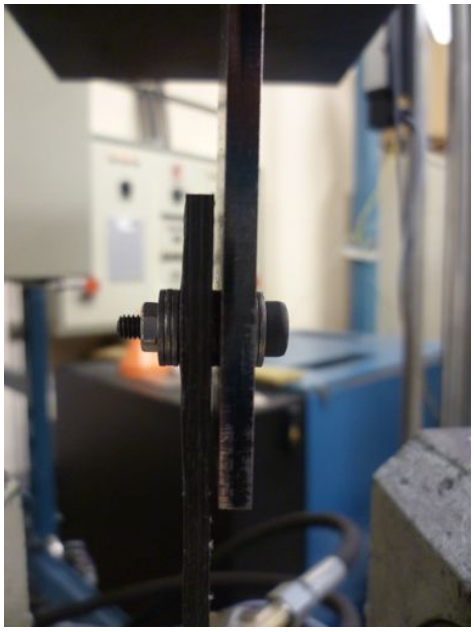

Figure 6.7: Side view of the test configuration

Figure 6.8: Front view of the test configuration

6.3.2 Discussion on the interferences in the test configuration

The bearing strain time history was obtained from the displacements of the upper load cell measured by the test machine. These includes, apart from the effective deformations of the investigated hole both in the steel plate and in the upper joints, also the effect of bending of the fasteners, and possible misalignment of the load cells. Even if this configuration was necessary for a reasonable comparison with the previous test, it is strongly recommended the usage of extensometers in the test of further TFP reinforcement configurations, as suggested in the norms.
According to the standards, the test speed has to be set in order to produce failure within 1 to 10 minutes. Tests were carried out at a head displacement rate of 2mm/min, without ramp-up and were interrupted much later than the bearing failure occurred, so that post-failure effects could be observed as well. The effect of the clamping system closing onto the tabs is everything but negligible.
A nominal torque of 2.5 Nm was imposed to the bolt. According to [35], the torque pressure has a great influence on the delamination and the ultimate bearing strength. The torque pressure suppresses the onset of delamination

and the propagation of interlaminar cracks.
The consequence is that the failure mode can change from a catastrophic one to a progressive one.
A loading eccentricity is created in every test by the offset of the line of action of force between text fixture and test specimen. This creates a moment that rotates the fastener, resulting in an asymmetrical contact stress distribution through the thickness of the specimen and between the upper and the lower surface.
From 1 to 3 washers were used trying to contrast this effect, which also strongly depends on the bolt diameter to specimen thickness ratio, the fastener torque, the size of the fastener head, the thickness and the stiffness of the specimen. In some tests the fastener yielded prior to the bearing failure of the composite sample.

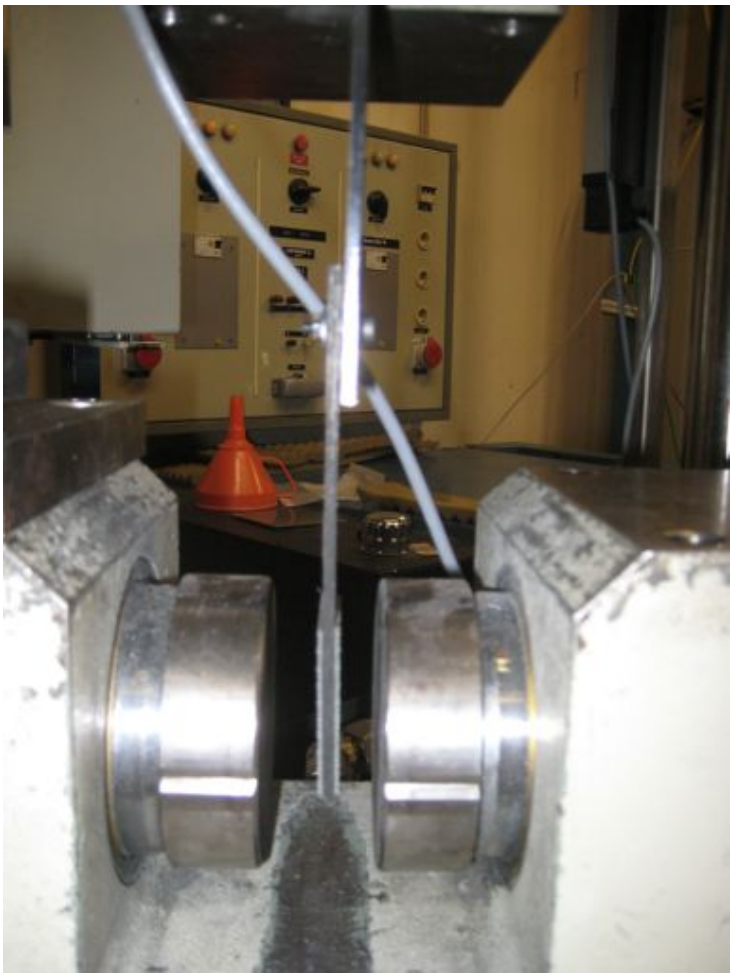

Figure 6.9: Misalignment and eccentricity caused by test configuration

6.4 Discussion of the test results

Results are reported in detail in Appendix B. In this section only the most significant issues are discussed. The bearing stress-strain curves of configuration 2, Fig. 6.10 are taken as a reference for the analysis of test data.
In every load time history coupons present an initial linear behavior, followed by a growing bending caused by the deformation of the hole.

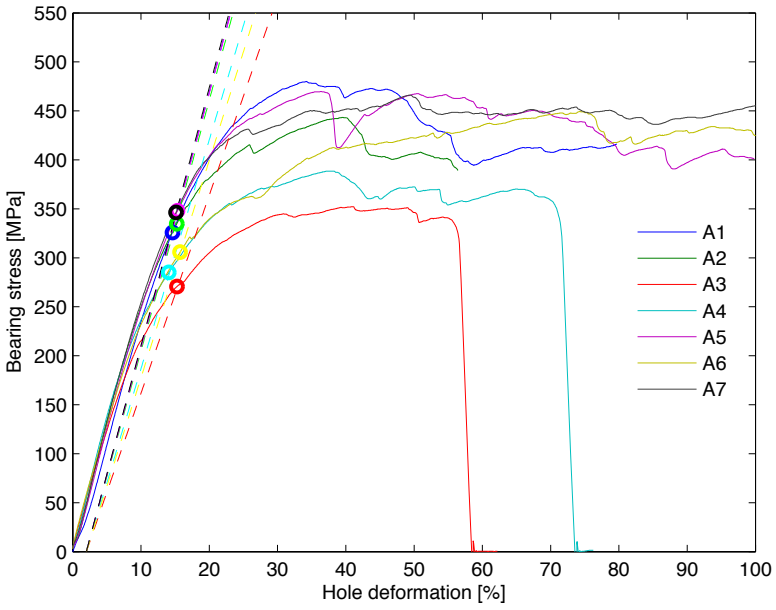

Figure 6.10: Configuration 2: Bearing stress-strain curve

It is very difficult to understand when the elastic behavior is replaced by a permanent deformation in the hole. A short fastener and only one washer per side were used for the first 6 coupons of configuration 2. In all the next tests a longer shank of the bolt and more washers per side were used. This is probably the reason why some coupons, A.2, A.3, A.6, exhibit a singular loading behavior with a significant loss in terms of offset and ultimate strength. That is, the short shank of the bolt enhance possible misalignments between the coupons and the test fixture, resulting in a premature failure. During the tests of coupons A.3 and A.4 this effect was so intensified that led to a fracture of the fastener shank. Most coupons presents an apparent first peak and just after that a rapid unload. This is considered to be a first ply failure of the laminate, as at this point of the test it could be clearly heard a typical sound of rupture.

6.4.1 Comparison of the different configurations

The first interesting comparison between the chord stiffness of the two configurations shows that the test fixture has a remarkable influence on the displacements. This has a great importance in evaluating the test results, since the bearing offset strength depends on the chord stiffness (it is defined as the intersection with the experimental curve).
The most important drawback of VARI process is here highlighted. The thickness at the hole cross section in configuration 2 and 3 is considerably higher than in the unreinforced laminate, due to the presence of the patch reinforcements. This resulted in an opposite trend for stresses and forces. Besides, it has to be pointed out that the definition of bearing strength and strain comes from standards, which were created considering laminates with constant cross sectional area. Because of the architecture of the star reinforcements, the thickness decreases as the distance from the hole increases. The variation of the bearing area during the test is really difficult to evaluate. For this reason, the force data are considered more reliable than the computed stresses and strains.
The data in the following graphs refer to average values of the first configuration, set at 1, for a more effective view of the different trend of force and stress values. In the worst case the patch thickness reaches 1.4 mm at the hole cross section, making the reinforced laminate locally 51% thicker than the ones in configuration 1.

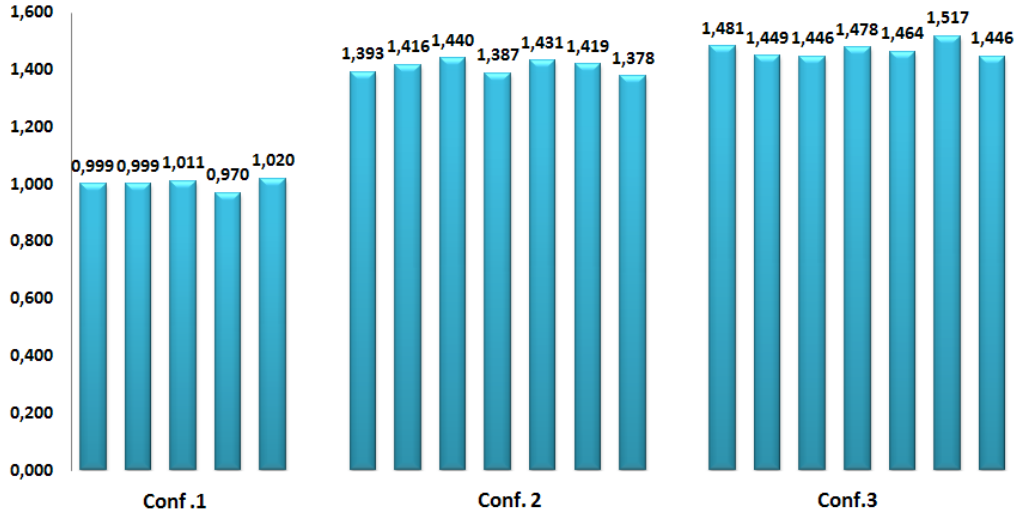

Figure 6.11: Comparison of different thickness in configurations 1, 2, 3.

Even if the two reinforced configurations have the same thickness the load carrying capacity is higher in the patches made out of 5 rovings per arm.

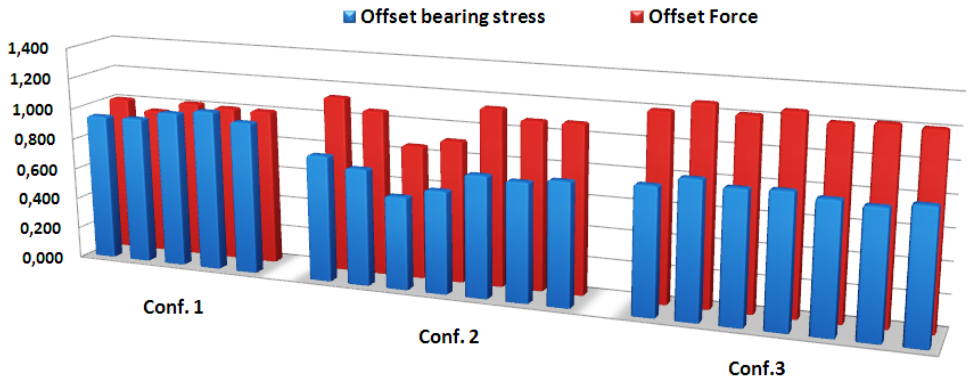

Figure 6.12: Comparison of bearing offset stresses and forces in configurations 1, 2, 3.

In general, data collected from the latest coupons exhibit less scatter than the first ones. This is probably due more to experience gained during the tests than to a better behavior of the configurations.

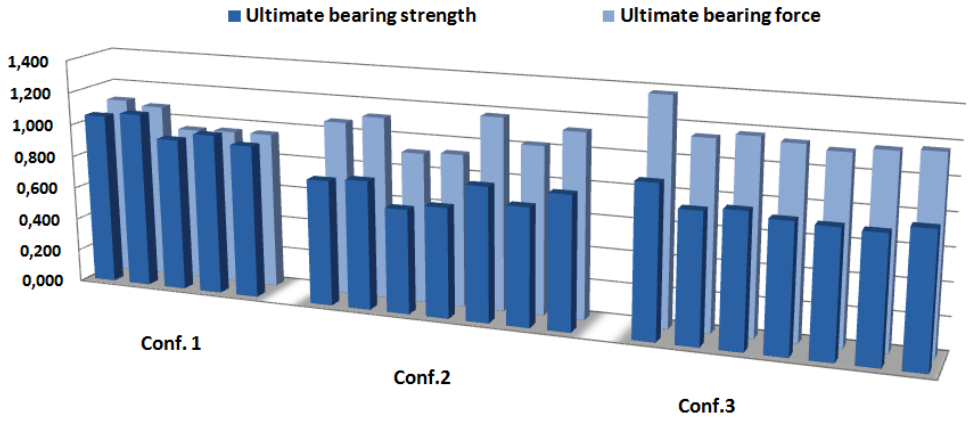

Figure 6.13: Comparison of ultimate bearing stresses and forces in configurations 1, 2, 3.

6.5 Failure

In Fig. 6.14 it is shown a coupon after the test. The bearing deformation of the hole is easily recognizable. The new deformed diameter of the hole in the loading direction was about 9 mm, that is 3 mm wider than the original hole, which means 50% deformation of the hole. From the loading time history, Fig. 6.10, at the end of the test the testing machine recorded displacements up to 8 mm. This difference clearly confirms that only the first part of the loading time history has to be considered as representative for bearing behavior.

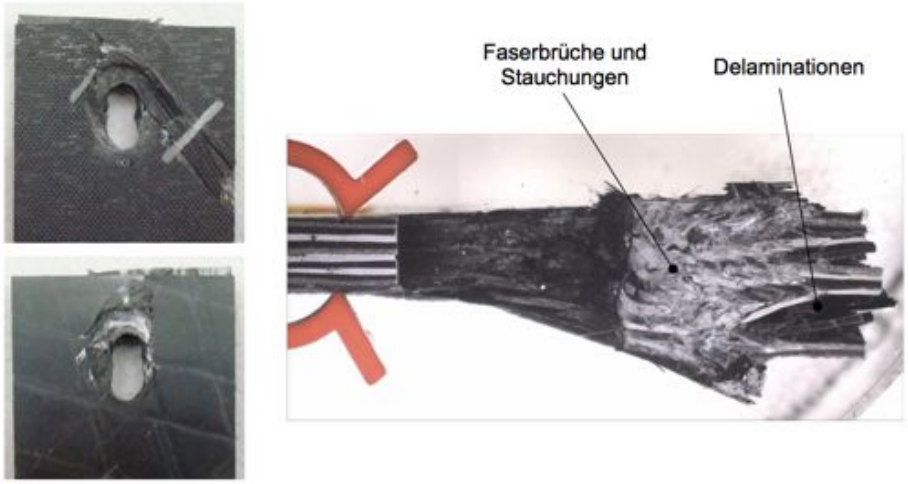

Figure 6.14: Bearing failure in QI laminate: front, back and side view, damage and failure [5]

From the side view it is possible to see the damage in the laminate after the test. Delaminations (*Delaminationen*), fiber buckling (*Stauchung*) and ruptures (*Faserbrüche*) can clearly be identified. There is a big circular area around the hole that shows the presence and the influence of the washer. These press the laminate in the out of plane direction, preventing the micro-buckling of the fibers and postponing the growth of delaminations.
As a result, coupons with a bigger number of washers exhibited generally a better behavior than the other ones. Apart from the compression stress it can be seen that also the $+45°$ orientated roving suffered a delamination, showing the great influence that shear stresses have in the damage mechanisms.
In both configuration with TFP reinforcements, it is clear that the failure takes place firstly in the patches, and then in the laminate.

6.5.1 Configuration 2: 3 rovings per arm

A few examples of failure modes are here illustrated. During the test of coupon 3, Fig. 6.15, the bolt broke interrupting the test, therefore a significant bearing deformation couldn't be achieved. Instead, all the rovings of the reinforcements failed in the test of coupon 6, Fig. 6.16. The failure of the TFP reinforced coupons occurred predominantly in the patches, as it can be seen in Fig. 6.17 and 6.18.

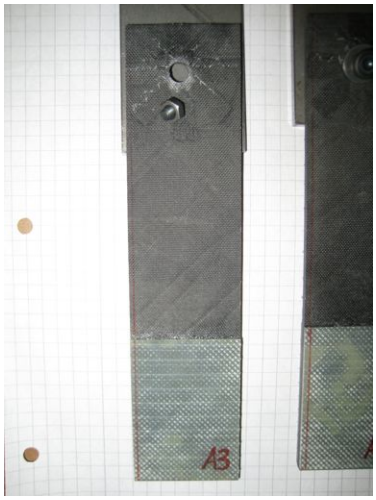

Figure 6.15: Configuration 2, coupon 3, fastener rupture

Figure 6.16: Configuration 2, coupon 6, huge delaminations

Figure 6.17: Configuration 2, coupon 7, bearing deformation

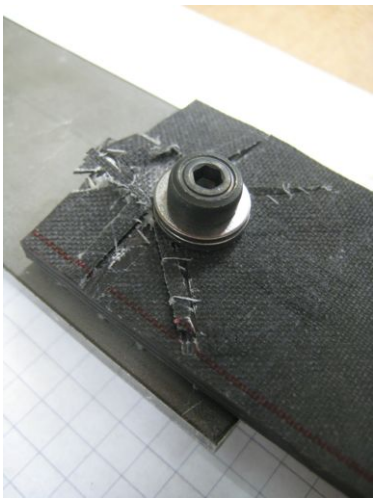

Figure 6.18: Configuration 2, reinforcement failure

6.5.2 Configuration 3: 5 rovings per arm

These patches shows a better behavior than the previous configurations. The tests shows that the first failed roving is always the one at the middle right side, as shown in Fig. 6.20. This is caused by shear and compression stresses who promoted its delaminations.

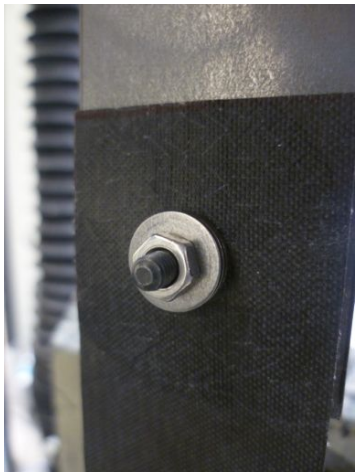

Figure 6.19: Configuration 3, front view, before testing

Figure 6.20: Configuration 3, front view, after testing

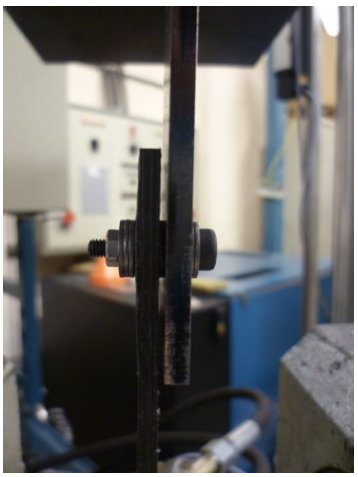

Figure 6.21: Configuration 3, side view, before testing

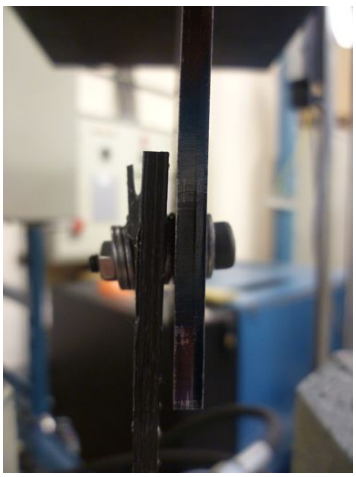

Figure 6.22: Configuration 3, side view, after testing

From the side view the bending of fastener and washers can be observed, as well as the delaminations in the upper part of the hole.

Chapter 7

Bearing finite element model

The development of a Finite Element Model can be a valid proof of the understanding of real phenomena. Once the phenomenon is correctly represented, this approach offers the possibility of studying and performing improvements, thanks to an optimization process.
In this chapter a numerical model is described in order to correlate numerical and experimental data, with the final aim of represent the bearing damage and failure behavior of composite joints. The first simulations performed with the explicit code PAM-CRASH showed that bearing failure cannot be represented with the same approach as for a standard tensile test, therefore a new research code provided by ESI-Group, and originally designed for crushing phenomena such as cylinder impact, was developed. The modeling of the entire bearing test assembly, including both test fixture and coupon model, would have led to a high computational time and still it would not guarantee a correct representation of the phenomenon, therefore some preliminary simplifications had to be made.
Representing such a complex failure mode like bearing failure with the Finite Element Method introduces additional problems, depending on the code structure, that have already been pointed out in Chapter 5. Keeping in mind what learnt from the investigation of notched specimens, particular attention was paid in the choice of the mesh size. The inter-laminar delamination failure model was developed according to the approach proposed by Johnson, Pickett and Rozycki [36], using stacked shell layers connected via delamination interface laws. In a common aeronautical design process an hole deformation exceeding 2% is considered failure, hence the correlation of this value is the primary goal of the present model.
The research code has been proven effective in modeling the bearing behavior, however some suggestions about possible improvements are discussed at the end of this chapter.

7.1 PAM CRASH Cards

7.1.1 Coupon model

The specimen is represented by a flat holed surface made of shell elements, with the same nominal dimension defined in the standards, Fig. 6.3. PAM CRASH allows to model composite laminates with different surfaces representing the different plies, so that the same quasi-isotropic stacking sequence can be introduced ply by ply. The thickness can be assigned in the material card. For every configuration, the thickness of a single ply is obtained dividing the average thickness of the configuration by the number of plies. Mechanical properties of the composite material are taken from the data collected during the calibration as explained in Chapter 4. Due to the extensive presence of delaminations occurred during the experimental tests, caused by out-of-plane stresses which are not supported in a typical shell element, another configuration comprehensive of 3 tied surfaces, each one composed by 4 plies, was investigated. Even if the computational time is drastically affected by the increase of element's number, this second approach should be able to represent delaminations and out of plane shear cracking adequately.

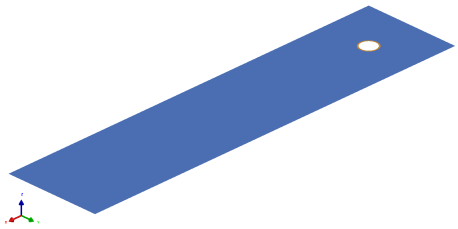

Figure 7.1: Coupon's shell elements surface: multilayered configuration

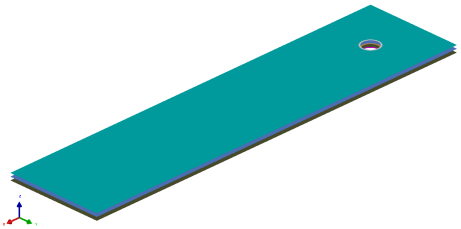

Figure 7.2: Coupon's shell elements surface: 3 tied surfaces configuration

7.1.2 Fastener model

The fastener is a critical component of the test, as it has the purpose to transfer the force from the test machine and the test fixture through direct contact with the hole surface. The complex geometry of the fastener is reduced to a simple cylinder, modeled in two different ways: firstly using solid elements, and secondly just reproducing the outer surface with shell elements. It is impossible to represent an exact circular surface with an integer number of elements, therefore an adequate number of nodes was chosen in order

to reproduce the contact pressure as uniform as possible but maintaining a reasonable time step.

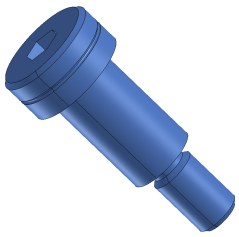

Figure 7.3: Fastener: CAD geometry

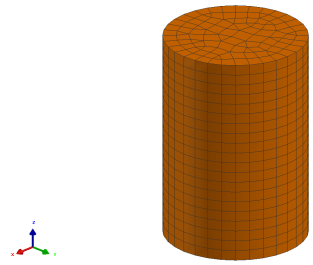

Figure 7.4: Fastener: solid elements modeling

The solid model allows to take into account out of plane stresses, but requires a higher computational time than using shell elements. The solid approach was followed to investigate how significant the deformations of the fastener are. This has been done because in a few tests the bolts showed great damages, and in two cases their failure caused the interruption of the test. The solid elements were modeled with steel material, card 1-ELASTIC-PLASTIC-SOLID where only the basic data such as an elastic modulus of 210 GPa and a Poisson coefficient of 0.3, were assigned.
However, after the first simulation neither significant damaging nor deformations occurred in the solid fastener before the first peak in the loading time history, and consequently 3D solid elements were replaced by 2D shell elements in order to save computational time. The same material data were kept but set with another card defined for rigid body constraints (see Sect. 7.1.4), 100-NULL-MATERIAL-SHELL.

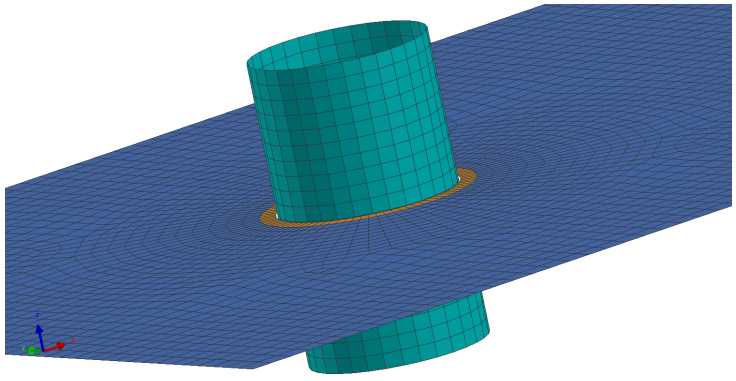

Figure 7.5: Fastener: Shell elements modeling

7.1.3 Test fixture

As already explained, the modeling of the complete test fixture is not the purpose of this project. All the interferences and flexibilities generated in the test assembly, already explained in section 6.3.2, were collected in a single bar element, whose mechanical properties and dimensions (card 202-ELASTIC-BEAM-BAR) were calibrated in order to reproduce the initial linear part of the load time history, remebering the experimental tests. Several runs of the model with different bar properties showed that the bar does not affect the final crushing stress, hence the usage of a simple element as the bar is justified. According to the damaging showed in the experimental tests, the model is considered reliable up to a bolt displacement of 3 mm.

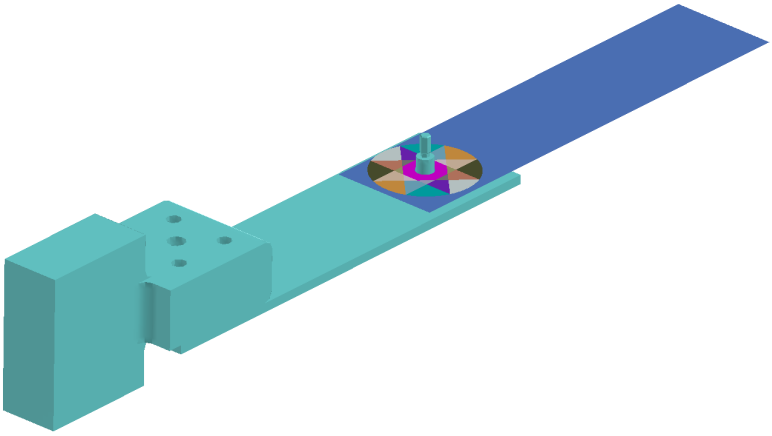

Figure 7.6: Complete test fixture model

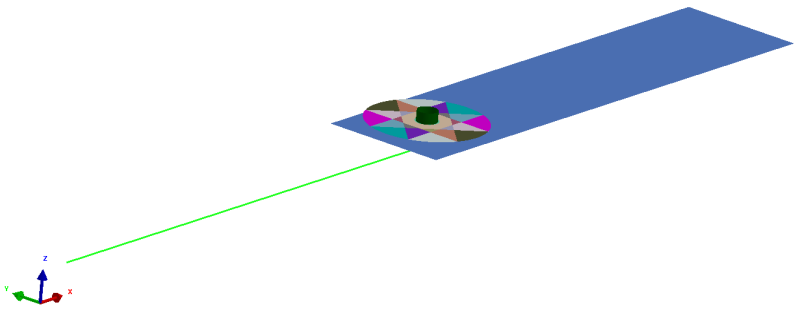

Figure 7.7: Representative bar element test fixture model

7.1.4 Loads and constraints

The numerical model was constrained according to the test configuration, as shown in Fig. 7.9. The nodes in the region of the glass tabs at the unnotched end of the coupon were fully constrained, simulating the clamping jaws. The end node of the bar was fully constrained except for the loading direction, and so was the bolt. The possibility of bending was prevented, because during the first simulations discontinuous contacts were observed, caused by the lack of damping options in the crushing code that is still in a research version. This choice was followed to avoid possible numerical instabilities, but limits the reliability of the model at high level of deformations.

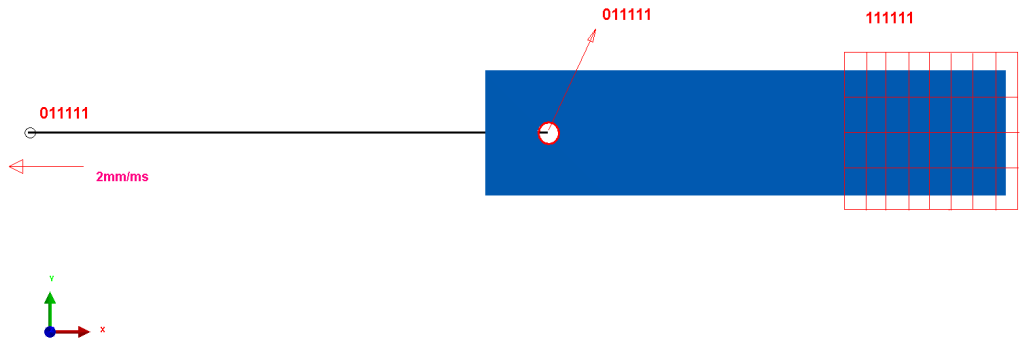

Figure 7.8: Complete test fixture model

Due to computational reasons, a 2mm/ms velocity load was imposed. However, since this value introduced significant dynamic effect on the coupons, a ramp-up was added in the velocity profile to limit oscillations of the contact curve in the first linear part of the loading phase. Even though the thickness of the shells can be increased within reasonable dimensions limit, these elements could not stand the load coming from the contact forces. The fastener was modeled as a rigid body with the card CONTACT RIGID BODY, keeping in mind that the force transmission of a rigid body is not equal to the one of an elastic body. A rigid body is an element of infinite stiffness defined on a number of nodes. Its basic degrees of freedom (DOF) consist of spatial rotations and translations. The DOF of the rigid body is fully determined by the DOF of an artificial "node" located at the rigid body's center of gravity

(COG), where all the boundary conditions have to be applied. A NODAL CONSTRAINT links its center of gravity to the first node of the bar test fixture, Fig. 7.9. This constraint ties the nodes (COG and the node of the bar) to the same 3 translational degrees of freedom. Only the displacement field is continuous between constrained nodes and the rest of the model, that is, only forces but no moments are transmitted through the constrained nodes.

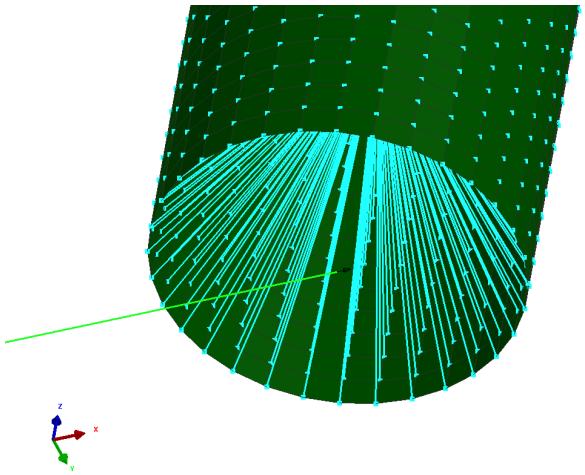

Figure 7.9: Fastener: loading constraint and Rigid body

7.1.5 Output

An explicit analysis was performed. The test fixture introduced in the test apparent differences even in chord stiffness between different configurations. The NODE TIME HISTORY of the bar node where the loading velocity was applied is recorded, trying to represent the displacement of the upper load cell. According to the crushing dataset, the force used for the correlation with the experimental data was the contact force between the fastener and the coupon.
Filtering can be the most critical phase in the processing of impact signals. The main goal of a filter is to eliminate undesired high frequency noise that can obscure the underlying signal. The corner of a low-pass Butterworth filter is defined as the frequency at which the signal magnitude attenuation is equal to 3 decibels (DB).
The load time history was filtered with a low-pass filter of the channel frequency classes (CFC) 600, whose corner frequency is derived from the Butterworth one dividing the designation by 0.6. Thus the corner frequency of CFC 600 is 1000 Hz.

7.1.6 TFP patch modelling

The patches were manufactured stitching different orientated rovings on a glass woven fabric. The reinforcements were modeled as SHELL elements, as this is the type of element required for the crushing dataset. A simple flat rectangular plate with width of 3 mm and a length of 34 mm was used to represent a single roving.

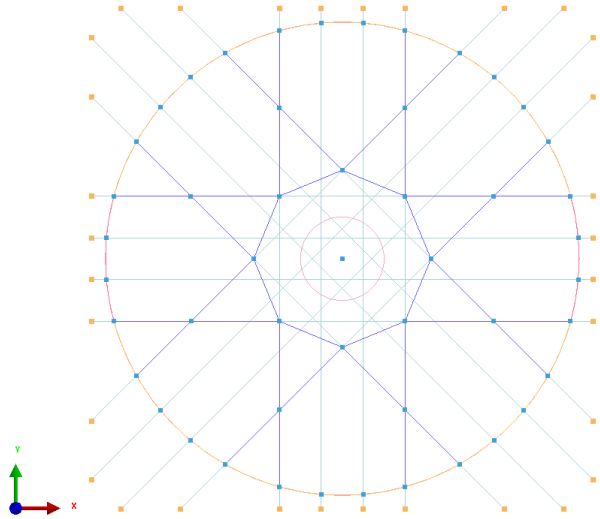

Figure 7.10: Patch geometry, example with 3 rovings per arm

Assembling 3 and 5 rovings per arm respectively for each configuration, Fig. 7.10, the meshes described in Figures 7.11 and 7.12 were obtained.

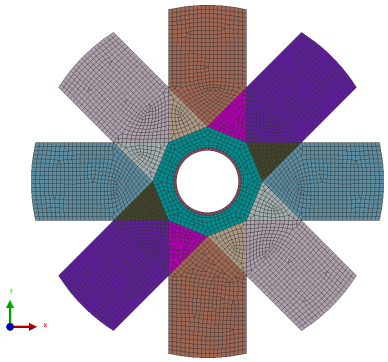

Figure 7.11: Numerical model of TFP patches 3 roving per arm

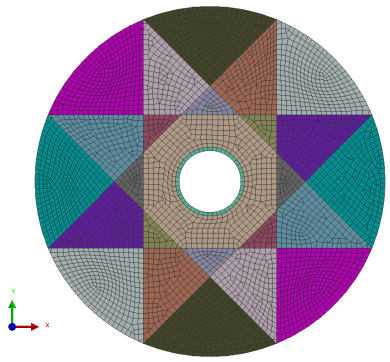

Figure 7.12: Numerical model of TFP patches 5 roving per arm

The correct thickness and orientation were assigned to the patch by dividing the original surface in different parts. Same color means same properties (see Fig. 7.10, symmetrical configurations). For the sake of simplicity, the material properties assigned to the patch were the same of the basic laminate, because no calibration data were available.
The mesh size of the patches was chosen finer than the one used for the basic laminates, because more importance was assigned to the good quality of the mesh (limited by the high number of parts) rather then the load level carried by the patch. In this way the correct distribution of the thickness can be represented. However, a finer mesh leads to a premature failure, which can be considered a conservative solution. The glass woven fabric was not included in the model, because of its negligible mechanical properties.
The nodes of the patches were connected to the nodes of the basic laminate with a node-to-surface TIED element. This represents the bonds created by the resin during the infusion. In the second approach (i.e. the model of the basic laminate with 3 surfaces each composed by 4 plies instead of a single surface including 12 plies), the same linking system was used.
The delamination interface is defined between two parallel layers of shell elements, one layer representing the slave nodes, and the other layer representing the master elements. In the undeformed state, each slave node is projected to the nearest master element surface creating a corresponding fictitious shadow node and a position penalty spring. The detailed approach can be found in [24]. This node-to-element approach is discontinuous, that is, the delamination elements, which can be considered as special spring elements, are not interconnected.

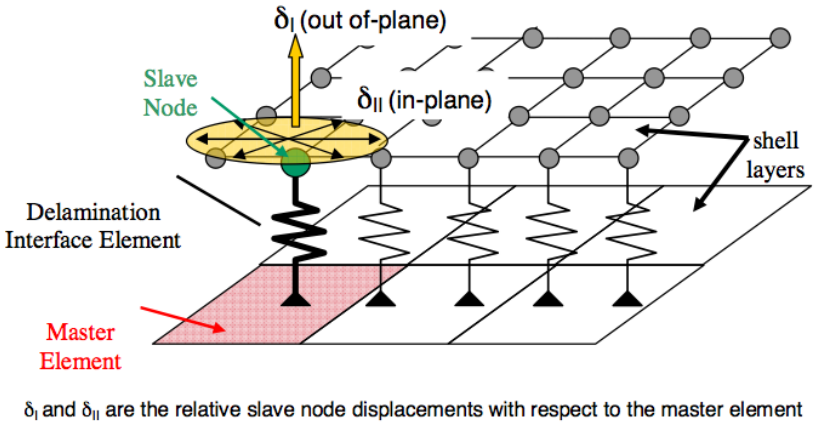

Figure 7.13: Tied elements method [24]

A continuous approach is expected to provide a better interpolation of the field quantities through the connected surface, however, the simplified discontinuous approach allows a more flexible application and automatic connection in complex structures and it was preferred because of the impossibility of assigning the same mesh to the basic laminate and to the patches.
The parameters representing the total strain energy release rates G_I and G_{II} were furnished by ESI Group, as no experimental tests were carried out so far for the characterization of inter-laminar properties of the investigated material. An example of the final model, in this case for 3 tied surfaces reinforced with 3 rovings per arm patch (configuration B), is shown in Fig. 7.14.

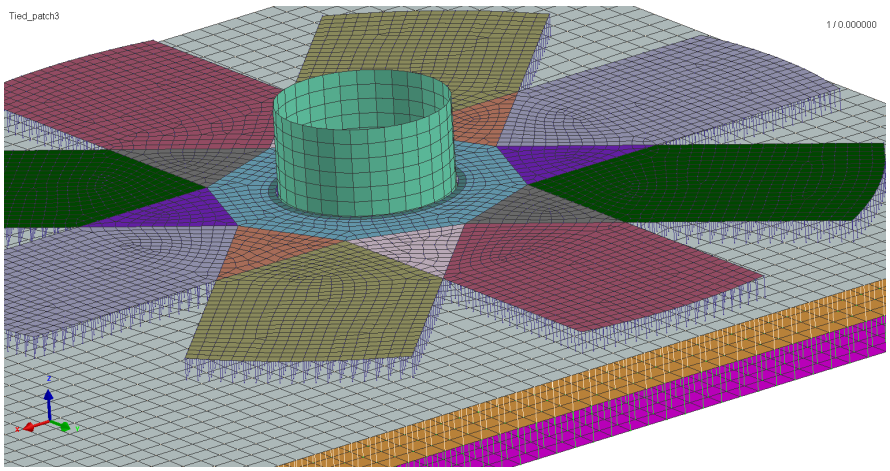

Figure 7.14: Tied elements

7.1.7 Crushing dataset

Up to now a standard modeling approach has been followed. According to the first simulations, obtained simply pulling the text fixture, Fig. 7.15, this model does not fit the problem. The elements in contact with the bolt become smaller and smaller until they reach their limit deformation value set in the ply card (which was defined by the compressive tests, as already explained in Chapter 4, Section 4.5). The contact force increases to this point, but then, as the solver eliminates the elements, it drops down, because the fastener suddenly finds no obstacle in its way. This happens for each following element, leading to the oscillating behavior of the contact force in Fig. 7.15, and preventing the coupon to reach the real load limit. This behavior is independent from the mesh size as well as from the failure criteria assigned to the material. Actually, it is possible to prevent the element from being eliminated, but in this approach the crushing force would simply keep

growing until high and unrealistic values. Therefore a different approach (crushing dataset) is needed.

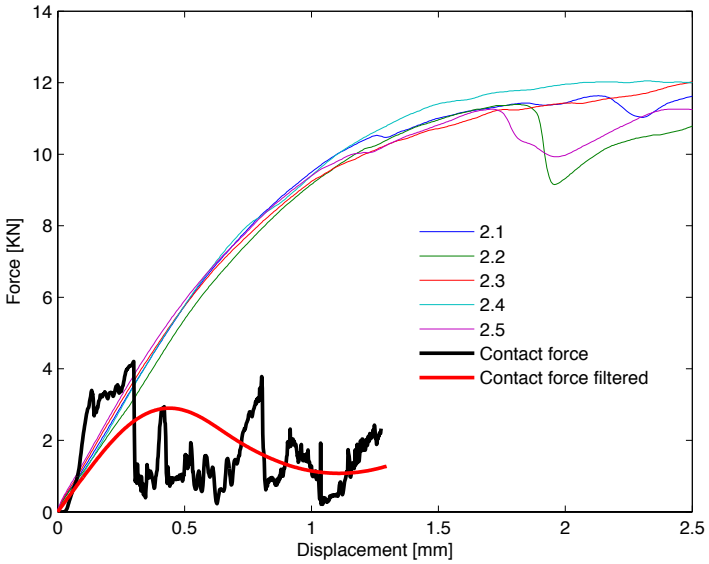

Figure 7.15: Simulation without crushing dataset

The principle of a crushing dataset is the following: elements located in direct contact with the "impacting" surface (type (A) in Fig. 7.16), start deforming when the contact event begins, while elements not in direct contact (type (B) in Fig. 7.16) absorb damage until the failure of the previous ones. Failure criteria and deformation limits do not have to be included in the ply card, since additional parameters are available in the crushing card itself to control the size of crushing elements (A) and enable the crush of subsequent element rows (B), Fig. 7.16.

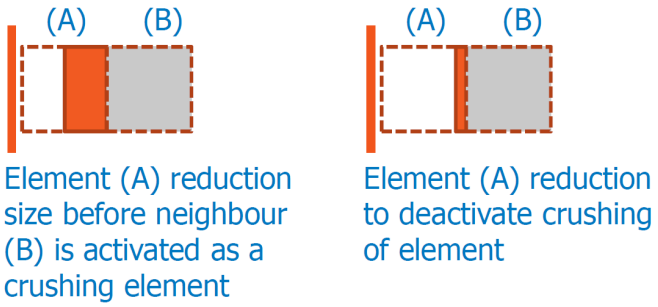

Figure 7.16: Crushing dataset: elements damaging size

The crushing stress is defined as the contact force divided by the contact area, so it does not correspond to the bearing stress. This value has to be set in the card to correlate the experimental curves. The original dataset used only two rows of elements due to the elasto-plastic behavior observed in a typical cylinder impact. However, because of the more complex shape of the bearing stress-strain curve, four rows of different crushing elements had to be chosen.

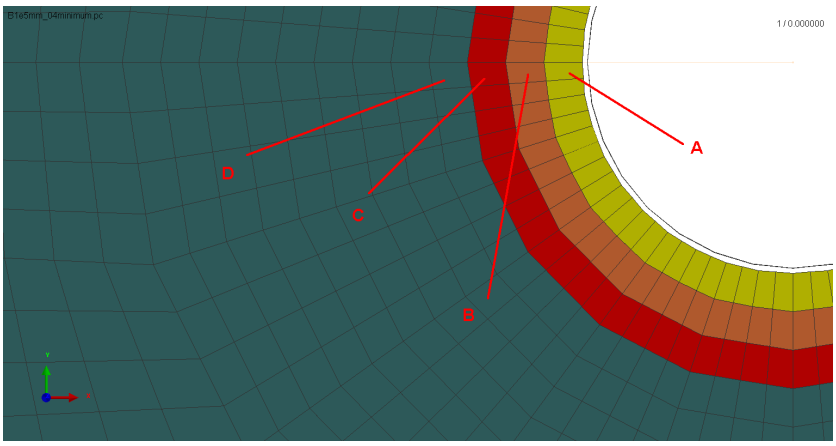

Figure 7.17: Elements crushing sequence around the hole

The original dataset suggests to use the load level of the flat plastic part of the experimental curve for the crushing stress, but in this study the choice of an unique value is not sufficient, because of the curve behavior after 2% deformation.

Table 7.1: Crushing elements data

Configuration											
1				2				3			
Element around the hole											
A	B	C	D	A	B	C	D	A	B	C	D
Crushing element type (2=A, 1=B in fig.7.17)											
2	2	1	1	2	2	1	1	2	2	1	1
Crushing stress [MPa]											
377	430	430	430	300	342	342	342	300	325	390	390
Ply numbering											
2	3	4	4	5	3	4	4	5	3	4	4

The strategy followed to assign the crushing stress consists in choosing the average ultimate load value of each configuration as first value, then applying increments from 15% to 30% to represent the hardening behavior. Due to the oscillations of the numerical curves, these values are actually asymptotic. When an element of type A, or 2 in Tab. 7.1, is used, all the elements in the following rows absorb damage, leading to a linear shape of the curve. On the other hand an element type B presents a typical perfectly plastic response. These behaviors were exploited in order to reproduce the shape of the experimental curves. A possible theoretical justification is proposed in the Section 7.2.1

7.1.8 Mesh dependency

According to what learnt from Chapter 5, the mesh size was chosen in order to correlate the load time history of the experimental tests with the numerical models. Only the right dimension of the elements around the hole allows to represent correctly the failure at the correct crushing stress. The correct mesh size of the elements closest to the hole resulted 0.5 mm. In Fig. 7.18 a finer and two coarser meshes in respect with the original one (here not reported) are presented, to highlight the dependency of the crushing phenomenon both in terms of ultimate stress and damaging slope.

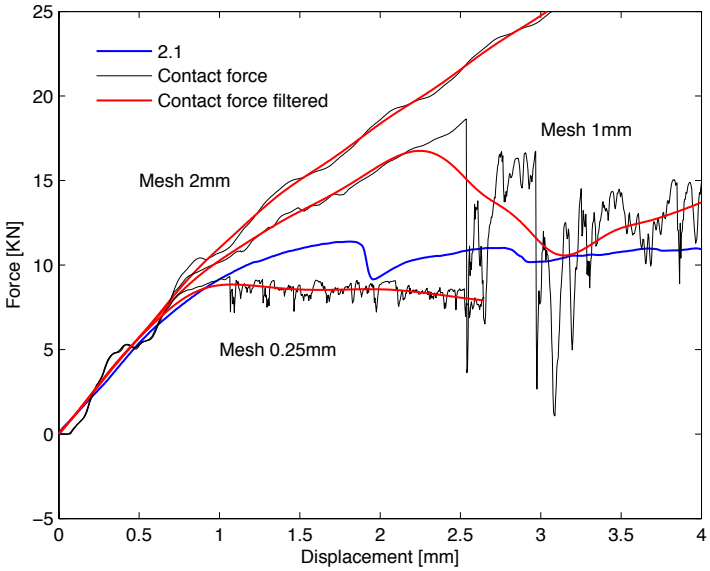

Figure 7.18: Mesh dependency of bearing models

7.2 Comparison with the experimental tests

The multilayered (Fig. 7.19, 7.21, 7.23) and tied surfaces (Fig. 7.20, 7.22, 7.24) final models of the basic and reinforced laminates are here presented.

Configuration 1

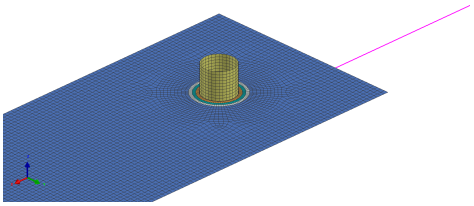

Figure 7.19: Multilayered numerical model configuration 1

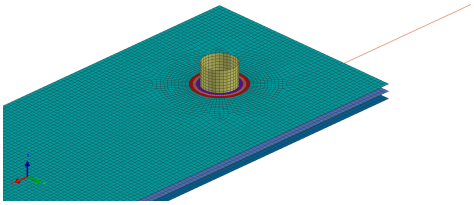

Figure 7.20: Tied numerical model configuration 1

Configuration 2

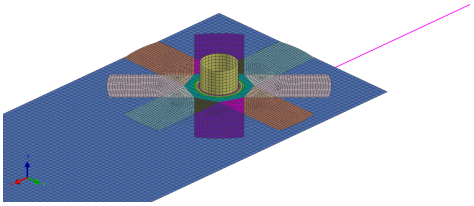

Figure 7.21: Multilayered numerical model configuration 2

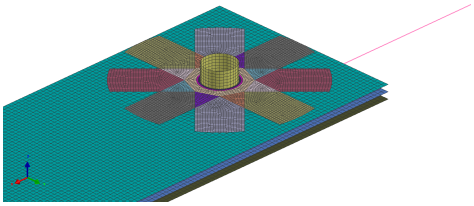

Figure 7.22: Tied numerical model configuration 2

Configuration 3

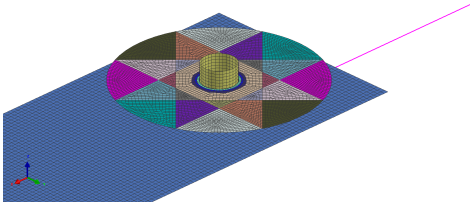

Figure 7.23: Multilayered numerical model configuration 3

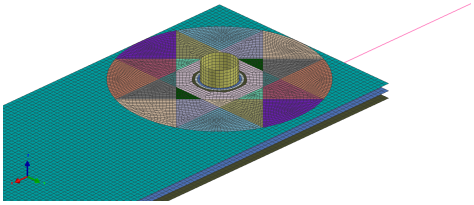

Figure 7.24: Tied numerical model configuration 3

All the configurations show good correlation with the experimental data until the first oscillation. Then delaminations of single rovings were observed in the experimental tests, but since in the ply card the composite material was modeled as homogeneous, this numerical model cannot represent the cracks originating between matrix and fibers. This implies that the oscillations of the experimental curves after the offset bearing strength are not visible in the numerical curves. That is, the correlation of the final part of the test is not reliable. The bi-phase model, implemented in PAM-CRASH, could probably fit the problem.
However, in a typical aeronautical design process, when the deformation exceed 2% a failure state has to be assumed. The correlation of the curve up to this value is the primary aim of the present model. Even if the same crushing stress was assigned to both configurations, the presence of tied elements generally reduces the oscillation in the contact force, whose filtered curve presents therefore a higher load value.

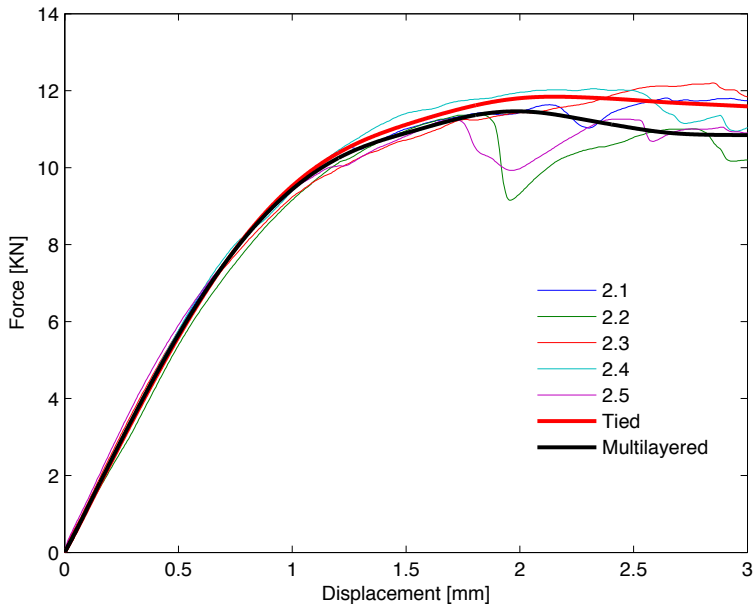

Figure 7.25: Configuration 1: Force-displacement curve

Coupons A.3, A.4, A.6, resulting from bad tests, were not considered for the calibration of configuration 2. This is the case of coupon B.1 too: in Fig. 7.27 it can be seen that its linear slope is quite different from the other ones of the same configuration.

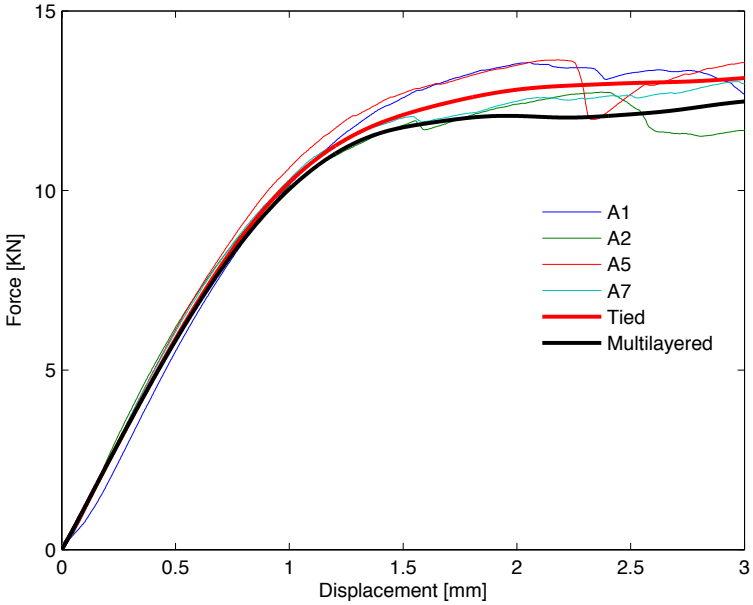

Figure 7.26: Configuration 2: Force-displacement curve

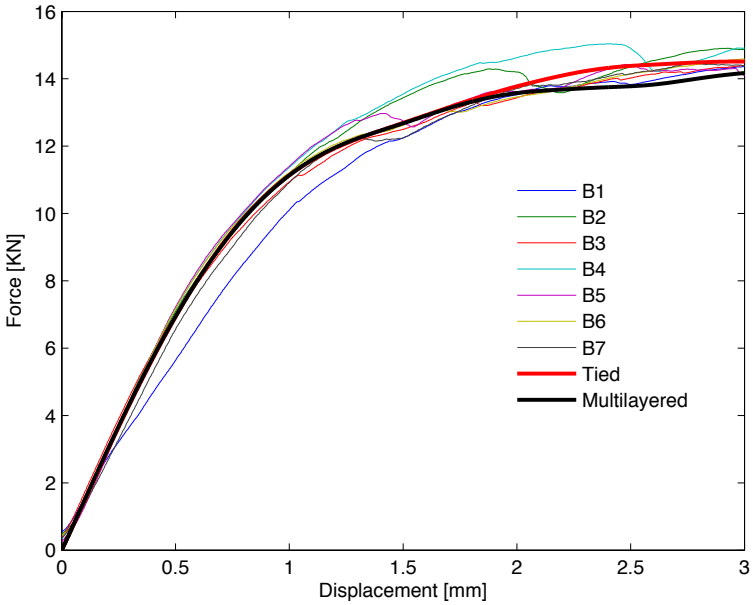

Figure 7.27: Configuration 3: Force-displacement curve

Finally a comparison between all the calibrated curves is presented. The coupons of configuration 3 exhibit a significant different slope in the first linear part of the curve, Fig. 7.28, which can depend on the influence of the test fixture as well as from the fact that the two configurations came from different infusions. The fiber volume content can show relevant oscillations depending on the low curing pressure and on the presence of pores. However, in this figure it is clear how the TFP patches reinforcements lead to a greater load-carrying capacity, in particular in configuration 3, with 5 rovings on each arm of the star.

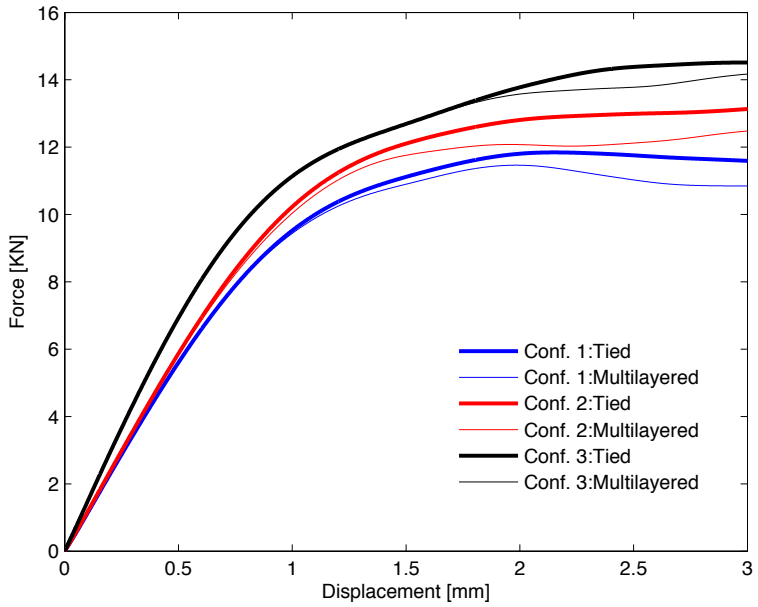

Figure 7.28: Comparison of all the correlated curves

7.2.1 Further considerations on the model

All the approximations considered in this simple approach prevent the model from the possibility of a post-failure study, but it is believed that it is able to lead to a fast and sufficiently accurate representation of the material behavior up to the offset bearing strength.
The purpose of the model is the correlation with the experimental data and not the prediction of the ultimate bearing stress. The correct failure damaging mode should look like in Fig. 7.29. The elements are not being eliminated and the damage is spread through the next elements.

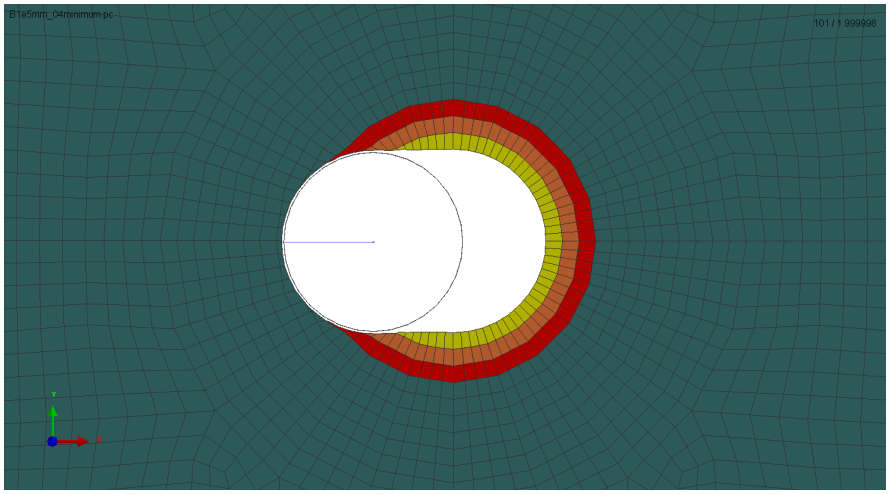

Figure 7.29: Bearing deformation in the numerical model

The identification of parameters such as damage growing functions or damage plasticity laws allowed the non linear behavior of the material to be effectively included in the model. In PAM CRASH, the total damage of the elements represents the changing in slope of the elastic modulus. Fig. 7.30 and 7.31 show clearly how the damage propagates from the elements in contact with the fastener through the other elements. The elastic modulus reaches a reduction of almost 20% from the initial value before the element start transferring the damage.

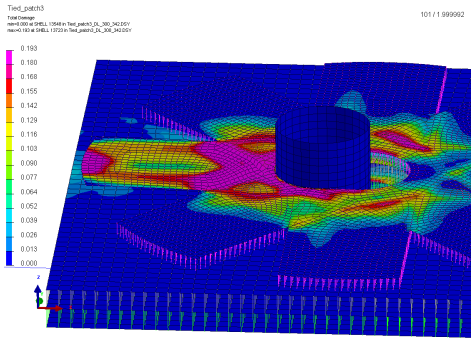

Figure 7.30: Total damage in configuration 2, tied surfaces

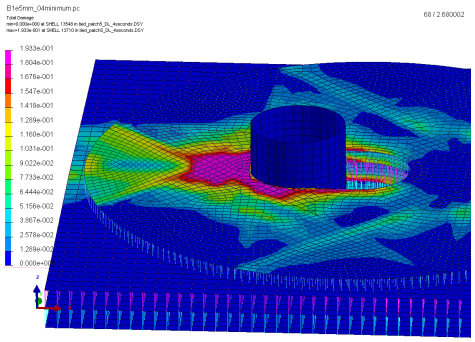

Figure 7.31: Total damage in configuration 3, tied surfaces

The use of different crushing stresses, as well as the hardening behavior of the coupons, can be explained with the Fig. 7.32. At the beginning the fastener is surrounded by cut fibers, but moving forward through the ±45° intact reinforcements it comes across more resistance.

Detachment of the edge in 0° and ±45° rovings from the specimen can be seen at the end of the simulation, in Fig. 7.33. Delaminations are represented by the elimination of the tied elements. Since the material was modeled as homogeneous, no rupture between fibers and matrix is visible.

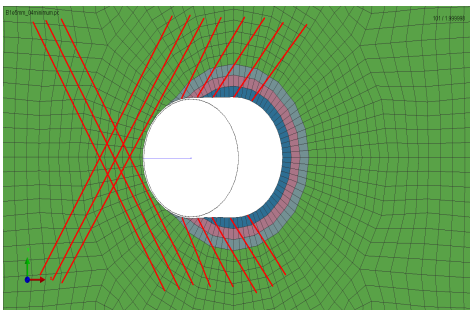

Figure 7.32: Integer and cut ±45° fibers disposition

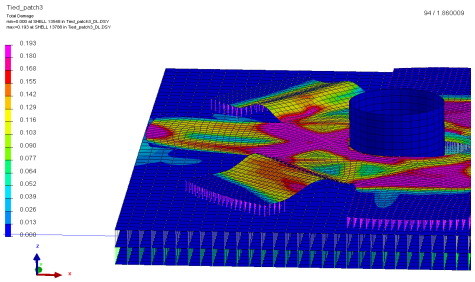

Figure 7.33: Delaminations of the rovings

The model has a quite fast simulation time: in the worst case, with 3 tied surfaces and a patch with 5 rovings per arm, less than an hour.
The correlation was successful thanks to the correct mesh size chosen. In the perspective of a possible implementation of the model in more complex components, it seems more reasonable to assign the correct mesh size than change the material crushing stress, because, as already shown, both the ultimate load and the slope of the plasticity part are considerably influenced by the dimensions of the elements around the hole.

Chapter 8

Conclusions and future works

Experimental bearing tests were carried out on TFP-reinforced coupons manufactured with VARI process, in order to understand the bearing damage and failure phenomenology, and to investigate the advantages in applying TFP-star-patches on holed flat composite panels.
The reinforcements have led to a significant improvement of the load carrying capacity of the coupons tested, showing better results than other patch configurations used before. In particular, the configuration with 5 rovings/arm resulted more effective than the one with 3 rovings/arm.
The VARI process did not seem convincing, because it causes an increased local thickness of the reinforced coupons, which resulted in a lower bearing strength than the one in the unreinforced laminate. Other manufacturing procedures, like Resin Transfer Moulding, or hot isostatic pressure, should be tried in the next investigations in order to achieve an efficient and competitive solution for practical industrial applications.
Data collected from calibration tests on carbon/epoxy material were implemented in a numerical model for the correlation with the bearing tests.
The finite element model derives from an experimental and numerical study on notched coupons, which highlighted a mesh size dependency of the problem. The average stress criterion developed by Whitney and Nuismer was proven reliable for the study of a cross-ply stacking sequence, but not for an angle-ply configuration.
Coupons were modeled in two different configurations: as a single flat specimen and as a stacking of multilayered surfaces. The tied elements representing delaminations used data collected from literature. A specific delamination test program, such as MMB, ENF, and DCB tests, should follow in order to characterize the correct values of the inter-laminar properties, both in unreinforced and patch-reinforced coupons.
A trial research code implemented in the software PAM-CRASH for the study

of crushing phenomena, was applied with some modifications and adapted in order to represent the complex bearing behavior seen in the tests.
The numerical model has been proven effective in the representation of the bearing damaging behavior in both the unreinforced and reinforced configurations. According to CERFAC project guidelines the model could be modified in the perspective of an optimization process. An optimization analysis could investigate the best orientation of the rovings able to improve the bearing strength. However, since the crushing stress is currently set from the experimental data, more tests with more different patches configuration should be carried out, in order to identify a possible relationship between crushing stress and roving orientation.
For an investigation of the post-failure behavior, improvements should be also introduced in the crushing dataset, in the model of the test fixture, as well as for the boundary conditions and the contact cards. The present work has shown the importance and the advantages of combining a numerical and an experimental method in the study of structural engineering problems. Arguably, the method here developed could be adopted to simulate any general bearing test conducted on holed flat composite surfaces, with different hole size, stacking sequence, and TFP reinforcing patches.
Experimental tests on other patch configurations should be carried out, in order to discover a relationship between the crushing stress and the orientation of the rovings in the perspective of a numerical optimization analysis.
According to the building block approach, this model represents a minor joining system element (D level) available for larger aeronautical panels (C level), where TFP patches reinforcements could also be applied.

Appendix A

Reinforcements optimization

A.1 Delamination problems in TFP patch reinforcements

One of the main weaknesses of patch reinforcements consists in the detachment of the patch from the basic laminate, as it can be experienced in many tests. Delamination occurs when the inter-laminar shear stresses, caused by dissimilar elastic properties in patches and specimens, reach a limit value. An optimization analysis based on the classical lamination theory has been performed, in order to prevent this failure mode. Fig .4.2 of Chapter 4 shows how different elastic moduli can increase the possibility of failure.
The patches considered in this study are made of several rovings aligned in different directions (0°, ±45° and 90°), in respect with the laminate frame of reference (x,y,z) represented in Fig. A.1.

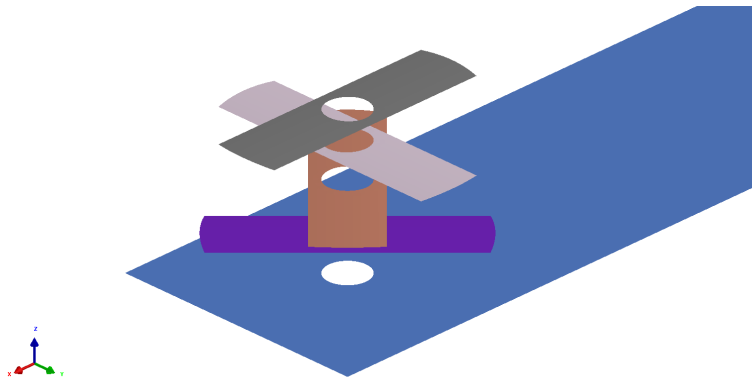

Figure A.1: Patch composed by differently oriented rovings

The purpose of this analysis is to determine the optimized number of rovings that should be placed in each direction to match the elastic modulus of the specimen in the load direction E_{xx}^{0t}, in order to obtain a more homogenous behavior of the inter-laminar shear stresses.
This is done by comparison of the elastic moduli of two idealized laminates, one representing the basic specimen and the other one representing the reinforcement patch. This is obtained superimposing different plies, whose properties depend on the number of rovings aligned in each direction.
The mechanical properties of the reinforcements are evaluated from the original material datasheets, while the ply data for the specimen come from the calibration described in Chapter 4. Once the characteristics of the plies are obtained, the laminates stiffnesses are calculated by means of the Classical Lamination Theory.

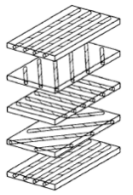

Figure A.2: Laminate modeling level [32]

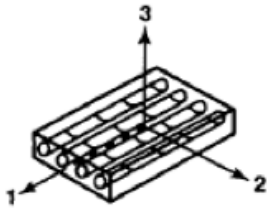

Figure A.3: macroscopic modeling level [32]

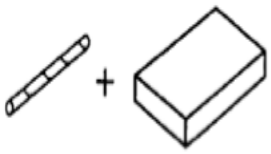

Figure A.4: microscopic modeling level [32]

Depending on the purpose of the analysis, three basic modeling techniques for composites can be distinguished [37]: using a laminate approach, as shown in Fig. A.2, the composite material is often modeled as homogeneous orthotropic material or homogeneous fully anisotropic material (laminate level); in a macroscopic approach, as shown in Fig. A.3, the material is typically considered as a transverse isotropic or orthotropic material (lamina or ply level); finally in a microscopic approach, as shown in Fig. A.4, matrix and reinforcement in the material are modeled separately as deformable continua (fiber/matrix, sub-lamina level).
In order to analyze the effect of different materials and phase properties on the mechanical behavior of the patch, all these three modeling steps are here used. The application of a theoretical model for the prediction of the mechanical behavior can replace partially the experimental tests and may significantly reduce the design cost, even if it remains only a preliminary study [37].

A.1.1 Microscopic approach - Patch ply

Three different types if fiber (rovings) from TOHO TENAX^{TM}[38], were used in the study of the patches, in order to examine different possibilities and to check the model efficiency. In Tab. A.1 only the relevant data for fibers and matrix are documented.

Table A.1: Fibers and Resin data (*in italic data collected from [16]*)

Materials	**E [GPa]**	ν **[-]**	**tex [g/km]**	ρ **[g/cm^3]**
TOHO TENAX HTS 40	240	*0.25*	800	1.76
TOHO TENAX IM 60	290	*0.25*	830	1.80
TOHO TENAX HMA 35	360	*0.25*	770	1.78
EPIKOTE RIM 235	3.1	*0.4*		1.15

The purpose of the microscopic approach is to combine the two different phases (matrix and fibers) of the starting composite material, in order to obtain the elastic coefficients of an equivalent anisotropic homogeneous material. In particular, the results achieved depend strongly on the analytical model used. The 'Rule of Mixtures' is the most common method and consider the constitutive phases of a single representative volume (REV) in parallel or in series. From now on, any elastic property referred to the ply will be denoted with the subscript $_{1,2,3}$, while the ones referred to the laminate will be labelled with $_{x,y,z}$. Furthermore $_f$ and $_m$ are referred to the fiber and to the matrix respectively. Assuming a constant strain in the ply and recalling the fibre volume content ϕ, the E modulus in the fibre direction and the Poisson's coefficient can be evaluated respectively as:

$$E_1 = \phi \cdot E_f + (1 - \phi) \cdot E_m \tag{A.1}$$

$$\nu = \phi \cdot \nu_f + (1 - \phi) \cdot \nu_m \tag{A.2}$$

The Rule of Mixture provides also the elastic modulus in the transverse direction, E_2, and the shear modulus, G_{12}, as:

$$\frac{1}{E_2} = \frac{\phi}{E_f} + \frac{1 - \phi}{E_m} \tag{A.3}$$

$$\frac{1}{G_{12}} = \frac{\phi}{G_f} + \frac{1 - \phi}{G_m} \tag{A.4}$$

There are other approaches, which are similar to the Rule of Mixtures, but lead to substantial improvements. One of these is the by Puck's model [39]. It uses different cells (REV) to provide better estimating of the elastic moduli. A study among several composite systems gives the following equations,

$$E_m^0 = \frac{E_m}{1-\nu^2} \tag{A.5}$$

$$E_2 = E_m^0 \frac{1 + 0.85 \cdot \phi^2}{(1-\phi_f)^{1.25} + \phi \cdot (\frac{E_m^0}{E_f})} \tag{A.6}$$

$$G_{12} = G^m \frac{1 + 0.6\sqrt{\phi}}{(1-\phi_f)^{1.25} + \phi \cdot (\frac{G_m}{G_f})} \tag{A.7}$$

By considering the effect of lateral constraints imposed by strain compatibility, this approach leads to a higher transverse modulus, as it can be seen in Tab. A.2. In the next sections the Puck's model will be used for the evaluation of the mechanical parameters.

Table A.2: Comparison between Rule of Mixtures and Puck's Model, single ply of HTS 40

Ply Properties	**Rule of Mixture**	**Puck's Model**	**Difference**
$\mathbf{E}_2$	6.78 GPa	12.30 GPa	+81.4%
$\mathbf{G}_{12}$	6.62 GPa	4.26 GPa	-35.6%

A.1.2 Macroscopic modelling - Patch ply

Each roving can be represented by a single ply with the properties just calculated. Besides these data, the thickness of every layer has to be defined too for the CLT study. For a single roving a standard width of 3 mm was chosen, which is the usual width provided by the stitching machine. The thickness of the ply representing the patch is evaluated according to the following simplifications. According to the patch configuration used in this project, the length of a roving is fixed at 34 mm, and its mass can be calculated starting from the *tex* data:

$$m_f = tex \cdot L \tag{A.8}$$

The total mass can be obtained through simple passages, once the fibre volume content (ϕ) is set:

$$V_f = \frac{m_f}{\rho_f} \tag{A.9}$$

$$V_{tot} = V_f \cdot \phi \tag{A.10}$$

$$V_m = V_{tot} - V_f \tag{A.11}$$

$$m_m = \rho_m \cdot V_m \tag{A.12}$$

$$m_{tot} = m_m + m_f \tag{A.13}$$

$$A = L \cdot w \tag{A.14}$$

Finally the thickness is calculated from the simple equation:

$$t = \frac{m_{tot}}{\rho \cdot A} \tag{A.15}$$

All the passages were followed for FVC (Fiber Volume Content) of 55% and 60%. The data below were obtained and given as input for the CLT:

Table A.3: 55% and 60% FVC (Fiber Volume Content)

55% FVC					
	$\mathbf{E_1^{0t}}$ **[GPa]**	$\mathbf{E_2^{0t}}$ **[GPa]**	$\boldsymbol{\nu_{12}^0}$ **[-]**	$\mathbf{G_{12}^0}$ **[GPa]**	**t [mm]**
HTS 40	133.39	12.30	0.3175	4.26	0.274
IM 60	160.89	12.35	0.3175	4.28	0.284
HMA 35	199.40	12.39	0.3175	4.29	0.263
60% FVC					
	$\mathbf{E_1^{0t}}$ **[GPa]**	$\mathbf{E_2^{0t}}$ **[GPa]**	$\boldsymbol{\nu_{12}^0}$ **[-]**	$\mathbf{G_{12}^0}$ **[GPa]**	**t [mm]**
HTS 40	145.24	14.72	0.31	4.99	0.251
IM 60	175.24	14.79	0.31	5.00	0.261
HMA 35	217.24	14.86	0.31	5.03	0.241

A.1.3 Macroscopic modeling - specimen ply

A ply with the elastic properties summarized in Tab. A.4 (which come from the material calibration of chapter 4) is taken as a reference for the basic specimen:

Table A.4: Test specimen mechanical properties

	$\mathbf{E_1^{0t}}$ **[GPa]**	$\mathbf{E_2^{0t}}$ **[GPa]**	$\boldsymbol{\nu_{12}^0}$ **[-]**	$\mathbf{G_{12}^0}$ **[GPa]**	**thickness [mm]**
specimen	127.3	9.9	0.3	5.0	3.7

A.1.4 Laminate and Patch modeling - CLT

The Classical Lamination Theory allow to predict the elastic modulus in the laminate direction E_{xx}^{0t}. A 0° dominated and a QI configuration were studied for the specimen.

Configuration	**Lay-up**	$\mathbf{E_{xx}^{0t}}$ [GPa]
1	0° [90/45/0/0/45/0/0/45/0/0/45/90]	286.876
2	QI [45/0/-45/90/45/0/90/-45/90/-45/0/45]	194.375

Table A.5: Specimen Configurations

As to the patch, the modulus E_{xx}^{0t} was obtained for each ply representing a roving through the CLT. A single layer in the 0° direction and two layers in the ±45° direction were considered. Rovings in the 90° direction were not considered in this study, due to their low contribute to the E_{xx}^{0t} modulus.

Table A.6: Patch ply E_{xx}^{0t}: 55 % FVC

55% FVC	$\mathbf{E_{xx}^{0t}}$ 0° **[GPa]**	$\mathbf{E_{xx}^{0t}}$ 45° **[GPa]**
HTS 40	36.883	23.561
IM 60	46.083	28.366
HMA 35	52.903	31.403

Table A.7: Patch ply E_{xx}^{0t}: 60 % FVC

60% FVC	$\mathbf{E_{xx}^{0t}}$ 0° **[GPa]**	$\mathbf{E_{xx}^{0t}}$ 45° **[GPa]**
HTS 40	36.828	23.944
IM 60	46.026	28.770
HMA 35	52.851	31.783

The hypotheses assumed up to now consider each series of roving (one arm in the star configuration) as a ply with a larger surface than the real one.

Hence, every E_{xx}^{0t} was weighed with respect to the ratio of the area occupied by the actual roving surface A_i^j to the specimen surface A_{tot}, considered as a circular surface with diameter equal to the length of a single roving.

$$w_i^j = \frac{A_i^j}{A_{tot}} \tag{A.16}$$

Varying the number of rovings in each direction, and stacking differently oriented plies, an equivalent E_{xx}^{0t} can be obtained and compared to the one of the specimens.

$$E_{patch} = E^{0^\circ} w_i^{0^\circ} + 2E^{45^\circ} w_i^{45^\circ} \tag{A.17}$$

A.2 Results

Different number of rovings in each direction produces different trends of E_{xx}^{0t} modulus. Starting with 2 rovings/arm and increasing gradually the number of reinforcements in each direction up to 8 rovings/arm, the results of Fig. A.5 are obtained.
In the case of a IM 60 material a configuration with 4 and 4 rovings/arm, respectively in the (0°) and (±45°) directions, could be suggested to reinforce a QI specimen, while a 6 and 4 roving/arm configuration looks more suitable for a 0° dominated basic laminate.

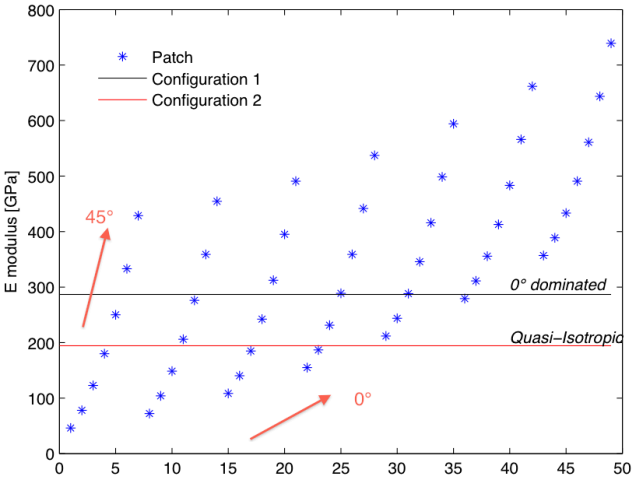

Figure A.5: IM 60 optimization results: 2 to 8 rovings per arm

Other configurations are here compared. A variation of FVC does not show significant changes, because even if increasing the FVC results in a higher contribute from each ply to the total E_{xx}^{0t}, it leads to a reduction of the thickness of the ply, consequence of the investigation method followed.

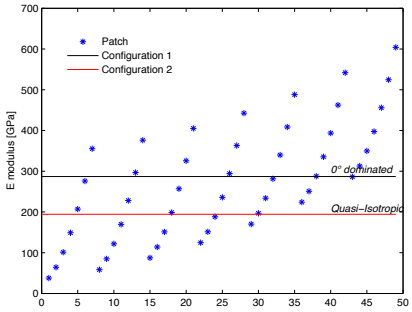

Figure A.6: HTS 40 55% FVC

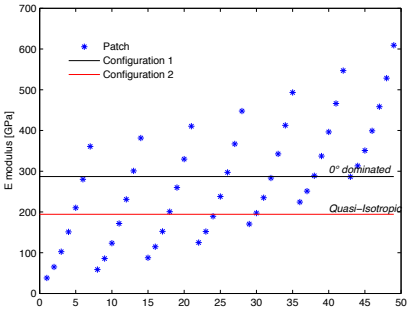

Figure A.7: HTS 40 60% FVC

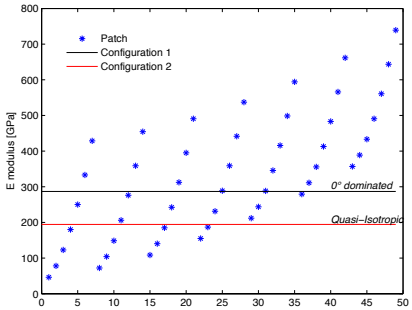

Figure A.8: IM 60 55% FVC

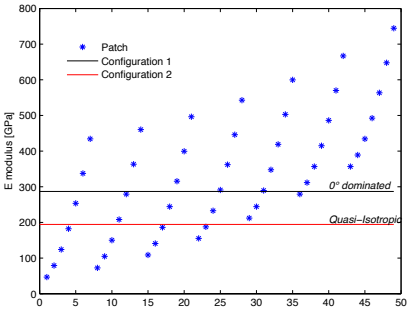

Figure A.9: IM 60 60% FVC

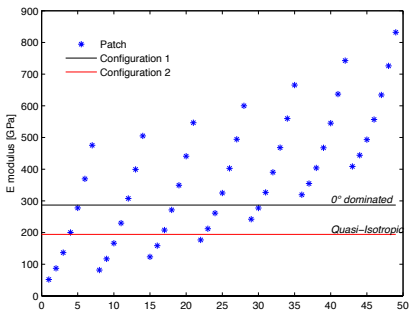

Figure A.10: HMA 35 55% FVC

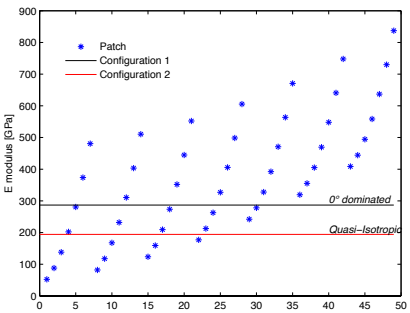

Figure A.11: HMA 35 60% FVC

Appendix B

Experimental test results

In this section the load time history and the results obtained for every configuration are listed.
Fig. B.1 proposes again how the experimental data were processed according to the standards (see Chapter 6), while Tab. B.1 presents the bearing test data acquired for each configuration. Finally for every configuration the recorded forces versus the displacements of the upper load cell and the bearing stress-strains curves are outlined.

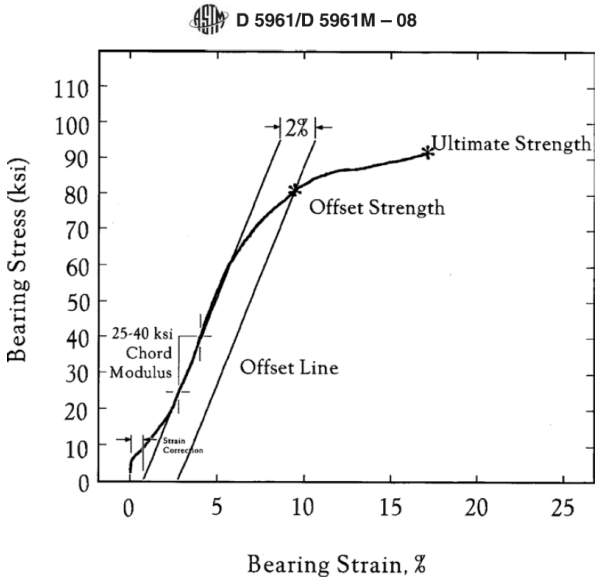

Figure B.1: Bearing stress-strain curve according to the standards

Table B.1: Comparison of experimental data

Configuration 1				
Specimen	E^{br} [GPa]	F_x^{bro} [MPa]	F_x^{bru} [MPa]	thickness [mm]
2.1	34.773	446.253	597.633	3.38
2.2	31.549	457.594	561.637	3.38
2.3	34.119	398.148	594.542	3.42
2.4	37.491	418.699	612.297	3.28
2.5	35.177	398.551	581.643	3.45

Configuration 2				
Specimen	E^{br} [GPa]	F_x^{bro} [MPa]	F_x^{bru} [MPa]	thickness [mm]
A.1	26.045	325.902	480.184	4.71
A.2	25.606	334.725	443.285	4.79
A.3	*20.216*	*270.705*	*352.156*	*4.87*
A.4	*23.356*	*285.004*	*388.415*	*4.69*
A.5	26.000	348.141	469.697	4.84
A.6	*22.187*	*305.903*	*449.306*	*4.80*
A.7	26.314	346.209	466.023	4.66

Configuration 3				
Specimen	E^{br} [GPa]	F_x^{bro} [MPa]	F_x^{bru} [MPa]	thickness [mm]
B.1	*19.320*	*393.546*	*478.377*	*5.01*
B.2	29.666	335.374	515.646	4.90
B.3	27.762	344.921	495.569	4.89
B.4	29.505	330.667	501.333	5.00
B.5	30.761	325.926	485.859	4.95
B.6	28.754	322.287	474.659	5.13
B.7	27.083	342.195	493.865	4.89

B.1 Configuration 1

These data come from the tests carried out by Urbanek at IFB [5], and are hereby depicted only for a useful comparison with the other results.

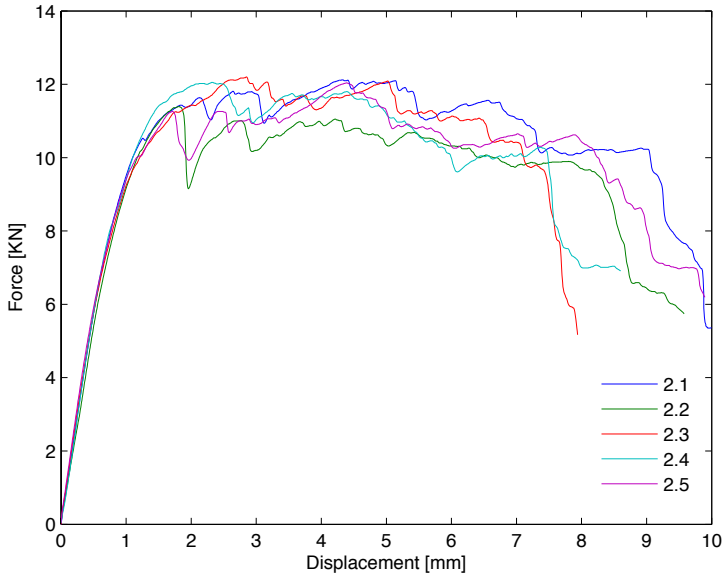

Figure B.2: Configuration 1: Force-displacement curve

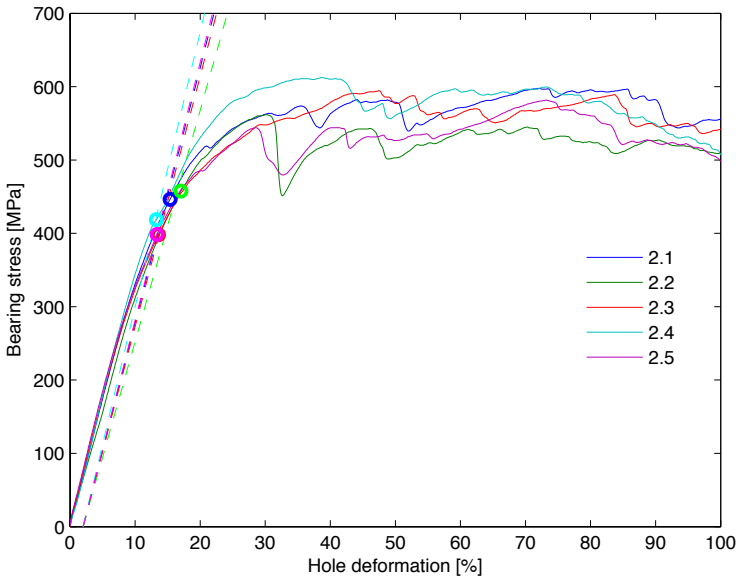

Figure B.3: Configuration 1: Bearing stress-strain curve

B.2 Configuration 2

In this configuration TFP star patches with 3 rovings per arm were applied on the laminate.

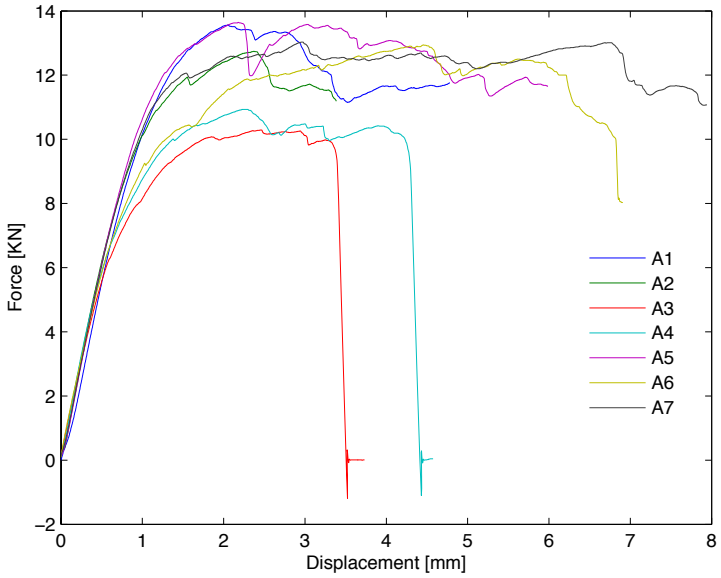

Figure B.4: Configuration 2: Force-displacement curve

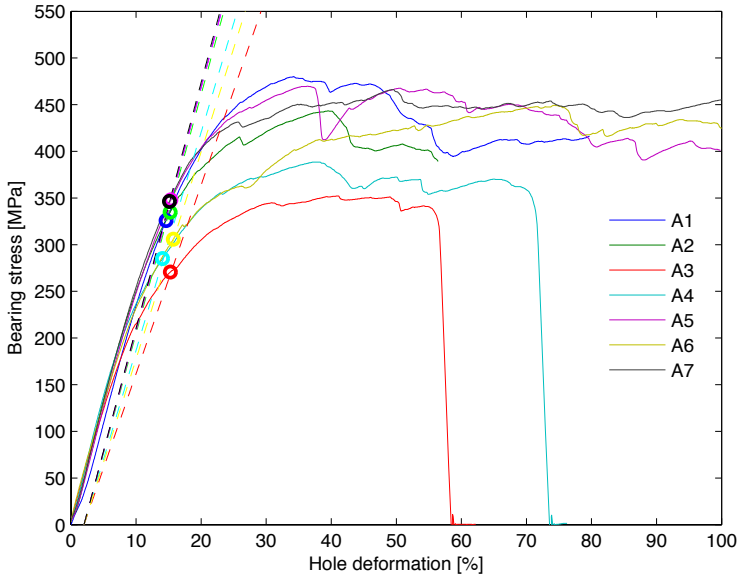

Figure B.5: Configuration 2: Bearing stress-strain curve

B.3 Configuration 3

In this configuration TFP star patches with 5 rovings per arm were applied on the laminate.

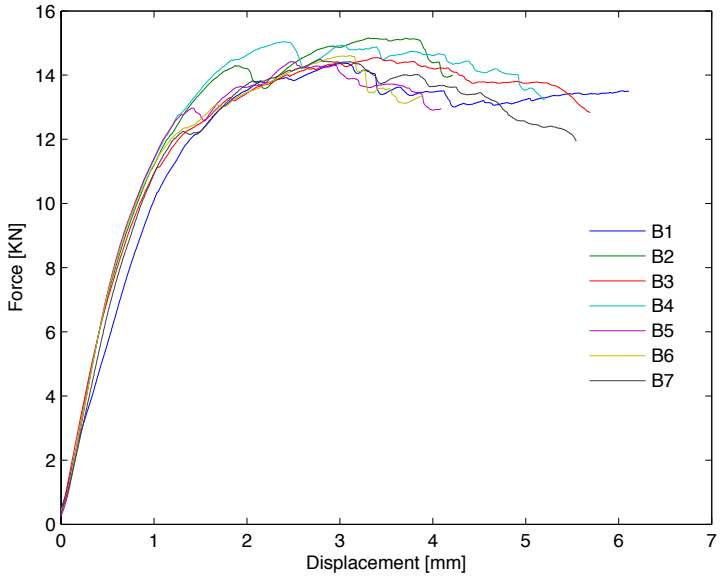

Figure B.6: Configuration 3: Force-displacement curve

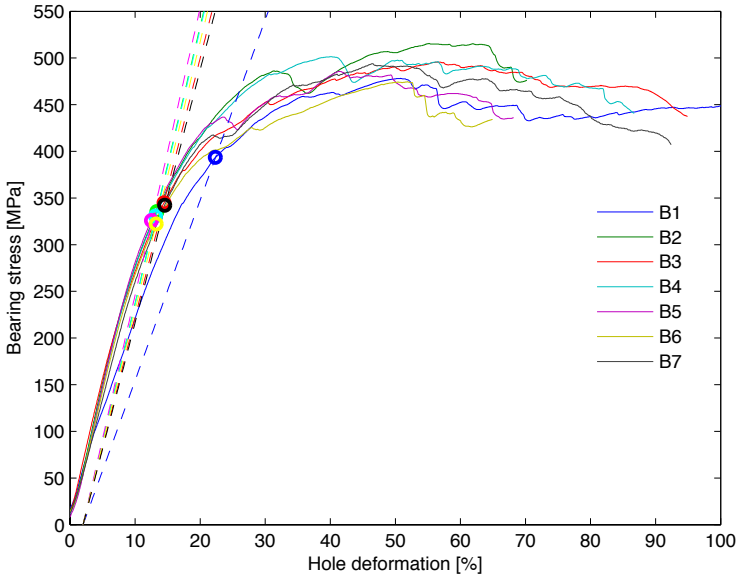

Figure B.7: Configuration 3: Bearing stress-strain curve

Bibliography

[1] http://bintang.site11.com/Boeing_787/B787.htm

[2] K.N. Kendall, C.D. Rudd, M.J. Owen, V. Middleton, *Characterization of the resin transfer moulding process, Composites Manufacturing*, Volume 3, Issue 4, 1992, Pages 235-249.

[3] L.J. Hart-Smith, *Joints, Engineered materials handbook: Composites*, vol. 1. Metal Park, OH: ASM International; 1987. p. 479–95.

[4] Y. Xiao, T. Ishikawa, *Bearing strength and failure behavior, of bolted composite joints (part II: modeling and simulauiont)*, Composites Science and Technology, 65 (7-8) , 2005, pp. 1022-1031.

[5] Y. Urbanek, *Experimentelle Untersuchung und Optimierung der Lochleibungseigenschaften von TFP-verstärken einschnittigen Laschenverbindungen*, Diplomarbeit, Stuttgart, 2012.

[6] http://www.ipfdd.de/Tailored-Fibre-Placement-TFP.424.0.html?L=0

[7] http://altairenlighten.com/2012/09/premium-aerotec-boeing-demonstrate-lightweight-composite-wing-spar.

[8] http://2013success4me.info/about/design-construction.

[9] B. Yenilmez, M. Senan, E. Murat Sozer, *Variation of part thickness and compaction pressure in vacuum infusion process*, Composites Science and Technology, 69 (11-12) , 2009, pp. 1710-1719.

[10] D. Bender, J. Schuster , D. Heider, *Flow rate control during vacuum-assisted resin transfer molding (VARTM) processing*, Composites Science and Technology 66, 2006, pp. 2265-2271.

[11] Engineering Systems International, *PAM RTM 2010 UserGuide-Tutorials*, www.esi-group.com

[12] E. Sevkat, M. Brahimi, *The bearing strength of pin loaded woven composites manufactored by vacuum assisted resin transfer moulding and hand lay-up techniques*, Procedia Engineering, Volume 10, 2011, Pages 153–158.

[13] Saertek® V104326-00300-01270 Unidirectional layer, *Datenblatt Entwurf*, 2011.

[14] Momentive™EPIKOTE™Resin MGS® RIM 234, EPIKURE™Curing Agent RIM H 235, *Technical Data Sheet*, 2006.

[15] Torayca® T700S, *Technical Data Sheet*, 2006.

[16] A. Kunart, *Application of the Tailored Fibre Placement Method with Optimization Software for the Reduction of Stress Concentrations in Composite Parts*, Universität Stuttgart, Research project, 2012.

[17] P. Carman, P. Tigwell, *CATIA reference guide.*

[18] Henkel®, *770 NC Frekote datasheet.*

[19] Lange & Ritter, *Klebeharzsystem A10/B10. Technische Daten*, 2011.

[20] G. Sala, L. Di Landro, A. Airoldi, P. Bettini, *Tecnologie sottrattive dei materiali compositi*, Dipartimento di ingegneria aerospaziale, Politecnico di Milano.

[21] GOM mbH, *ARAMIS User Maual - Software*, 2007.

[22] P. Ladevèze, E. Le Dantec, *Damage Modeling of the elementary ply for laminated composites*, Composites Science and Technology, Vol. 43, Issue 3, 1992, pp. 257-267.

[23] Engineering Systems International, *PAM-CRASH Users manuals*, www.esi-group.com

[24] L. Greve, A.K. Pickett, *Delamination testing and modelling for composite crash simulation*, Composites Science and Technology, Volume 66, Issue 6, May 2006, Pages 816–826.

[25] E. Reissner, *On Bending of Elastic Plates*, Quarterly of Applied Mathematics, Vol. 5, No. 1, 1947, pp. 55-68.

[26] R.D. Mindlin *Influence of Rotary Inertia and Shear On Flexural Motions of Isotropic Elastic Plates*, ASME Journal of Applied Mechanics, Vol. 18, No. 1, 1951, pp. 31-38.

[27] *LS-Dyna User's Manual*, Livermore Software Technology Corporation. http://www.lstc.com

[28] R.A. Brockman, *Dynamics of the Bilinear Mindlin Plate Element*, International Journal for Numerical Methods in Engineering, Vol. 24, 1987, pp. 2343-2356.

[29] S.P. Timoskenko, J.N. Goodier, *Theory of Elasticity*, Second Edition, McGraw-Hill, New York, 1951, pp. 78.

[30] ASTM D 3039/D 3039M 08, *Standard Test Method for Tensile Properties of Polymer Matrix Composite Materials.*

[31] F.L. Matthews, *Bolted Joints*, Composites Design, 1986.

[32] G. Sala, L. Di Landro, A. Airoldi, P. Bettini, *Effetto della fatica e dell'ambiente sui compositi*, Dipartimento di ingegneria aerospaziali, Politecnico di Milano.

[33] Whitney JM, Nuismer RJ, *Stress Fracture Criteria for Laminated Composites Containing Stress Concentrations*, Journal of Composite Materials, Vol. 8, 1974, pp. 253-265.

[34] ASTM D5961/D5961M -08, *Standard Test Method for Bearing Response of Polymer Matrix Composite Laminates.* ASTM International, West Conshohocken, 2008.

[35] H.J. Park, *Effects of stacking sequence and clamping force on the bearing strengths of mechanically fastened joints in composite laminates*, Composite Structures 53, 2001, pp. 213-221.

[36] A.F. Johnson, A. Pickett, P. Rozycki, *Computational methods for predicting impact damage in composite structures*, Composite Science and Technology, Vol. 61, Issue 15, 2001, pp. 2183-2192.

[37] L. Mishnaevsky Jr., *Computational Mesomechanics of Composites*, John Wiley & Sons, 2007.

[38] http://www.tohotenax.com/tenax/en/products/st_property.php

[39] A.R. Bunsell, J. Renard, *Fundamentals of Fibre Reinforced Composite Material*, 2010, pp. 203-204.